

POLITECNICO DI MILANO

School of Industrial and Information Engineering  
Master of Science degree in Mathematical Engineering



STATISTICAL ANALYSIS OF fNIRS DATA  
APPLIED TO CEREBRAL HEMODYNAMICS

Master Thesis

Viola BONOMINI, 786863

Supervisor: Prof. Anna Maria PAGANONI

Co-supervisor: Dott. Francesca IEVA

Academic year 2013-2014



*In un certo senso, non si scopre che quello che si vuole trovare. Per lo meno è sempre vero che non si scopre senza una volontà di trovare e senza qualche ipotesi di ricerca. Non si ricerca con la testa vuota, ma con la testa piena: di cultura, di idee, di domande, di curiosità, di desideri, di aspettative, di previsioni, di profezie, e talora, di errori, come Colombo.*

G. PREZZOLINI

*A mamma e papà.*



# Contents

Sommario . . . . .	xi
Abstract . . . . .	xiii
<b>Introduzione</b>	<b>1</b>
<b>Introduction</b>	<b>3</b>
<b>1 Introduction to NIRS</b>	<b>5</b>
1.1 An optical method with several applications . . . . .	5
1.2 The State of the Art . . . . .	9
1.3 The software NIRS-SPM . . . . .	17
<b>2 The datasets</b>	<b>25</b>
2.1 Pre-processing . . . . .	26
2.2 In vivo data . . . . .	26
2.3 Synthetic data . . . . .	29
<b>3 AUC Analysis</b>	<b>37</b>
3.1 AUC analysis for activation detection . . . . .	38
3.2 AUC analysis for anomalous channels detection . . . . .	39
<b>4 Activation detection trough linear regression models</b>	<b>47</b>
4.1 The linear regression model . . . . .	47
4.2 Analysis of the coefficients of the models . . . . .	50
4.3 Activation maps . . . . .	55
4.4 K-means clustering algorithm . . . . .	62
4.5 Group Analysis . . . . .	68

<b>5</b>	<b>Bayesian analysis</b>	<b>73</b>
5.1	Bayesian analysis of time series . . . . .	73
5.2	A hierarchical linear regression model . . . . .	78
5.3	Convergence analysis . . . . .	81
5.4	A look to the posterior densities . . . . .	84
<b>6</b>	<b>Conclusions</b>	<b>87</b>
	<b>Appendix: R codes</b>	<b>91</b>
	<b>Ringraziamenti</b>	<b>95</b>
	<b>Bibliography</b>	<b>96</b>

# List of Figures

1.1	An example of source-detector map. . . . .	6
1.2	The emission/detection of NIR waves for the three types of NIRS systems. . . . .	8
1.3	Framework of the multi-distance source-detector approach. . .	11
1.4	Motion Artefact corrected trough different techniques. . . . .	13
1.5	The hemodynamic response function. . . . .	16
1.6	Main panel of NIRS-SPM. . . . .	18
1.7	An example of channels MNI coordinates projected to a rendered brain. . . . .	19
1.8	An example of design matrix built by NIRS-SPM. . . . .	20
1.9	A typical output of NIRS-SPM. . . . .	23
1.10	An example of P-values from Shapiro-Wilk tests on errors originated by the GLM. . . . .	24
2.1	Temporal configuration of the right hand grip experiment. . .	25
2.2	An example of in vivo data, from datasets INV1 and INV2. . .	28
2.3	Means of O <sub>2</sub> Hb and HHb concentration during trials for in vivo data 0173, 0176, 0179, 0182. . . . .	30
2.4	Means of O <sub>2</sub> Hb and HHb concentration during trials for in vivo data 0185, 0188, 0191, 0197. . . . .	31
2.5	Means of O <sub>2</sub> Hb and HHb concentration during trials for in vivo data 0200, 0203, 0206, 0209. . . . .	32
2.6	Means of O <sub>2</sub> Hb and HHb concentration during trials for synthetic data. . . . .	36
3.1	Boxplots on AUC, divided by channels and by trials. . . . .	40

---

3.2	Clear examples of anomalous channels. . . . .	41
3.3	AUC sample mean vs standard deviation for subj. 0173, and related Tukey depth. . . . .	43
3.4	Sample Mean vs Log(Std. Dev.) for subjects 0173, 0176, 0179, 0182, 0185, 0188. . . . .	45
3.5	Sample Mean vs Log(Std. Dev.) for subjects 0191, 0197, 0200, 0203, 0206, 0209. . . . .	46
4.1	Regressors for O <sub>2</sub> Hb and HHb concentrations. . . . .	48
4.2	Comparison between fitted data in two approaches. . . . .	49
4.3	Gaussianity P-values for $\hat{\beta}_{rest}^{i,k}$ , $\hat{\beta}_{task}^{i,k}$ and $\hat{\beta}_{task}^{i,k} - \hat{\beta}_{rest}^{i,k}$ for the deeper layer of INV1, O <sub>2</sub> Hb. . . . .	51
4.4	Boxplots of contrasts in right and left hemispheres, for each subject. . . . .	52
4.5	Activation maps for synthetic data, EXP1. . . . .	55
4.6	Activation map for synthetic data, EXP2. . . . .	56
4.7	Activation maps for in vivo data 0173, 0176, 0179. . . . .	58
4.8	Activation maps for in vivo data 0182, 0185, 0188. . . . .	59
4.9	Activation maps for in vivo data 0191, 0197, 0200. . . . .	60
4.10	Activation maps for in vivo data 0203, 0206, 0209. . . . .	61
4.11	K-means activation for EXP1. . . . .	64
4.12	K-means activation for EXP2. . . . .	65
4.13	Folded data, k-means and activation map for a noisy subject. . . . .	66
4.14	K-means activation for some of in vivo data. . . . .	67
4.15	Group analysis maps calculated on 120 trials. . . . .	69
4.16	Group analysis maps obtained trough mean of P-values. . . . .	70
4.17	Group analysis maps obtained trough median of P-values. . . . .	72
4.18	Group analysis maps obtained trough median of P-values for INV1. . . . .	72
5.1	Traceplot, Autocorrelation function and posterior densities for $\beta_1$ of not-activated channels (channels 4, 6, 10, 14). . . . .	75
5.2	Traceplot, Autocorrelation function and posterior densities for $\beta_1$ of activated channels (channels 17, 21, 25, 29). . . . .	76
5.3	HPD intervals for $\beta_1$ in each channel. . . . .	77



---

5.4	Length of HPD intervals for $\beta_1$ in each channel. . . . .	78
5.5	The regressor, <i>rest</i> . . . . .	79
5.6	Geweke plot for $\mu_1$ in two channels. . . . .	81
5.7	Traceplot and autocorrelation plot for $\mu_1$ in two channels. . . . .	83
5.8	Evolution in time of the sample quantiles of $\mu_1$ for two channels. . . . .	84
5.9	Posterior densities for $\mu_1$ in not-activated channels. . . . .	85
5.10	Posterior densities for $\mu_1$ in activated channels. . . . .	86



## Sommario

Il presente lavoro tratta dell'analisi statistica di dati provenienti da spettroscopie del vicino infrarosso (NIRS) eseguite al cervello. La NIRS è una tecnica ottica che consente di ricostruire nel tempo la concentrazione di emoglobina in più punti del cervello chiamati "canali". Il nostro obiettivo consiste nell'analizzare l'andamento dell'emoglobina in ogni canale per valutare in quali di questi il cervello è attivo durante un certo esperimento. Questa operazione è complicata a causa dell'alta variabilità tra soggetti e della presenza di diversi rumori (fisiologici, di misura e dovuti alla configurazione dell'esperimento). Per questo motivo un filtraggio dei dati e un'analisi statistica degli stessi sono indispensabili per una corretta classificazione dei canali. In questo lavoro suggeriamo un metodo per determinare quali canali andrebbero esclusi dalle analisi a causa dell'eccessivo rumore. Tale metodo si basa sull'analisi delle aree sotto la curva (AUC).

Uno dei metodi statistici più comuni in letteratura per individuare le aree attive prevede l'adattamento di un modello di regressione lineare che utilizza come regressore una risposta emodinamica ideale. Questo modello presenta però diverse criticità, dovute soprattutto alla forte dipendenza temporale che caratterizza i dati. Per far fronte a queste criticità proponiamo un metodo alternativo, che prende spunto dal modello in letteratura e come esso utilizza un regressore che mima la risposta emodinamica ideale, ma che consente di ottenere per ogni canale un campione di determinate quantità che ne sintetizzano il grado di attivazione. Questo campione è gaussiano e può essere facilmente indagato per ricavare il grado di attivazione di ogni canale. Descriviamo inoltre alcune proposte per un'analisi di gruppo e un approccio bayesiano coerenti col modello sopra esposto.

Proponiamo infine l'utilizzo dell'algoritmo k-medie per la classificazione dei canali. Questo algoritmo segue una un'altra procedura rispetto a quella finora descritta e pertanto costituisce un utile strumento ausiliario e di controllo.

Queste tecniche sono testate su un dataset simulato e su uno proveniente da un esperimento in vivo.



## Abstract

The present work concerns the statistical analysis of NIRS data applied to the brain. The Near Infra-Red Spectroscopy (NIRS) is an optical technique that allows to reconstruct the hemoglobin concentration in time, in some points of the brain indicated as “channels”. Our objective consists in analysing the temporal evolution of hemoglobin in each channel, in order to evaluate where the brain is activated during a certain experiment. This operation is difficult because of the high variability between subjects and because of the presence of many noises (physiological noises, measure noises and experiment errors). For this reason it is necessary to filter data and to perform a statistical analysis. In this work we suggest a method to determine which channels should be excluded from the analysis because of a too high noise. This method is based on the analysis of the Area Under the Curve (AUC).

One of the most commonly accepted methods for statistical activation detection consists in using an adapted linear regression model that has as regressor an ideal hemodynamic response. However this model presents several criticalities, mainly due to the high temporal correlation that afflicts data. In order to solve these criticalities we propose an alternative method, that takes advantage from a regressor imitating the ideal hemodynamic response, as happens in the current literature, but produces for each channel a sample of activation-related quantities. This sample is gaussian and it can be easily inspected to detect the activation degree of each channel. We also describe some procedures for a group analysis and a bayesian approach that are coherent with the model earlier illustrated.

We propose the k-means clustering algorithm for the channels’ classification. This algorithm follows a new procedure respect of the one described until now and it represents a useful additional tool in activation detection.

These techniques are tested on a simulated dataset and on a dataset from an in vivo experiment.



# Introduzione

Questo lavoro riguarda l'analisi di dati provenienti dall'utilizzo della spettroscopia del vicino infrarosso (NIRS) al cervello.

L'obiettivo primario del nostro studio consiste nel proporre un modello statistico che indaghi i dati valutando l'attività neuronale in diverse zone del cervello.

La letteratura corrente suggerisce diversi metodi per ricercare l'attivazione e a causa della complessità del problema e della relativa novità di questa tecnica ottica non è stata ancora adottata un'unica procedura. Alcune delle metodologie proposte sono piuttosto semplici, altre sono molto più complesse. Tutte presentano alcuni svantaggi e criticità irrisolte.

Una profonda revisione dei metodi usati per l'analisi di dati NIRS è necessaria per proporre un modello che sfrutti le conoscenze pregresse e minimizzi le problematiche esistenti.

L'output finale del nostro modello sarà una mappa della testa che mostra quali aree del cervello sono attivate. Tale mappa dovrà essere chiara e comprensibile anche a personale medico e a utenti con un background non statistico.

Il lavoro che proponiamo si articola nelle seguenti parti.

Nel Capitolo 1 proponiamo un'introduzione al problema dell'analisi di dati NIRS. Viene presentata la tecnica della spettroscopia del vicino infrarosso, con una breve descrizione delle sue applicazioni in ambito scientifico. Riportiamo poi una sintesi delle tecniche utilizzate in letteratura per l'analisi di dati NIRS e descriviamo la procedura eseguita sui dati da uno dei software più utilizzati in questo campo, il software NIRS-SPM.

Nel secondo capitolo presentiamo i dataset, precisandone le caratteristiche e il processo di acquisizione.

Nel Capitolo 3 riportiamo le analisi condotte sulle aree sotto la curva (AUC). Indaghiamo queste quantità con un duplice obiettivo: cerchiamo da una parte di trovare le zone attivate, dall'altra di determinare quali canali sono da escludere a causa dell'eccessivo rumore.

Il Capitolo 4 descrive una nuova procedura per rivelare le aree cerebrali attivate. Tale procedura si basa su modelli di regressione lineari. Questo

capitolo presenta una sezione di presentazione dei modelli lineari (4.1), una sezione riportante le analisi condotte sui parametri ottenuti (4.2), una sezione sull'algoritmo di k-medie, proposto come strumento addizionale e di controllo (4.4), e una sezione sulle analisi di gruppo (4.5).

Infine nel Capitolo 5 proponiamo un approccio bayesiano, con una sezione sull'analisi dei dati come serie temporale e una in cui descriviamo un modello bayesiano gerarchico, che conferma e arricchisce i risultati ottenuti tramite l'analisi frequentista.

Questo lavoro è stato condotto in collaborazione con il Dipartimento di Fisica del Politecnico di Milano.



# Introduction

The present work concerns the analysis of data from the application of Near Infrared Spectroscopy (NIRS) to the brain.

The main objective of our studies is the proposal of a statistical model on NIRS data for the detection of neural activation in the brain.

The current literature suggests different methods for activation detection, and a common accepted procedure is not yet defined because of the complexity of the matter and the relative novelty of the technique. Some of the frameworks proposed in recent years are quite simple, others are much more complex. Each of them presents some drawbacks or unresolved criticalities.

A good review of the methods used on NIRS data since the beginnings is necessary to propose a model that takes advantage from previous knowledge and minimizes the unsolved questions.

The final output of our model will be a map of the head showing which areas of the brain are activated. This map should be understandable to medical personnel and people without a mathematical background.

This work is composed by the following parts.

In Chapter 1 an introduction to the problem is proposed, with a section describing NIRS technique (Section 1.1), a review of the present literature (Section 1.2) and a brief dissertation about one of the most commonly used software for NIRS data analysis, NIRS-SPM (Section 1.3).

In Chapter 2 datasets are presented, with explanations about the used pre-processing algorithm.

Chapter 3 reports analysis on Area Under the Curves (AUC) of our data. We inspect this quantity in order to perform activation detection (Section 3.1) and outlier detection (Section 3.2).

In Chapter 4 we propose a new procedure for activation detection, based on linear regression models. This chapter is organized with a section on the linear regression models (Section 4.1), a section with analysis on the parameters of the models (Section 4.2), a section on the resulting activation maps (Section 4.3), a section on k-means clustering algorithm used as an additional activation detection technique (Section 4.4) and a section on group analysis (Section 4.5).

A bayesian approach is proposed in Chapter 5, with time series analysis (Section 5.1) and a bayesian hierarchical linear regression model (Section 5.2). Convergence diagnostic is reported in Section 5.3, while a bayesian criterion for activation detection is introduced in Section 5.4.

This work was conducted in collaboration with the Physics Department of the Politecnico of Milan.

# Chapter 1

## Introduction to NIRS

### 1.1 An optical method with several applications

Near Infrared Spectroscopy (NIRS) is an optic technique that uses optic radiations from near infra-red spectrum (i.e. radiations with wavelengths from 650 to 950 nm) to inspect the composition of materials.

This technology was introduced in the '70s in agriculture and food science, to estimate the level of humidity and the chemical composition of foodstuffs and animal feeds. At the beginning it was used in a few contexts, because its instrumentation was expensive and there were many difficulties in handling and evaluating results. Then, with electronics and computers development, managing data became easy and the cost of NIRS technology decreased. Thus NIRS found new applications in different sectors, such as astronomy, agrochemical quality control, material science, combustion research, polymer and plastic moisture analysis, cosmetics and pharmaceutical.

In the last few decades NIRS began to be employed also in medical diagnostics and medicine research, with applications in sports medicine, ergonomics, neonatal research and childhood brain development analysis, urology, neurology and functional neuroimaging.

NIRS applied to functional neuroimaging is called functional Near Infrared Spectroscopy (fNIRS), because it aims to probe the function of the brain. Many researches have been conducted in this field, with the objective, for example, to inspect the cerebral response to visual, auditory or somatosensory

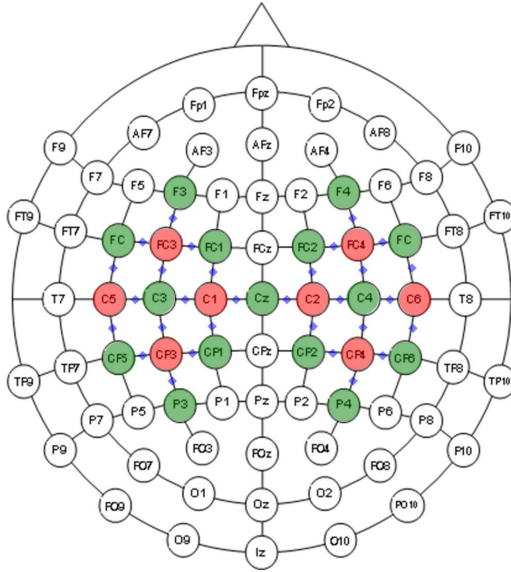


Figure 1.1: An example of source-detector map. Head is seen from above. Sources are in red, detectors are in green. Using this configuration, hemoglobin concentrations are acquired for each of the 30 channels between a source and a detector. Channels are marked in blue.

stimuli, or to study brain activity during speech recognition or cognitive processes. NIRS in fact allows to monitor changes in oxygenated hemoglobin ( $O_2Hb$ ) and deoxygenated hemoglobin (HHb) caused by neural activity.

fNIRS was also employed in clinical studies on patients with Alzheimer disease, epilepsy, depression, schizophrenia and other diseases, and during rehabilitation after an ischemia or cerebral damages. These studies aimed to detect and understand cerebral alterations caused by these pathologies.

Nowadays fNIRS has become a complementary and alternative technique to functional Magnetic Resonance Imaging (fMRI), with the advantages, respect to fMRI, of higher temporal resolution, excellent sensitivity to hemoglobin (fMRI can only monitor concentration changes in HHb), fewer motion artefacts and a cheaper and more portable technology.

fNIRS is based on the optical absorption/transparency of blood and biological tissues. In fact the skin, skull and tissues are transparent to NIR wavelengths, while  $O_2Hb$  and HHb absorb these spectra.

During the experiment, the patient wears a helmet with a variable number of sources and detectors. Photons emitted in the NIR range by sources penetrate in the head, being absorbed, transmitted or reflected depending on the optical properties of the medium they pass through. Reflected photons are then absorbed by detectors, placed some centimetres apart from the emission

points. Highly sensitive detectors are required, since the intensity of the reflected light is very low. In fact, not to damage tissues, the NIR emission is about a few  $\text{mW} \cdot \text{mm}^{-2}$ , in order that the skin temperature increase is less than  $0.5^\circ\text{C}$ .

Hemoglobin is the main absorber at NIR wavelengths, thus from the reflected spectra registration it is possible to acquire its concentration. Moreover the difference in the NIR absorption spectra of  $\text{O}_2\text{Hb}$  and  $\text{HHb}$  allows the separate measurement of the concentrations of these two species: to achieve this goal, it is sufficient to perform NIRS measurements at two different wavelengths.

According to some authors (Boas et al., 2004), wavelengths should be chosen in the range of 670 to 900 nm, as shorter wavelengths are too strongly absorbed by hemoglobin, and longer wavelengths are strongly absorbed by water. The maximal distance between a source and a detector is usually around 3.5-4 cm, allowing photons to reach a depth of 3-3.5 cm.

While the spatial resolution is moderate (subcentimetre to fewcentimetre, limited by the diffusive nature of photon transport) and it degrades rapidly with increasing depth in the brain, the temporal resolution of hemoglobin detection with NIRS is not acquisition limited and can be up to milliseconds, much faster than the hemodynamic response itself.

There are three main types of NIRS technologies. All the three methods allows a direct determination of  $\text{O}_2\text{Hb}$  and  $\text{HHb}$  concentrations during time. From these time series it is possible also to determine the total hemoglobin concentration ( $\text{tHb}$ ) and the tissue oxygen saturation ( $\text{StO}_2$ ), which are given by:

$$\begin{cases} \text{tHb} = \text{O}_2\text{Hb} + \text{HHb} \\ \text{StO}_2 = 100 \cdot \frac{\text{O}_2\text{Hb}}{\text{tHb}} \end{cases} \quad (1.1)$$

The simplest and the cheapest NIRS system, and for this the most common one, is “continuous wave” (CW) fNIRS. This NIRS system emits waves with constant frequency and amplitude, continuously in time. Absorption changes are determined by measuring the attenuation of incident light. The main drawback of this technology is that it doesn’t allow to define the photon path length, preventing an absolute estimate of the absorption coefficients and

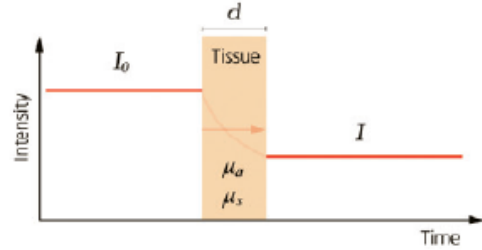
consequently of the hemoglobin concentration.

A more complex and more precise system is “time domain” (TD) fNIRS. In this type of spectroscopy photons are emitted through pulses with a temporal width of some tens of picoseconds. The photons path can be obtained evaluating delay between emission and detection, thus it is possible to reconstruct the depth reached by photons and to determine the absolute absorption coefficients of the crossed media. In this way the absolute concentration values of O<sub>2</sub>Hb and HHb can be retrieved.

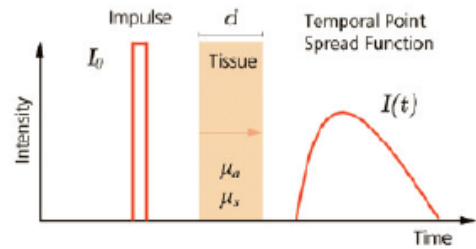
This method is more expensive and technically complex than CW fNIRS, because it requires high-speed sources and detectors. Nevertheless it provides the most information, as well as a good spatial resolution. It also enables the correction of the noise of the superficial layers.

The datasets we use are obtained with this technique.

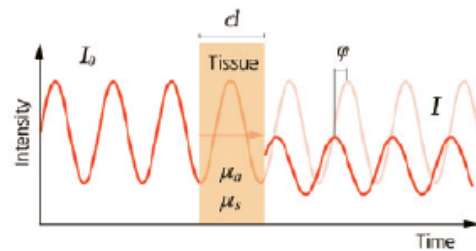
The third NIRS system is “frequency domain” (FD) fNIRS. Sources introduce into the head an amplitude-modulated sinusoid at frequencies in order of tens to hundreds of MHz. These systems record changes in amplitude and phase of the back-scattered signal and, from them, information on the absorption and scattering properties of tissues is acquired. This method requires modulated lasers and phasic measurements, thus it is less portable and more expensive than CW NIRS systems. Even if the frequency range, being limited, cannot cover the infinite frequency modulation of a time resolved



(a) *Continuous wave NIRS.*



(b) *Time domain NIRS.*



(c) *Frequency domain NIRS.*

Figure 1.2: The emission/detection of NIR waves for the three types of NIRS systems, Scholkmann, Wolf (2012).

pulse, the information obtained with this method is in principle the same of the TD approach.

The behaviour of the three NIRS systems in time is shown in Fig. 1.2.

## 1.2 The State of the Art

Using NIRS to measure hemoglobin concentration in the brain has a lot of advantages. It is a very safe and non-invasive technique, that can be used on children and elderly people, without contraindications. In literature there are studies on neonates a few hours old, for example.

Moreover NIRS is relatively cheap, easy to use and to move. It doesn't need for special infrastructure or trained personnel, thus it can be used on people far from urban area (for example, there are studies on children in rural regions of Africa), and on bedridden patients.

Finally, NIRS has a high resolution in time. It allows to study the temporal behaviour of the hemodynamic response to neural activation, with high temporal precision.

This technique presents also some disadvantages, including a modest spatial resolution (1-3 cm), a limited penetration depth and the presence of noises.

fNIRS data are usually corrupted by different types of noise: physiological noise (such as interferences provoked by heartbeat, breathing, blood pressure), instrument noise (such as shot noise, with a Poisson distribution, and measurement noise, which is assumed to be a Gaussian white noise) and experiment errors (motion artefacts, potential sensitivity to hair absorption, interferences from external sources). Thus it is advantageous to pre-process data, in order to remove some interferences and to improve the spatial sensitivity of registered measurements. After subtracting noise, data are usually analysed to detect active areas of the brain.

Many methods have been proposed to filter and analyse fNIRS data. We report now a brief summary on the most important results about preprocessing (physiological noise and motion artefact correction) and active channels detection.

## Systemic interference correction

Noise caused by cardiac activity, respiration, blood pressure variations including Mayer waves (with an approximately 10 s period) and other slower variations is called *systemic physiological interference*. This interference can arise from two spatial sources: the superficial layers (such as scalp and skull) and the brain layer. The contribution of systemic interference to NIRS signal is intensified because of the “back reflection geometry” of the measurements. In fact light is both emitted and received at the scalp surface, thus photons reflected from brain tissue must travel through the skin, skull and dura before reaching a detector on the scalp surface. This increases the sensitivity of NIRS measurements to systemic oscillations occurring in the superficial layers. For this reason systemic interference from superficial layers often results as the dominating noise component.

Several methods have been used in the literature to reduce this type of noise in NIRS data. One of the most common technique is low-pass filtering (e.g. Franceschini, Boas, 2004). This approach suits perfectly the suppression of high frequency interferences (such as noise from heartbeat), but it doesn't remove noise from respiration and other low frequency phenomena. If the noise has the same frequency of the hemodynamic response, a frequency-based filtering is also inappropriate, because it may distort the information on cerebral activity.

Other methods for reduction of systemic physiological interference include wavelet filtering (e.g. Lina et al., 2010) and Principal Component Analysis (e.g. Franceschini et al., 2006).

Another approach that can be adopted takes advantage of the different spatial locality between hemodynamic response and systemic interference. In fact the former is expected to be localized in a limited space (dependent on the experiment), while the latter extends globally. Thus the signal from a not-activated area should be similar to systemic noise. Direct subtraction of a signal from a not-activated channel was proposed by Franceschini, Boas (2004).

Another way to isolate noise from superficial layers is “multi-distance” approach. Photons propagate through the head travelling along a zig-zag path



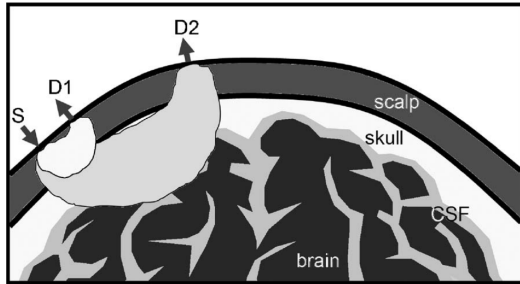


Figure 1.3: Multi-distance source-detector approach. Superficial layer interference acquired from S-D1 are used to estimate systemic interference in S-D2 (Zhang et al., 2007).

until they are detected. The collective photon propagation follows a half-moon pattern, as shown in Fig. 1.3. Depth reached by photons depends on the separation of source and detector. With an appropriate source and detector placement, we can use the signal from close source-detector, dependent on noise only, to eliminate systemic interference in signal from distant source-detector, with the assumption that a common systemic interference is present in both channel measurements. This approach is applied, for example, in Gagnon et al. (2012); Saager, Berger (2005).

Several algorithms have been developed to use small separation signals as regressors to filter the systemic interference in the longer source-detector measurements. These include linear minimum mean square estimation (Saager, Berger, 2005), adaptive filtering (Zhang et al., 2007) and state-space modeling with Kalman filter estimation (Gagnon et al., 2011, 2012).

The most critical point in multi-distance approach is the difficulty in determining photons path length in each head layer. Many studies tried to solve this problem using Monte Carlo simulations to investigate the partial optical path lengths for each layer, in order to fix appropriate multi-distance set-ups (Umeyama, Yamada, 2014).

Finally, we underline that TD fNIRS produces data with a systemic noise much lower than CW NIRS. In fact with this technique it is possible to estimate the superficial hemodynamics and to distinguish between photons from deep and shallow layers.

## Motion artefacts correction

Motion artefact is another type of noise that corrupts fNIRS data. It can be distinguished from hemodynamic response by its rapid occurrence and

larger amplitude, appearing as a sharp spike in the signal, sometimes followed by a shift in the baseline value. It differs from systemic noise because of its irregularity.

Motion artefacts are provoked by a sudden increase or decrease in the measured light attenuation, depending on a lack of contact from the source or the detector and the skin. Gravitational effects produced by head movement may also result in changes in blood flow in parts of the head, interfering with experiment-related hemodynamic response.

Optodes are usually fitted firmly to the head using a cap to minimize the effects of motion, and optical fibers are placed at right angles to the scalp surface.

Even though fNIRS is less sensitive to motion artefacts than other neuroimaging techniques, such as fMRI, motion artefacts cannot always be eliminated entirely. This happens especially in studies on children, animals or patients unable to avoid movements deliberately.

In order to reduce motion artefacts in fNIRS data, many approaches have been developed. Some of these detect motion artefact exclusively through an analysis of the temporal characteristics of the signal. Others methods, instead, use additional equipment (requiring an alteration of experimental design) to get an input signal that is highly correlated with motion artefact but not with hemodynamic response. Such an input signal can be obtained through a specific disposition of channels (for example, co-located channels), or an additional sensor to detect movements (typically, an accelerometer).

In co-located channels configuration, source-detector pairs are on the same position. Since photon penetration depth depends on source-detector separation, if source and detector overlap the registered signal is superficial noise. Thus with co-located channels it is possible to measure little or no physiological signal, registering the signal fluctuations caused by the shift between the fiber and the skin.

Trough an accelerometer or the co-located channels configuration, motion can be easily identified. After the identification, signals can be corrected in different ways (e.g. adaptive filters, wavelet filtering, Independent Component Analysis, linear regression). These class of methods has the disadvantage of needing specific additional equipment, which is not always available in NIRS

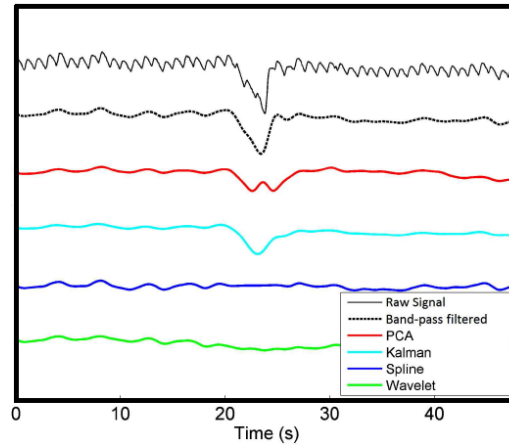


Figure 1.4: Motion Artefact corrected trough different techniques (Cooper et al., 2012).

devices.

In the literature we find another approach to this problem: it aims to remove motion artefacts without an external measure of motion. These techniques are based on an analysis of signal mutations in amplitude and frequency, because rapid changes are usually provoked by motion artefacts. Some methods used for this approach are based on Wiener filtering (Izzetoglu et al., 2005), Kalman filtering (Izzetoglu et al., 2010), correlation-based signal improvement method (Cui et al., 2010), Wavelet-based filtering (Sato et al., 2006) and moving standard deviation with spline interpolation (Scholkmann et al., 2010).

The Wiener filter requires two calibrations measurements before the actual one: one measurement with motion artefact and one without it. Thus it can't be applied if it is not possible to avoid motion artefact during the calibration period (e.g. fNIRS on neonates).

Correlation-based signal improvement takes advantage of the negative correlation between  $O_2Hb$  and  $HHb$ , assuming that positive or not strongly negative correlated signals are substantial noise. This method suggests to correct the original signal with a linear combination of  $O_2Hb$  and  $HHb$  that maximizes the negative correlation between the two hemoglobins.

Wavelet transform decomposes signals into global trends, hemodynamic signals and uncorrelated noise components as distinct scales. Motion artefact

usually provokes a sudden change in the signal frequency, thus wavelet transformation can be used to remove motion artefact, deleting the coefficients which correspond to motion artefact in the wavelet domain.

Moving standard deviations with spline interpolation algorithm detects motion artifacts calculating moving standard deviation (MSD): motion artefact is assumed when MSD exceeds a threshold. Then a cubic spline interpolation of motion artefact segments is subtracted to the original signal, smoothing and detrending it.

Fig. 1.4 shows how motion artefact can be corrected through different techniques.

## Statistical Inference for brain activation detection

In the first studies about fNIRS, brain activation was detected through a simple visual inspection of hemodynamic signals (e.g. Murata et al., 2002). Another simple procedure that was initially adopted (Benaron et al., 2000) was the control of hemoglobin concentration increase: if signal exceeded 2 standard deviation from the mean, the activation was assumed<sup>1</sup>.

These subjective or heuristic approaches can be inaccurate, especially if the signal is highly corrupted by interferences and noises. Statistical inference and a more organised procedure then become essential for neural activation detection in fNIRS data.

Many methods have been proposed in different studies and even now there isn't a unique way to detect activation (for a review, see Tak, Ye, 2014). Suitable statistics were calculated to test the difference between means of two groups: the hemoglobin concentration during task and the hemoglobin concentration during rest. In these analysis one hypothesis test was implemented for each channel and P-values were adjusted with Bonferroni correction.

One-way or multi-way ANOVA was also employed to compare different groups of concentrations. Typically, average values are used in this analysis not to make assumptions on the exact shape or the evolution in time of

---

<sup>1</sup>In order to reduce noise, this analysis was performed after the subtraction of a baseline, assuming a globally distribution of noise and its independence from brain activation

hemoglobin signals.

White et al. (2009) studied spatial correlation between different channels. Correlation between a benchmark (activated) channel and the other time traces was analysed, founding the highest correlation between activated channels.

In these simple analysis the information on timing and shape of the hemodynamic response is usually lost. Neural activation provokes a specific hemoglobin alteration: its peculiarity is not just in absolute values, but in a particular evolution in time. Thus forgetting about the correlation structure of data can be inaccurate, because the hypothesis of independence of data, that is often assumed, is not verified, and also limiting, because some information on activation is lost. The strong dependence of measures, that can be a critical point to treat, is at the same time a source of knowledge. Thus more complex methods have been applied, taking advantages from evolution in time of data.

Trough Fourier analysis it is possible to compare time courses. This analysis is based on the intuition that activated signals must have a peak at the task frequency. The main drawback on Fourier approach is that it is hardly applied to non-periodic tasks such as event-related paradigm.

Then the Generalized Linear model (GLM), that was used in fMRI analysis, was proposed for fNIRS, because of the similarities of the two technologies. Numerous studies have been presented to exploit this method.

With GLM, hemoglobin concentration is seen as a linear combination of some predictors plus an error term. Predictors usually consist of task-related boxcar functions. In our analysis we will use, as predictors, convolutions between a boxcar function and the hemodynamic response function (HRF).

These convolutions represent a sort of temporal evolution of the “ideal” hemoglobin concentration in an active channel. In fact neuronal activity consumes oxygen carried by hemoglobin, provoking an increase of the blood flux. This blood flux variation is called hemodynamic response and it reaches a peak after 4-5 s, then it decreases to the initial level (usually passing below it). Fig. 1.5 shows the hemodynamic response function, that describes this phenomenon.

Thus in the GLM a signal is expected to depend on predictors if it belongs

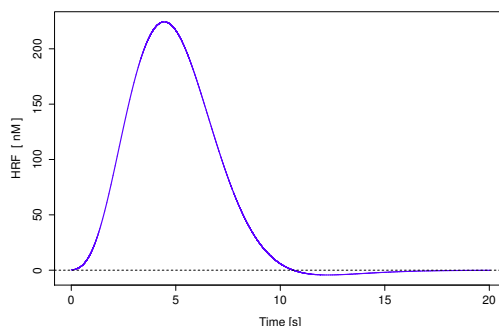


Figure 1.5: The hemodynamic response function.

to an active channel, while an independence will suggest no activation.

The error covariance matrix is not an identity matrix (as in a linear regression model), because errors are not independent. This makes inference on parameters more complicated than in linear models, because an appropriate test statistic should be calculated in a more sophisticated way (for more details, see Section 1.3).

Several methodologies have been developed for fNIRS users to process functional optical data. The first public domain software package for fNIRS data analysis was HomER<sup>2</sup> (acronym for Hemodynamic Evoked Response). The software provides a graphical user interface and MATLAB<sup>3</sup> scripts for both the preprocessing and the standard statistics on fNIRS data. HomER has been upgraded and the new release HomER2 more easily supports group analyses and re-configuration of the processing stream, and it integrates users algorithms into the processing stream.

Another free software is Functional Optical Signal Analysis (fOSA<sup>4</sup>), which offers MATLAB based functions for a basic analysis of fNIRS data, incorporating several filters for signal denoising and providing also the Statistical Parametric Mapping (SPM) methodology for statistical analysis based on the GLM approach.

---

<sup>2</sup><http://www.nmr.mgh.harvard.edu/PMI/>, distributed by Massachusetts General Hospital.

<sup>3</sup>MATLAB and Statistics Toolbox Release 2012, The MathWorks, Inc., Natick, Massachusetts, USA.

<sup>4</sup>Koh et al. (2007)

More focused on the development of SPM routines is the non-commercial MATLAB-based software NIRS-SPM<sup>5</sup>. A novelty introduced by this program is represented by a voxel based alignment between interpolated maps instead of an inter-subjects realignment of optodes, in order to facilitate the group analysis.

Another software is NIRS analysis package (NAP<sup>6</sup>) which allows noise removal and GLM analysis, as well as anatomical registration of the measurements.

fNIRSOFT<sup>7</sup> is a stand-alone software to process, analyse and visualize fNIRS signals through a graphical user interface and/or scripting distributed by BIOPAC Systems, Inc.

Finally POTATo<sup>8</sup> (Platform for Optical Topography Analysis Tools) is a software package for fNIRS signal processing and analysis, developed by Hitachi, Ltd.

In order to better understand the GLM method and a typical existing approach to fNIRS data, we examine in depth the software NIRS-SPM, illustrating the steps it performs. In this way some fundamental idea will be clear, as well as some critical points that we'll try to solve in the next chapters.

## 1.3 The software NIRS-SPM

NIRS-SPM is a public domain toolbox for the analysis of fNIRS signals. It is based on SPM<sup>9</sup> and MATLAB, and it allows a stand alone or a combined fNIRS-fMRI data analysis. With its packages it is possible to filter the data in different ways and to perform a statistical analysis, building a GLM and obtaining the related activation maps.

Analysis takes place in six stages: (1) converting the optical densities to concentration changes of O<sub>2</sub>Hb and HHb, (2) spatial registration of channels

---

<sup>5</sup><http://bisp.kaist.ac.kr/NIRS-SPM.html>

<sup>6</sup>Fekete et al. (2011)

<sup>7</sup><http://www.biopac.com/fNIR-Software-Professional-Edition>

<sup>8</sup>[http://www.hitachi.co.jp/products/ot/analyze/kaiseki\\_en.html](http://www.hitachi.co.jp/products/ot/analyze/kaiseki_en.html)

<sup>9</sup>Wellcome Department of Cognitive Neurology, London, UK.

positions, (3) model specification, (4) detrending the unwanted global trends using wavelet-MDL algorithm or discrete cosine transform based high pass filtering, (5) temporal correlation estimation from precoloring or prewhitening method, (6) statistical inference and visualization of activated region from various functional contrasts ( $O_2Hb$ ,  $HHb$ ,  $tHb$ ,  $StO_2$ . For a definition of these quantities, see (1.1)).

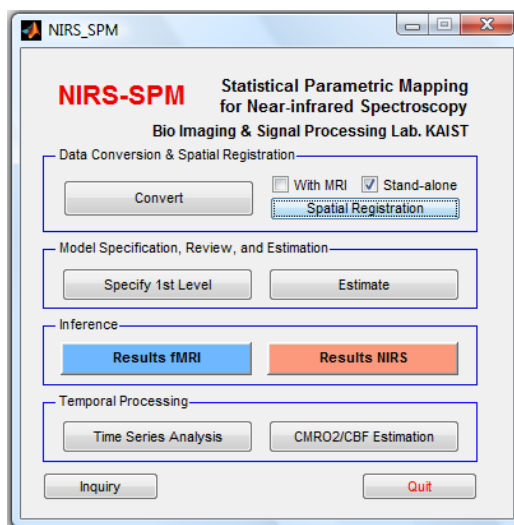


Figure 1.6: Main panel of NIRS-SPM.

(1) The first step allows conversion of the optical densities, that are unitless quantities, in hemoglobin concentration changes in  $\mu M$ . They are calculated using the modified Beer-Lambert law:

$$\Delta OD = [\varepsilon_{O_2Hb} \Delta C_{O_2Hb} + \varepsilon_{HHb} \Delta C_{HHb}] \cdot d \cdot l, \quad (1.2)$$

where  $\Delta OD$  is the optical density variation,  $\varepsilon_{O_2Hb}$  and  $\varepsilon_{HHb}$  [ $(\mu M \cdot mm)^{-1}$ ] are the extinction coefficients of  $O_2Hb$  and  $HHb$ ,  $C_{O_2Hb}$  and  $C_{HHb}$  are the hemoglobin concentration changes,  $d$  is the unitless differential path length factor and  $l$  [mm] is the distance between the source and the detector. NIRS-SPM can analyse the optical density of various formats from different NIRS systems.

(2) NIRS-SPM allows the spatial registration of fNIRS channels to Montreal Neurological Institute (MNI) space. The MNI is a coordinate system used to map the location of brain structures independent from individual differences



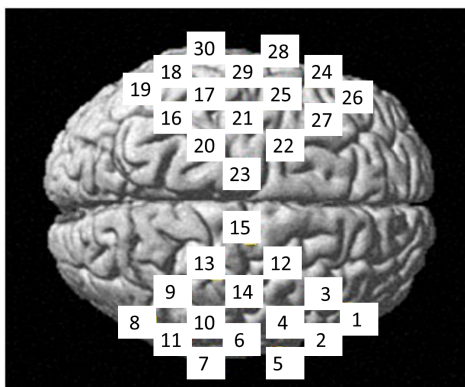


Figure 1.7: An example of channels MNI coordinates projected to a rendered brain. The brain is seen from above: the face of the subject is on the right.

in the size and overall shape of the brain. This allows a standardization of brains from different subjects and permits their comparison and an eventual group analysis. The spatial registration can be done with an additional alignment with MRI data, or standalone. In order to do it, it is possible to insert channels or optodes MNI coordinates or real coordinates. The fNIRS channels positions are then localized onto the cerebral cortex of an anatomical MR image, and they are saved for later analysis (an example of channels locations on a “standardized” brain is reported in Fig. 1.7).

(3) In model specification we can choose the design matrix that will be used for the GLM. We do this specifying:

- the interscan interval (in seconds) or, equivalently, the sampling frequency (in Herz);
- the names, onsets and durations of each event (in our data the two repeated events will always be *rest* and *task*);
- the basis functions used to build the predictors. We can choose the Hemodynamic Response Function (HRF) or HRF with time and/or dispersion derivatives. In the simplest case each column of the design matrix contains the predicted hemodynamic response for one experimental condition over time (in our analysis the two experimental conditions will be *rest* and *task*). With the inclusion of the HRF’s first and second temporal derivative, a design matrix with more columns is obtained. This kind of matrix has been proposed to address inter-individual differences regarding the HRF’s latency and dispersion.

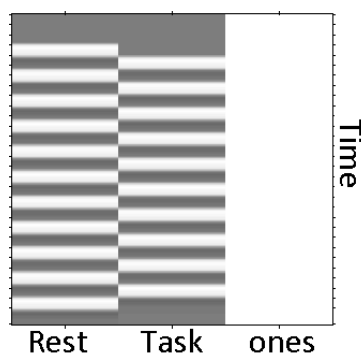


Figure 1.8: An example of design matrix built by NIRS-SPM. The alternation between colors derives from the convolution between scales functions and the HRF.

(4) In fNIRS experiments, there often exist global drifts of the optical signal measurements for a variety of reasons, including subject movement during the experiment, vaso-motion, blood pressure variation, long-term physiological changes or instrumental instability. Moreover, the amplitude of the global drift is often comparable to that of a signal from an activated channel.

In order to eliminate the global trend and to improve the signal-to-noise ratio, two different high-pass filters are implemented: discrete cosine transform (DCT) based detrending algorithm and Wavelet detrending algorithm. If we choose the latter, Wavelet transform is applied to decompose fNIRS measurements into global trends, hemodynamic signals and uncorrelated noise components as distinct scales.

(5) After detrending, temporal correlation continues to exist in fNIRS data. This means that the signal at the specific time is highly correlated with its temporal neighbours. This generates problems in statistical inference, because the hypothesis of independence of the observations falls down. NIRS-SPM gives two options to address this problem, both initially proposed for fMRI: precoloring method and prewhitening method.

In the former, the intrinsic temporal correlations are swamped by an imposed temporal correlation structure, by smoothing the data with a temporal filter that will attenuate high frequency components. It's a low-pass filter. The shape of this filter can be Gaussian or HRF (differences are slight).

Prewhitening method, instead, attempts to regress out the unknown

autocorrelations through an AR(1) model. If  $y_t$  is hemoglobin concentration at time  $t$ ,  $(X)_t$  is the  $t$ -th row of the design matrix and  $\varepsilon_t$  and  $v_t$  are Gaussian white noises, we can set the following linear model and autoregressive model:

$$\begin{cases} y_t = (X)_t \boldsymbol{\beta} + \varepsilon_t \\ y_t = \rho y_{t-1} + v_t \end{cases} \quad (1.3)$$

From this we obtain:

$$y_t - \rho y_{t-1} = ((X)_t - \rho(X)_{t-1}) \boldsymbol{\beta} + (\varepsilon_t - \rho \varepsilon_{t-1}),$$

and if we redefine each variable as follows:

$$y_t^* = y_t - \rho y_{t-1}, \quad (X^*)_t = (X)_t - \rho(X)_{t-1}, \quad u_t = \varepsilon_t - \rho \varepsilon_{t-1},$$

we can build the following linear model, with a reduction in correlation:

$$y_t^* = (X^*)_t \boldsymbol{\beta} + u_t. \quad (1.4)$$

(6) After filtering algorithms, a GLM is implemented. If  $X \in \mathbb{R}^{n \times (r+1)}$  is the design matrix built in (3),  $\mathbf{y}^i \in \mathbb{R}^n$  is the hemoglobin concentration in channel  $i$  and  $\boldsymbol{\varepsilon}^i \in \mathbb{R}^n$  is a term of error, the model is:

$$\mathbf{y}^i = X \boldsymbol{\beta}^i + \boldsymbol{\varepsilon}^i. \quad (1.5)$$

The unknown coefficients  $\boldsymbol{\beta}^i \in \mathbb{R}^{r+1}$  are estimated with the Least Square unbiased estimates, given by

$$\hat{\boldsymbol{\beta}}^i = X^\dagger \mathbf{y}^i,$$

where  $X^\dagger = (X^T X)^{-1} X^T$  defines the Moore-Penrose pseudo-inverse matrix of  $X$ .

Then the gaussianity of the errors  $\boldsymbol{\varepsilon}^i$  is assumed. We can't assume the independence of errors in time, but we hypothesize that different channels have the same correlation structure, defining a temporal correlation matrix,  $\Lambda$ , common for all the channels. Thus we assume  $\boldsymbol{\varepsilon}^i \sim \mathcal{N}_n(\mathbf{0}, \sigma_i^2 \Lambda)$ , where  $\Lambda$  is the common correlation matrix and  $\sigma_i^2$  is the variance in the  $i$ -th channel, and we find  $\hat{\boldsymbol{\beta}}^i \sim \mathcal{N}_{r+1}(\boldsymbol{\beta}^i, \sigma_i^2 (X^\dagger \Lambda (X^\dagger)^T))$ .

An hypothesis test is implemented on a linear combination of the coefficients estimates: under the null hypothesis  $\mathbf{c}^T \hat{\boldsymbol{\beta}}^i \sim \mathcal{N}(0, \mathbf{C}_{\hat{\boldsymbol{\beta}}^i})$ , with  $\mathbf{c}$  contrast vector and  $\mathbf{C}_{\hat{\boldsymbol{\beta}}^i} = \sigma_i^2 (\mathbf{c}^T X^\dagger \Lambda (X^\dagger)^T \mathbf{c})$ . The software calculates the following statistics:

$$T_i = \frac{\mathbf{c}^T \hat{\boldsymbol{\beta}}^i}{\sqrt{\hat{\sigma}_i^2 (\mathbf{c}^T X^\dagger \Lambda (X^\dagger)^T \mathbf{c})}}. \quad (1.6)$$

Because of the shape of the correlation matrix  $\Lambda$ , the denominator of (1.6) is not the square root of a  $\chi^2$  distribution. This means that the statistic  $T_i$  of (1.6) is not distributed as a t-student, and we cannot simply make inference by comparing it with a t distribution with  $\text{trace}(\text{RV})$  degrees of freedom, where  $R = I - X(X^T X)^{-1} X^T$ . Thus an approximation for the denominator has to be found.

Friston et al. (2011) proposes to approximate the distribution of the denominator of (1.6) with the square root of a  $\chi^2$ , using the Satterthwaite approximation. This procedure is made imposing:

$$d = \sigma^2 \mathbf{c}^T (X^T X)^{-1} X^T \Lambda X (X^T X)^{-1} \mathbf{c}, \quad (1.7)$$

$$d = ay \quad (1.8)$$

where  $y \sim \chi^2(\nu)$ , with  $\nu$  that has to be estimated.

Note that, for a  $\chi^2(\nu)$  distribution,  $E[y] = \nu$  and  $\text{Var}(y) = 2\nu$ .

The approximation is made by matching the first two moments of  $d$  with the first two moments of  $ay$ :

$$E[d] = a\nu \quad (1.9)$$

$$\text{Var}(d) = a^2 2\nu \quad (1.10)$$

If the correlation matrix  $\Lambda$  is assumed to be known, from (1.9) and (1.10) we get:

$$\nu = \frac{2E[\hat{\sigma}^2]^2}{\text{Var}(\hat{\sigma}^2)}. \quad (1.11)$$

With  $E[\hat{\sigma}^2] = \sigma^2$  and:

$$\begin{aligned} E[e^T e e^T e] &= \text{Var}(e^T e) + (E[e^T e])^2 \\ &= 2\text{trace}(E[ee^T]^2) + \text{trace}(E[ee^T])^2 \\ &= \sigma^4 (2\text{trace}(\text{RV} \text{RV}) + \text{trace}(\text{RV})^2) \end{aligned} \quad (1.12)$$

we have:

$$\begin{aligned}
 \text{Var}(\hat{\sigma}^2) &= E[\hat{\sigma}^4] - E[\hat{\sigma}^2]^2 \\
 &= \frac{\sigma^4(2\text{trace}(RV RV) + \text{trace}(RV)^2)}{\text{trace}(RV)^2} - \sigma^4 \\
 &= \frac{2\sigma^4\text{trace}(RV RV)}{\text{trace}(RV)^2}.
 \end{aligned} \tag{1.13}$$

Using (1.11), we get:

$$\nu = \frac{2E[\hat{\sigma}^2]^2}{\text{Var}[\hat{\sigma}^2]} = \frac{\text{trace}(R\Lambda)^2}{\text{trace}(R\Lambda R\Lambda)}, \tag{1.14}$$

where  $\nu$  approximates the degrees of freedom of the t-student statistic in (1.6).

At this point NIRS-SPM calculates the P-values for which the null hypothesis can be rejected, and it builds the maps.

It uses Euler Characteristic (EC) with Lipschitz Killing Curvature or Sun's tube formula in order to interpolate in the space, getting a high resolution map.

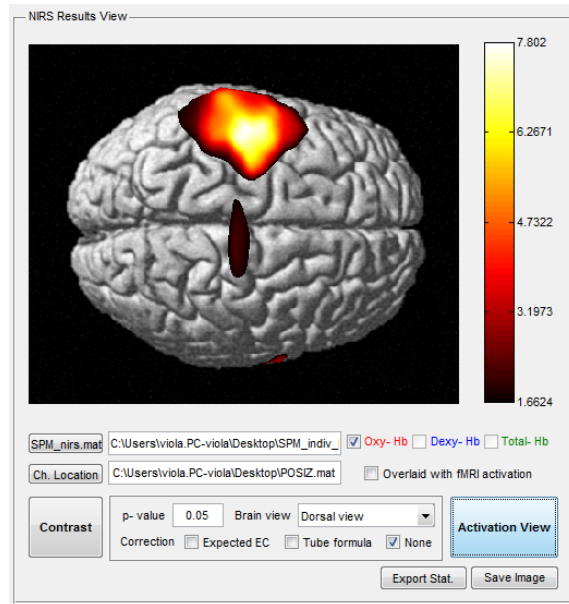


Figure 1.9: A typical output of NIRS-SPM.

An example of a typical NIRS-SPM output is reported in Fig. 1.9.

The most critical points of this approach are the hypothesis on errors.

Of course errors can't be treated as independent, because they belongs to repeated measures in time of the same concentration. This complicates the procedure to find a statistic with a known distribution.

Furthermore, errors are assumed to be normal. This is a fundamental hypothesis, because without it the assumption on gaussianity of the coefficients  $\beta^i$  fails, making the inference weak.

If we make some Shapiro-Wilk tests on the residuals of our datasets to verify this assumption, we get low P-values. Thus we have to reject the null hypothesis of gaussianity.

In Fig. 1.10 we reported some examples for two subjects of our dataset from an in vivo experiment. The P-value from Shapiro-Wilk test on the residuals is plotted for each channel (channels are on  $x$ -axis). The red line stands at 0.05.

Then we look for an alternative analysis that relax these hypotheses. Our analysis grows from the same essential idea of NIRS-SPM: we try to detect activation through an inspection of the dependence between data and an ideal hemodynamic response to neural activation. However theoretical assumptions are different, as we'll see in the next chapters.

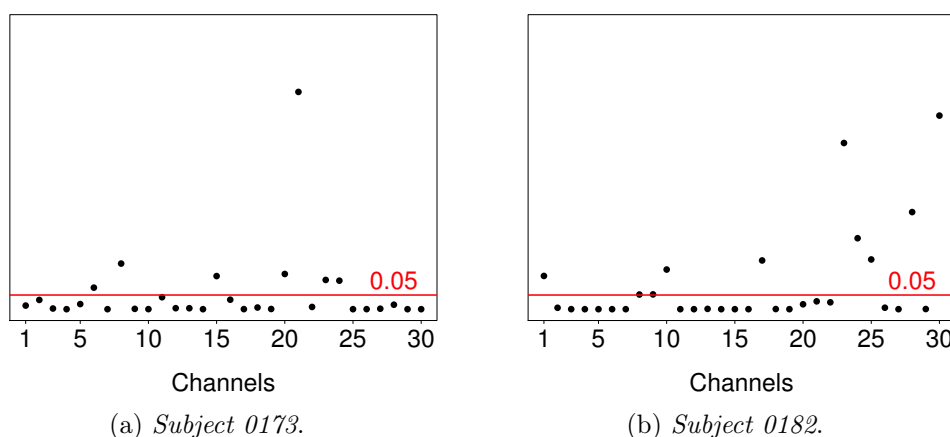


Figure 1.10: An example of P-values from Shapiro-Wilk tests on errors originated by the GLM. Data refer to  $O_2Hb$  of subjects 0173 and 0182.

# Chapter 2

## The datasets

We will use two types of data: in vivo data, originated by a real fNIRS experiment on volunteers, and synthetic data, obtained through simulations. Both in vivo and synthetic data present the same structure: they register (or mimic, if they are simulated) the concentration of O<sub>2</sub>Hb and HHb in 30 fixed positions (“channels”) of the brain in a healthy adult, during a motor task. The hemoglobin measurements are recorded with (or simulated as deriving from) a TD fNIRS system (for a definition of TD fNIRS, see Pag. 8).

The 30 channels are placed in the same positions in both synthetic and in vivo datasets. Their disposition on the head is reported in Fig. 1.1 at Pag. 6.

Hemoglobin concentrations of in vivo and virtual subjects are registered during a *right hand grip* experiment, in which periods of rest and task flow one after the other with the following structure: after an initial resting period

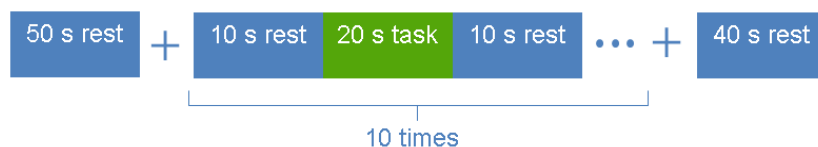


Figure 2.1: Temporal configuration of the right hand grip experiment.

of 50 s, 10 trials are performed. Each trial is composed by 10 s of rest, 20 s of right hand gripping (task) and 10 s of rest. A final resting period of 40 s is conducted after the last trial. The temporal configuration of the experiment is reported in Fig. 2.1. The experiment completely lasts 490 s.

The fNIRS system registers one concentration of O<sub>2</sub>Hb and one concentration of HHb on each second: a complete dataset is then composed by 30 vectors of length 490 for O<sub>2</sub>Hb measures, and 30 vectors of length 490 for HHb data.

In our work we consider each type of hemoglobin (oxygenated and deoxygenated) individually, analysing each of them in two different moments.

## 2.1 Pre-processing

A filtering algorithm is initially applied to all fNIRS datasets. The objective of the filter consists in subtracting some noise. In particular, we are interested in subtraction of habituation effects and high frequency noise.

We focus on the central 400 s of trials (10 s rest, 20 s task, 10 s rest), forgetting the first 50 and the last 40 s of rest. The sample mean on the first 10 s of each trial is subtracted to the related trial, in order to detrend data.

Then a smoothing spline algorithm is applied to the whole signal. If  $y_t$ , is hemoglobin concentration at time  $t = 1 : 400$ , the algorithm calculates the curve  $\hat{y}(t)$  that minimizes (in the class of twice differentiable functions) the following quantity:

$$\frac{1}{400} \sum_{t=1}^{400} (y_t - \hat{y}(t))^2 + \lambda \int_1^{400} (\hat{y}''(t))^2 dt. \quad (2.1)$$

The first term represents the estimated Mean Squared Error (MSE) when using  $\hat{y}(t)$  to estimate  $y_t$ . The second term penalizes the curvature of  $\hat{y}(t)$ . The parameter  $\lambda$  controls the trade-off between the accuracy of  $\hat{y}(t)$  (for  $\lambda = 0$  it corresponds to the original data) and how it is smoothed. Thus data are estimated through the smoothing spline  $\hat{y}(t)$  that minimizes a weighted sum of MSE and the average curvature.

In next sections we describe in vivo and synthetic data in details.

## 2.2 In vivo data

We have O<sub>2</sub>Hb and HHb measures from 12 right-handed healthy volunteers. Data were acquired by a multi-channel dual-wavelength TD fNIRS medical



device developed by the Physics Department of the Politecnico of Milan (see Contini et al., 2009).

Subjects are 7 males and 5 females, of age  $32.2 \pm 10$  years.

During task periods they squeezed a soft ball in the right hand at a rate of 2 Hz, guided by a metronome. Instructions about the movement and rest periods were given by presenting a picture on a screen, which always had a fixation cross in the centre.

Hemodynamic parameters were estimated by the Physics Department of the Politecnico of Milan through the following steps:

1. calculating the baseline optical properties and the absorption changes in the upper and lower layer;
2. gathering the hemoglobin concentrations from the absorption coefficients.

For each subject we have two datasets originated from the same physical experiment, from the same fNIRS system acquisition: the difference between them consists in the way in which raw data are treated by physicists' team after the fNIRS system registration. In particular, the difference concerns the estimation of the photon path length in the superficial and deep layers: we have different datasets depending on the used estimation method.

The simplest way to estimate the photon path length  $l$  consists in using the formula  $l = vt$ , where  $v$  is the speed of light in tissues and  $t$  is a characteristic time, set to  $500 \cdot 10^{-12}$  s for “early” photons (the ones that pass through superficial layers), set to  $1500 \cdot 10^{-12}$  s for photons from deep layers (they are called “late” photons). The risk of this method consists in overestimating the path in deep regions and underestimating hemoglobin concentration. The in vivo dataset obtained through this calculation will be identified as “INV1”.

A more complex estimation method was developed by the Physics Department of the Politecnico of Milan (for details, see Zucchelli et al., 2013). In this work the photon propagation model is refined through a more precise computation of the path length travelled by photons within each layer the tissue is composed of. The non-idealities of the fNIRS system set-up and the heterogeneous structure of the human head are also considered. This method leads to a reduction of photon path in deep regions, and to an increase in

estimated hemoglobin concentration. In this way we find higher hemoglobin amplitudes (until 10 times respect of the first dataset) and a more precise hemoglobin estimation. The signals are more corrupted by noise, though, because this method is more sensitive to few photons. In order to reduce noise we smooth data, applying a moving average of 5 s. We will refer to the dataset obtained through this method as to “INV2”.

At first we had only INV1, therefore all the analysis were initially developed and applied on this dataset.

Then, when the Physics Department provided INV2, we replayed only the most incisive and convincing methods on new data, abandoning techniques that had shown low performances on INV1.

An example of data from INV1 and INV2 is reported in Fig. 2.2. Here we can notice the different amplitudes of the signals.

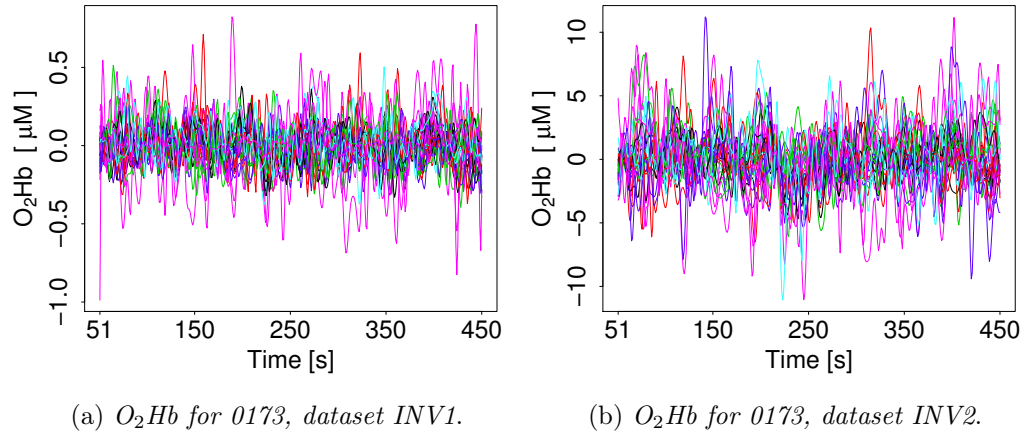


Figure 2.2: An example of in vivo data, from datasets INV1 and INV2. Data are reported during the ten trials (thus from second 51 to 450).

All the statistical analysis will be conducted separately and independently on each subject, except for group analysis in Section 4.5. Subjects are identified through a number: they are 0173, 0176, 0179, 0182, 0185, 0188, 0191, 0197, 0200, 0203, 0206, 0209.

Some subjects present several channels with very high noise. We will see that noisy channels can create many problems in activation detection. For

a visual identification of critical subjects in INV2 we can look at Fig. 2.3, 2.4, 2.5. In these figures we report for each channel the mean of hemoglobin concentration on trials of 40 s. O<sub>2</sub>Hb measures are in red, HHb measures are in blue.

During the 40 s trials, activated channels should have an increase in O<sub>2</sub>Hb and a decrease in HHb, drawing the shape of an eye. From these figures we have a visual control of noisy channels: subjects 0185, 0188, 0197, 0200, 0209 seem to have several noisy channels.

In the following sections we will specify at each time which in vivo dataset we will use (INV1 or INV2), and the reason of the choice (that typically depends on time in which the analysis was conducted).

A comparison between results on the two datasets can be in some cases useful to understand differences between data, and to direct the future analysis and path length estimation research.

## 2.3 Synthetic data

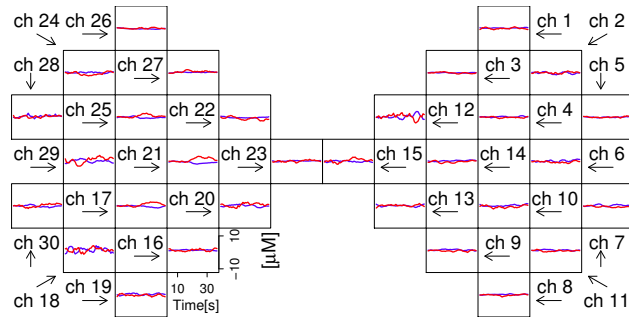
Simulated data mimic real multichannel fNIRS measurements on a healthy adult during the *right hand grip* experiment before described. The procedure to create synthetic data is developed by Physics Department of Politecnico of Milan. It consists in the following steps.

### Defining the geometry of the head

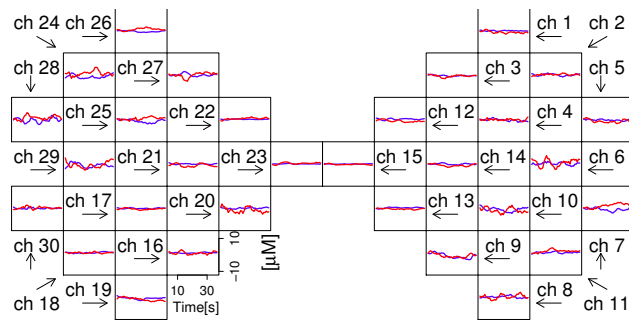
The head is modelled as a bilayered medium, where the upper layer is 1 cm thick, and the lower layer is ideally a semi-infinite medium. To a first approximation in fact this geometry can be used to simulate fNIRS measurements on the head of an adult, where an extra-cerebral layer (composed by scalp, skull and cerebrospinal fluid) overlays the intra-cerebral one (grey and white matter).

### Specification of the hemodynamic parameters and the HRF

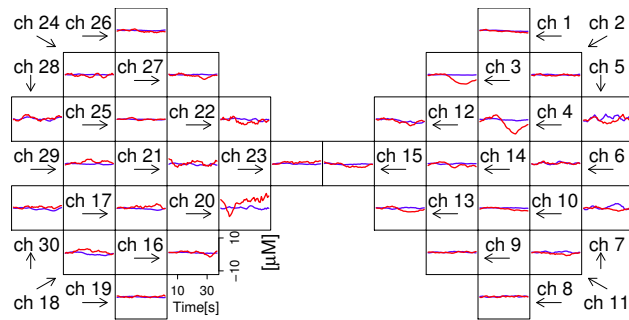
Hemoglobin concentrations are calculated for both layers of the head. They are simulated by considering reference values of 12  $\mu\text{M}$  for the O<sub>2</sub>Hb and 7  $\mu\text{M}$  for the HHb in the superficial layer, and reference values of 30  $\mu\text{M}$  for



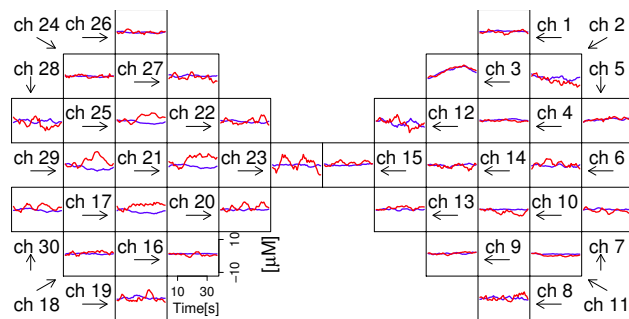
(a) Subject 0173.



(b) Subject 0176.

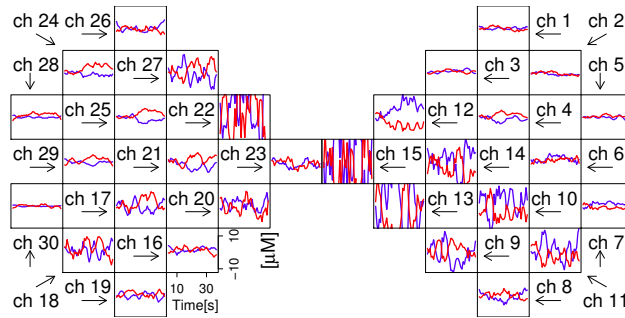


(c) Subject 0179.

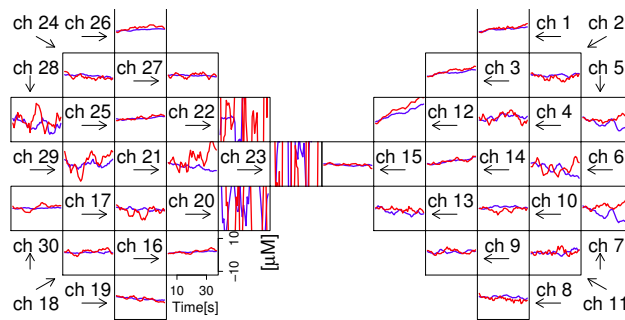


(d) Subject 0182.

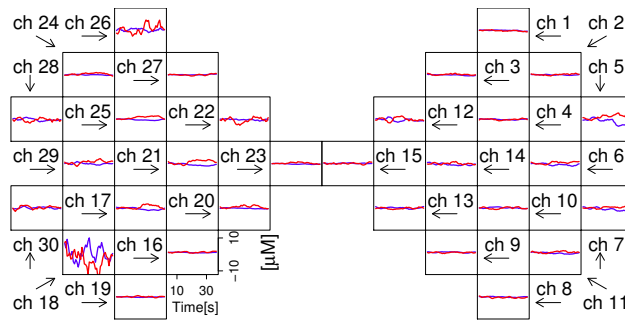
Figure 2.3: Means of  $O_2Hb$  and  $HHb$  concentration during trials for in vivo data (INV2).  $O_2Hb$  is in red,  $HHb$  is in blue.



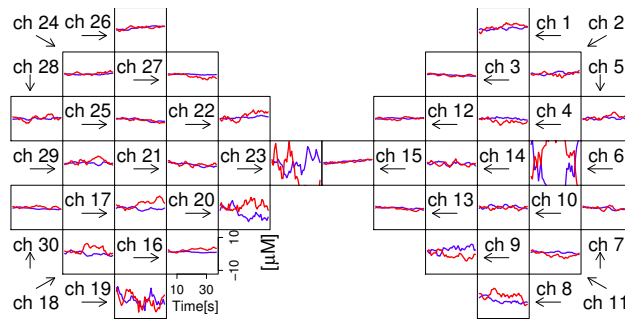
(a) Subject 0185.



(b) Subject 0188.

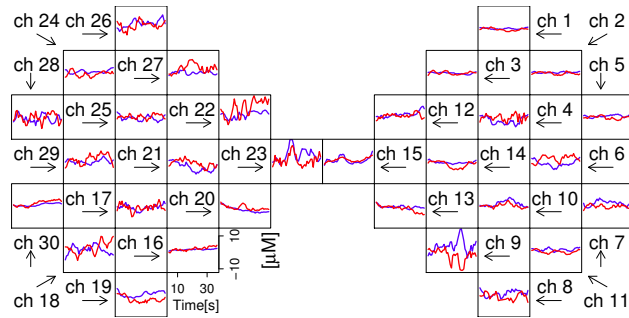


(c) Subject 0191.

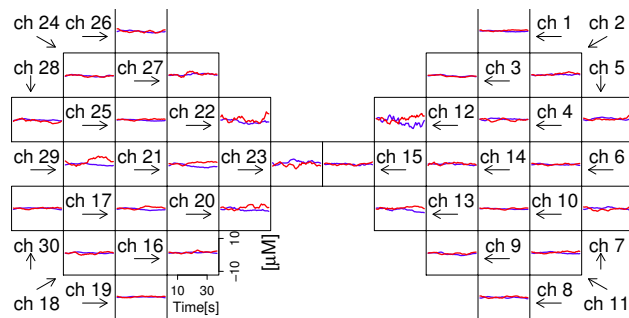


(d) Subject 0197.

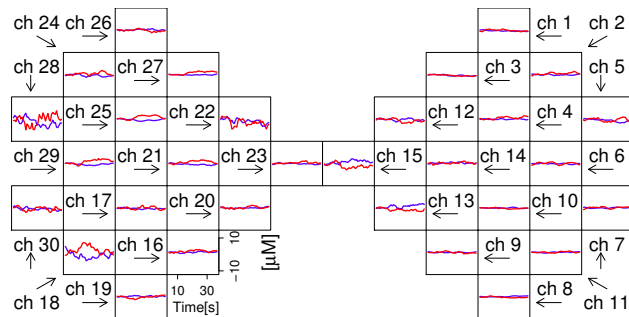
Figure 2.4: Means of  $O_2Hb$  and  $HHb$  concentration during trials for in vivo data (INV2).  $O_2Hb$  is in red,  $HHb$  is in blue.



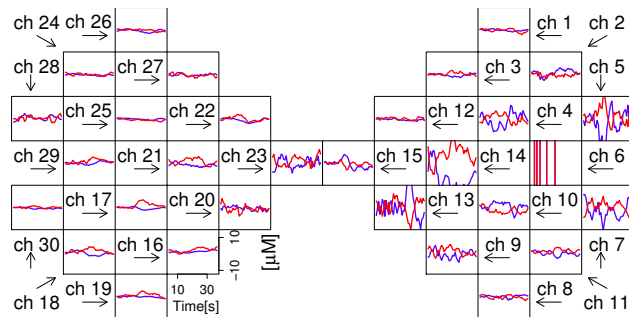
(a) Subject 0200.



(b) Subject 0203.



(c) Subject 0206.



(d) Subject 0209.

Figure 2.5: Means of  $O_2Hb$  and  $HHb$  concentration during trials for in vivo data (INV2).  $O_2Hb$  is in red,  $HHb$  is in blue.

the O<sub>2</sub>Hb and 20  $\mu\text{M}$  for the HHb in the lower layer.

Two different datasets are simulated.

The first experiment (EXP1) considers an ideal situation where a neuronal activation is generated by a motor task, and no physiological oscillations occur in the superficial layer. The O<sub>2</sub>Hb and HHb concentrations in the upper layer are simulated to be constant at reference values during the whole experiment, while the concentrations in the lower layer are perturbed in some channels so as to mimic a hemodynamic response in correspondence to the task periods.

This superimposed response profile is calculated as a convolution of a boxcar function, representing the task and rest alternation, with the Hemodynamic Response Function (HRF) evoked by a single stimulus. By following the method proposed by Scarpa et al. (2013) the HRF is modelled as a linear combination of two different gamma-variant time-dependent functions  $\Gamma_n$ :

$$\text{HRF}(t) = \alpha \cdot (\Gamma_n(t, \tau_1, \rho_1) + \beta \cdot \Gamma_n(t, \tau_2, \rho_2)), \quad (2.2)$$

with

$$\Gamma_n(t, \tau_j, \rho_j) = \frac{1}{p! \tau_j} \left( \frac{t - \rho_j}{\tau_j} \right)^p e^{-\frac{t - \rho_j}{\tau_j}} \delta(t - \rho_j),$$

$$\delta(t - \rho_j) = \begin{cases} 1 & \text{if } t - \rho_j \geq 0 \\ 0 & \text{otherwise} \end{cases}, \quad (2.3)$$

where  $\alpha$  tunes the amplitude,  $\tau_j$  and  $\rho_j$  tune the response width and the onset time respectively. Variability in amplitude of about 5% is considered among the different trials to account for possible differences in the execution of the task and/or in the functional response (e.g. habituation effects).

The peak of the HRF for the O<sub>2</sub>Hb is chosen to be around  $1.555 \pm 0.075$   $\mu\text{M}$ ; the HRF for the HHb is inverted and with a maximum set at  $-1/3$  with respect to the O<sub>2</sub>Hb response. The free parameters are chosen so as to create a HRF similar to the one expected for the motor task of interest ( $\alpha = 1282$ ,  $\beta = 0.17$ ,  $\tau_1 = 1$ ,  $\tau_2 = 1$ ,  $\rho_1 = -0.5$ ,  $\rho_2 = 3.5$ ).

To simulate an actual neuronal activation localized around the central positions of the hemisphere contralateral to the movement, channels considered as activated are: channel number 16 (with an intensity of 25% HRF), 17 (100% HRF), 18 (50% HRF), 21 (50%HRF), 28 (25% HRF), 29 (50% HRF).

Table 2.1: Mean and standard deviation of frequency and amplitude of each physiological component (Scarpa et al., 2013).

	Frequency (Hz)	Amplitude (nM)
Very low frequency	$f_1 = 0.002 \pm 0.0001$	$A_1 = 700 \pm 100$
Low frequency	$f_2 = 0.01 \pm 0.001$	$A_2 = 700 \pm 100$
Vasomotor	$f_3 = 0.07 \pm 0.04$	$A_3 = 400 \pm 10$
Respiratory	$f_4 = 0.2 \pm 0.03$	$A_4 = 200 \pm 10$
Cardiac	$f_5 = 1.1 \pm 0.1$	$A_5 = 400 \pm 10$

In the other channels no hemodynamic response is added.

In the second experiment (EXP2) the reference values for both layers and for the hemodynamic changes happening in the lower layer are identical to EXP1. However a physiological noise is added in the superficial layer by following the procedure reported by Scarpa et al. (2013).

The physiological noise at time  $t$ , indicated as  $\psi(t)$ , is an oscillation built for O<sub>2</sub>Hb signal for one channel as a sum of sinusoidal functions at different mean frequencies and amplitudes:

$$\psi(t) = \sum_{i=1}^5 A_i \sin(2\pi f_i t + \phi_i).$$

Amplitudes  $A_i$  and frequencies  $f_i$  vary in the channel for every repetition in the range described in Table 2.1, while phases  $\phi_i$  are equally distributed between 0 and  $2\pi$  and are different for each trial. The generated signal is then replicated for all the channels by modifying the oscillation amplitude of a random value between  $\pm 10\%$ .

The HHb variations are generated by threefold reducing the magnitude of the physiological noise simulated for the O<sub>2</sub>Hb.

### Obtaining the absorption coefficients

The absorption coefficients at two wavelengths (690 and 820 nm) for both layers are computed from these hemoglobin concentration changes by exploiting



the Lambert Beer law (see (1.2)) and the a priori knowledge of the specific absorption of O<sub>2</sub>Hb and HHb.

#### **Adding the information on the reduced scattering coefficients**

The scattering coefficients at the same wavelengths are derived from a simple approximation of the Mie theory:

$$\mu'_s(\lambda) = a \left( \frac{\lambda}{\lambda_0} \right)^{-b} \quad (2.4)$$

by setting the amplitude scattering  $a$  and the power scattering  $b$  fixed respectively at  $12 \text{ cm}^{-1}$  and  $0.5$  for the upper layer, and at  $12 \text{ cm}^{-1}$  and  $1$  for the lower layer, for a reference  $\lambda_0$  at  $660 \text{ nm}$ .

#### **Generate distributions of photon time-of-flight**

A forward model for photon diffusion in a bilayered geometry is used to generate synthetic time-resolved reflectance curves for each channel by using as input parameters the optical properties and the source detector distance (fixed at  $3 \text{ cm}$ ). A count rate of  $5 \cdot 10^5 \text{ ph/s}$  is considered, the integration time is set at  $1 \text{ s}$ , and Poisson noise is added to the simulated curves to mimic real measurements.

After this procedure, hemodynamic parameters are obtained as for in vivo data, estimating the baseline optical properties and the absorption changes in the upper and deep layer and calculating the hemodynamic parameters from the absorption coefficients, following the method proposed by Zucchelli et al. (2013).

Finally, data are pre-processed through the algorithm of Section 2.1.

The resulting hemoglobin concentrations for synthetic datasets are reported in Fig. 2.6.

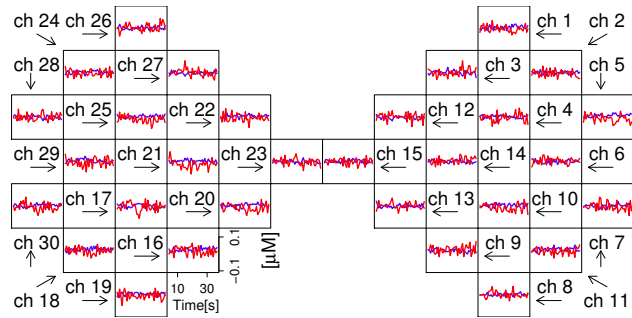
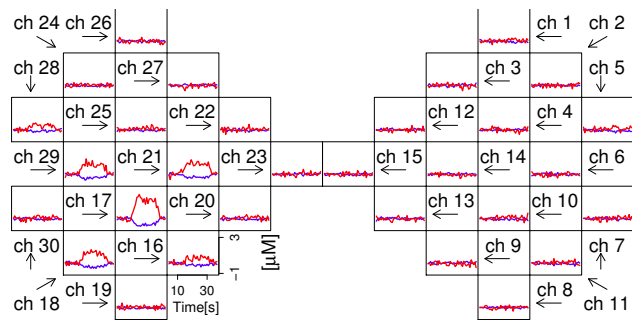
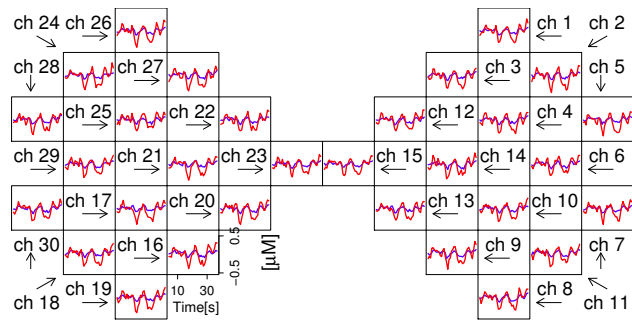
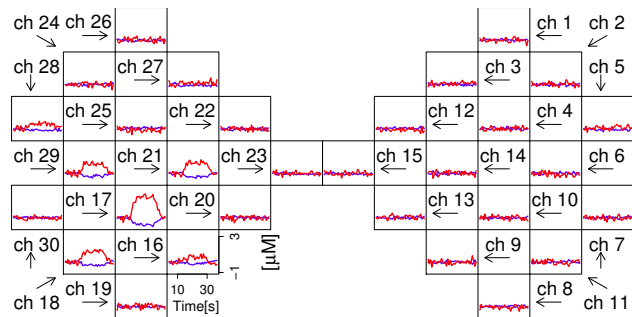
(a) *Folded data for the superficial layer of EXP1.*(b) *Folded data for the deep layer of EXP1.*(c) *Folded data for the superficial layer of EXP2.*(d) *Folded data for the deep layer of EXP2.*

Figure 2.6: Means of  $O_2Hb$  and  $HHb$  concentration during trials for synthetic data EXP1 and EXP2.  $O_2Hb$  is in red,  $HHb$  is in blue.

# Chapter 3

## AUC Analysis

In this section we study the “area under the curve” (AUC) of hemoglobyn concentrations. To do this we look at our data as a functional data. This approach is different from the one used in the other chapters, where we always consider the data as vectorial data.

We propose two AUC analysis. They were conducted in two different moments, with different purposes. The former analysis aims at channel activation detection. One of the critic points in analysing fNIRS data is their high dimensionality compared with their low sample size: the information on activation is split on 400 measures for each channel, and the number of channels, usually equivalent to the sample size, is equal to 30. The first attempt in detecting activation was then dimensionality reduction. We were looking for some indices that could summarize the information on activation, making data easy to handle. AUC was the first index we thought. It is an index simple to calculate with a clear meaning.

The latter analysis aims at “anomalous channels” detection. This expression refers to signals with too high noise, and for this reason they can’t be used for activation analysis. This is mainly due to a low number of registered photons. We will see that AUC analysis will help us in detecting these abnormal measures.

### 3.1 AUC analysis for activation detection

One of the first attempt in detecting cortical activation was “area under the curve” (AUC) analysis. We knew that the ideal hemodynamic response has a known shape, shown by the Hemodynamic Response Function (HRF), and it has a positive AUC for O<sub>2</sub>Hb. We wondered if activated channels had specific AUC, maybe higher than not-activated ones, and if they could be detected through it. We thought that activated channels could have higher AUC because we supposed that noise on not-activated signals, that mainly causes not null AUC, had lower amplitude than the hemodynamic response. In this chapter we analyse the in vivo dataset INV1, using O<sub>2</sub>Hb concentrations because of the highest amplitude of the signal.

After the preprocessing algorithm we split the signal in ten sub-intervals of 40 s for each channel, evaluating the absolute value of AUCs for each sub-interval. We choose to use the absolute value because HRF is positive in the first seconds, then it becomes negative. Choosing AUC with sign we could find small AUC also for activated channels because of compensation between positive and negative areas.

We build a boxplot of AUC in different channels for each sub-interval, in order to verify if AUCs change with sub-intervals. We report boxplots for 0173 and 0203 in Figure 3.1a e 3.1b, as an example (boxplots from other subjects have the same features). Boxplots look like very homogeneous and similar to each other. This means that sub-intervals don’t help us in discriminating AUC. To confirm this we implement an ANOVA model with sub-intervals as group factors. As we expected from boxplot visual inspection, we don’t reject the null hypothesis of equality of the means.

This is coherent with the hypothesis we will make in the next sections, in which we will consider each sub-interval as a realization of the same event.

Obviously in this figure we can’t find any information about the relation between AUC and activated channels.

To inspect activation we plotted boxplots for AUC divided by channels. Graphics referred to O<sub>2</sub>Hb for subjects 0173 and 0203 are reported in Figure 3.1c and 3.1e. Looking at these images we can understand that it is difficult to detect activation trough AUC.

Differently from previous image, boxplots are not similar to each other. Some of them have a higher mean and a larger variance (in particular, the ones related to ch. 12, 18, 20, 28, 29 for subject 0173, to ch. 12, 22, 23 for subject 0203). This means that AUC differs from channel to channel and there are channels with higher AUCs, as we expected. Unfortunately, though, channels with different boxplot are not the activated ones, as we can see from activation brain maps on the right, in which activated channels are in white. Almost all the activated channels in the maps (such as ch. 17, 21, 25 for subject 0173, ch. 17, 20, 21, 29 for 0203) have related boxplots that don't have higher sample mean or variance. If we implement for subject 0173 an ANOVA model, using as group factors channels 17, 21, 25, 29 (the activated ones, according to the activation map on the right), we find a high P-value. We can't then reject the null hypothesis of equality of the means.

We also applied a k-means algorithm on the  $\mathbb{R}^2$  vectors made for each channel by its AUC sample mean and its AUC standard deviation, in order to see if this classification algorithm can discriminate between activated/not-activated channels. As we expected from the previous analysis, it failed.

Thus we hypothesize that differences among boxplots are generated by other factors, and that it is not possible to perform an activation detection using AUC only. We then move to an analysis that consider the shape of the signal, not only the area under it (coherently with the state of the art). Oscillations caused by noise in not-activated channels probably are too high, and they produce AUC similar to the ones of activated signals, making impossible activation detection.

Trough this analysis we can also realize that abnormal boxplots can derive from anomalies on data. Thus, when we were asked about outlier detection and anomalous data analysis, we thought about AUC.

## 3.2 AUC analysis for anomalous channels detection

Another problem we faced is anomalous channel detection. NIRS data usually present some channels with a very high noise, mainly due to a low number of

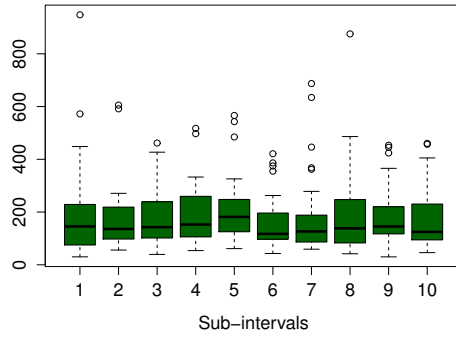
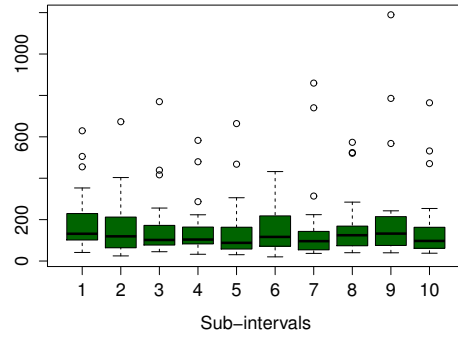
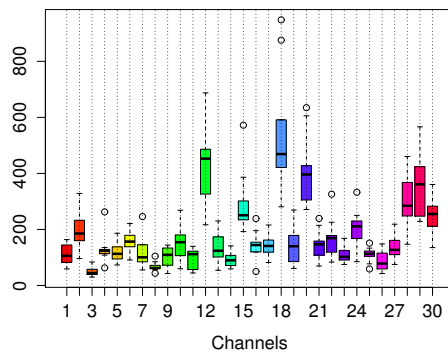
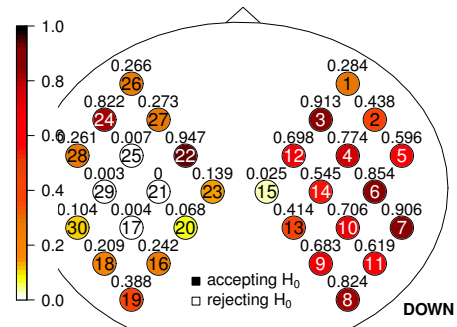
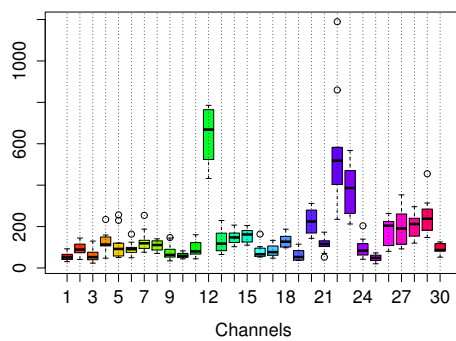
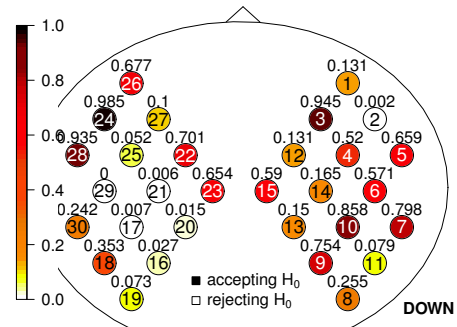
(a) *AUC in trials, subject 0173.*(b) *AUC in trials, subject 0203.*(c) *AUC boxplot in channels, subj. 0173.*(d) *Activation map for subject 0173.*(e) *AUC boxplot in channels, subj. 0203.*(f) *Activation map for subject 0203.*

Figure 3.1: Boxplots on AUC, divided by channels and by trials. In the activation maps, colours indicate the activation degree of each channel: activated channels are in white.

registered photons.

This can happen for many reasons: hair covering the sensors, particular head shape, equalization of signals that produces a penalization of some channels not to saturate others with too many photons.

An anomalous signal can derive also from the reception of external light or from a loss of contact between the skin and the optode (due, for example, to motion artefact). This can last for a part or the whole experiment, thus we can have channels with a signal that is always out of control, or channels with acceptable hemoglobin concentrations till a certain moment, and then a degeneration with a change of some orders of magnitude. Some of these anomalous data are easy to find even through a visual inspection (see, for an example of clear anomalies, Figure 3.2); others are more difficult to detect.

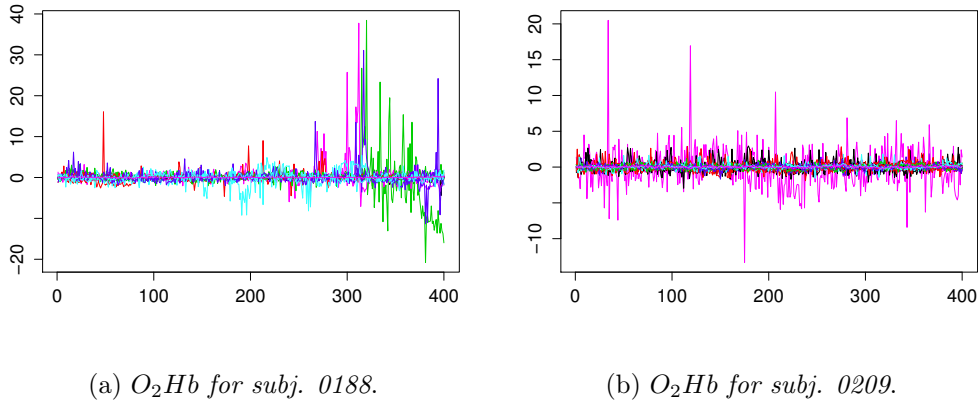


Figure 3.2: Clear examples of anomalous channels.

It would be preferable to exclude abnormal channels from activation analysis: an appropriate outlier detection should be performed before using any activation detection algorithm. If the algorithm analyses channels independently one to each other, this can be done not to find false activated channels, or not to catch information from an unreliable data. If activation analysis is not on individual channels but it requires interaction among them, then an outlier detection is even mandatory not to alter results. This happens, for example, using k-means algorithm, as in Section 4.4: we will see that in this

Table 3.1: Abnormal channels from a visual inspection.

Subject	Excluded channels
0173	12, 18
0176	6 8, 20, 24, 28, 29
0179	20, 21
0182	8, 12, 19
0185	8, 9, 10, 11, 12, 13, 14, 15, 17, 18, 20, 22, 27
0188	4, 6, 7, 20, 21, 22, 23, 28, 29
0191	18, 22, 26
0197	6, 8, 9, 18, 19, 20, 23, 29
0200	4, 8, 9, 12, 17, 22, 23, 25, 26, 28, 29
0203	12
0206	18, 20, 22, 28
0209	2, 4, 5, 6, 7, 9, 10, 12, 13, 14, 15, 20, 23

situation the exclusion of irregular channels is required to obtain acceptable results.

We have a list, made by experts, with channels which seem to be abnormal from a visual inspection. They are reported in Tab. 3.1.

The question is: is it possible to detect anomalous channels through some automatic algorithm? We think again at the AUC analysis of Section 3.1, looking at boxplots in Fig. 3.1. We wonder if channels with particular boxplots are generated by anomalous signals. By intuition it can be correct that anomalous signals have a high AUC mean, due to measures from a different order of magnitude, and/or a high AUC variance (this happens when a signal is correct till a certain moment and then it degenerates, producing AUC very different from the previous ones). If this hypothesis was correct we could detect outliers through an analysis on the sample mean and the sample variance of AUC.

For an outlier detection we use O<sub>2</sub>Hb concentrations, pre-processing data subtracting the baseline sample mean for each trial (without applying spline interpolation). As in the previous section we calculate the AUC for each



sub-interval of the absolute value of the signal. Then we build a bivariate dataset with sample size  $n = 30$ , made by the AUC sample mean and the AUC sample variance in each channel.

One idea is to compute Tukey depth. It is a measure proposed by John Tukey in ‘70 for outlier detection and estimation of the “centre” of multivariate data. For each point of a bivariate dataset it evaluates all possible half spaces generated by a line passing through the point, counting for each half space the minimum number of points at one side. Then the Tukey depth of each statistical unit is the minimum number of sample points on one side of half spaces, divided by the sample size. This measure evaluates how much a point is extreme for the population. Outliers will have a low depth, while a good estimate of the population will have a high depth (it will be in the “centre” of the population). We calculate Tukey depth using the R package `depth`<sup>1</sup>.

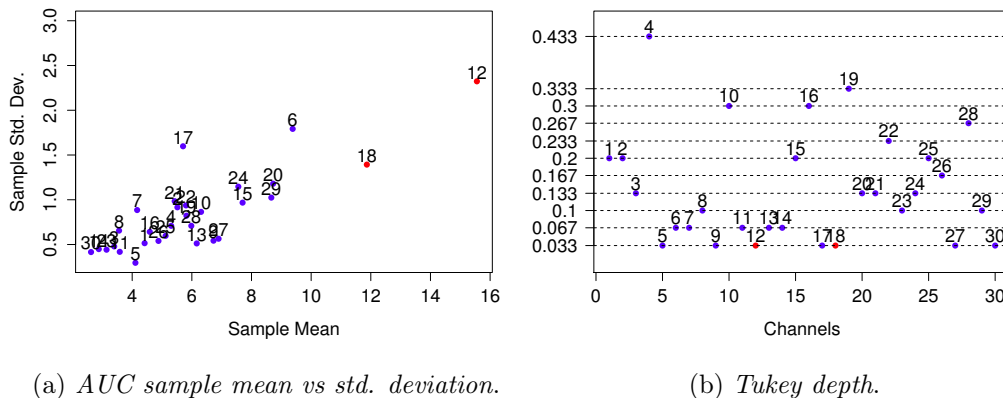


Figure 3.3: AUC sample mean vs standard deviation for subj. 0173, and related Tukey depth.

Nevertheless this measure is not very suitable for our aim. One of its drawbacks is that Tukey depth is radial symmetric: it considers as outliers all the points at the peripheral regions, independently of the part of the space in which the points are. This doesn’t work well with our purpose because we are interested in identifying channels with high sample mean and high

<sup>1</sup>Genest et al. (2012)

variance and, for example, we don't care about the points in the bottom of the cloud. An example of this bad behaviour is reported in Fig. 3.3. In this image the anomalous channels are represented by red points in the plane. If we look at 3.3b we can notice that the lowest depth (equal to 0.033, that is  $1/30$ ) is related to points higher than the cloud (ch. 12, 17, 18), but also to channels with low AUC sample mean and sample variance (ch. 5, 9, 27, 30).

Moreover if we analyse one subject at time Tukey depth labels as outliers the extreme points of the subject, obviously without considering the absolute magnitude of the points. This means that the algorithm always finds outliers: if a subject hasn't got any anomalous channel, the depth will be minimal for the points on the edge of the cloud, which will be labelled as outliers even if they are not.

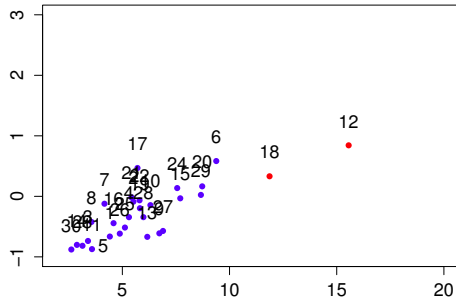
A more appropriate method should consider the absolute values of the sample mean and the sample variance, proposing a threshold beyond which the channels must be excluded.

In Fig. 3.4 and 3.5 we reported the natural logarithm of the AUC sample standard deviation (on  $y$ -coordinate) as a function of the AUC sample mean (on  $x$ -coordinate) for all the subjects. Anomalous channels from visual inspection are in red.

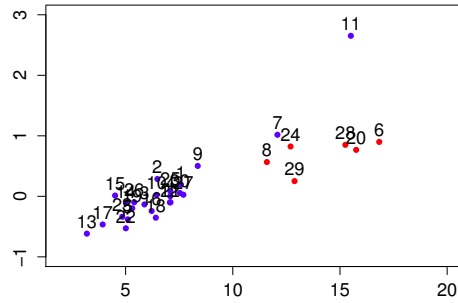
From this graphics we can observe that high sample mean and high variance seem to be correlated. This is confirmed by a linear regression model in which we use the sample standard deviation as the independent variable, and the sample mean as predictor. P-values associated to the tests on the predictor coefficient ( $H_0 : \beta = 0$  vs  $H_1 : \beta \neq 0$ ) are low for each subject, so the null hypothesis is rejected and the linear dependence is verified.

Then we can notice that red points are in the right part of each image, which means they have higher AUC sample mean. In all the subjects except the ones with a lot of abnormal channels (such as 0185, 0188, 0197, 0200 and 0209) red points are well separated from the point cloud. This suggests us that the idea of detecting abnormal channels trough AUC is good. We could fix a threshold between 10 or 12 for the AUC mean.

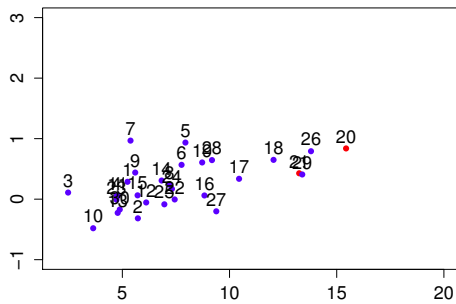
Thus if we have to detect anomalous channels we can look at AUC sample mean: if it is smaller than the threshold the channel will be used for the activation analysis, otherwise it will be excluded.



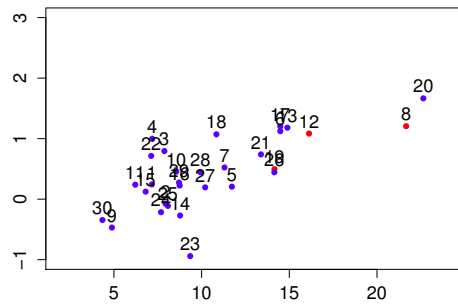
(a) Subject 0173.



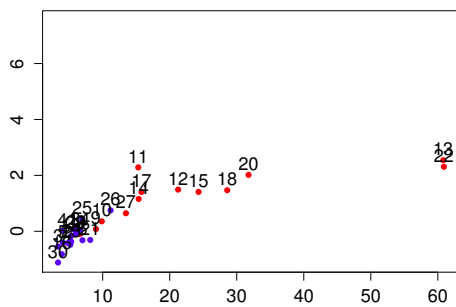
(b) Subject 0176.



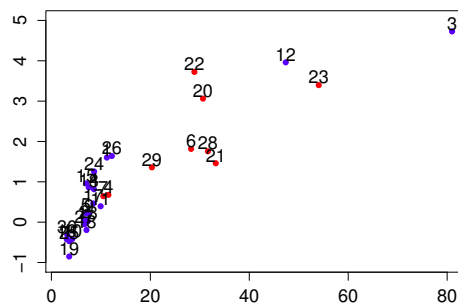
(c) Subject 0179.



(d) Subject 0182.



(e) Subject 0185.



(f) Subject 0188.

Figure 3.4: Sample Mean vs Log(Std. Dev.) for subjects 0173, 0176, 0179, 0182, 0185, 0188.

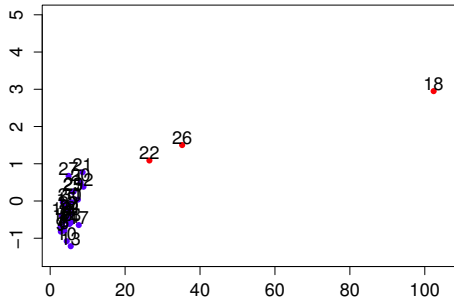
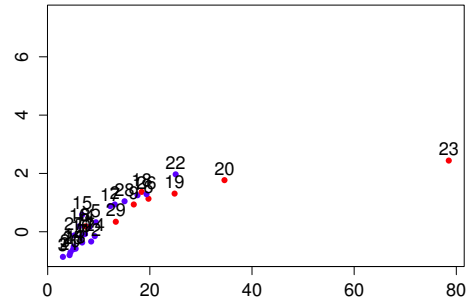
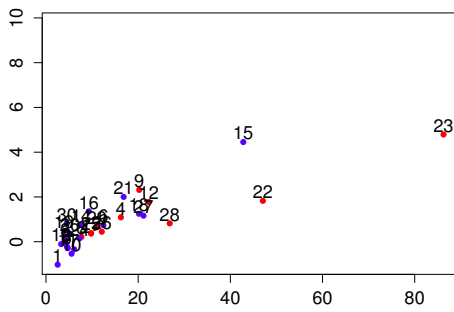
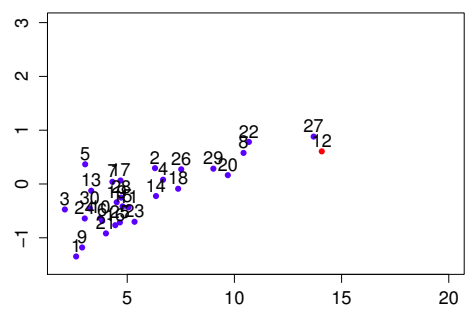
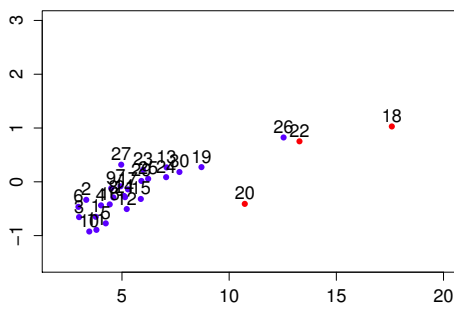
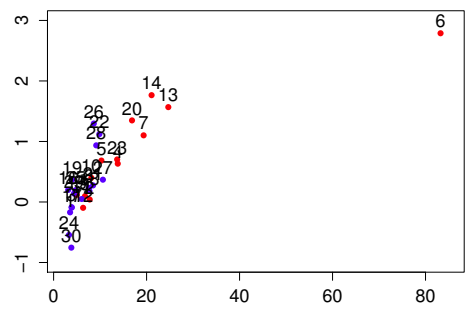
(a) *Subject 0191.*(b) *Subject 0197.*(c) *Subject 0200.*(d) *Subject 0203.*(e) *Subject 0206.*(f) *Subject 0209.*

Figure 3.5: Sample Mean vs Log(Std. Dev.) for subjects 0191, 0197, 0200, 0203, 0206, 0209.

# Chapter 4

## Activation detection through linear regression models

In this chapter we propose a procedure for channels' activation detection. We showed in Section 1.3 that a common approach to this problem doesn't include a check of important hypothesis on which the used statistical tests are based, such as the gaussianity of residuals. Furthermore, statistics used for inference are often obtained through approximations and rough assumptions (for an example, see the procedure to find a known distribution for the statistic  $T$ , in Section 1.3).

Therefore the main objective of this work consists in proposing a method for activation detection with higher solidity and theoretical rigour than existing ones. This will be performed maintaining the good-working aspects of the widely used models presented so far: in particular, the linear dependence of data from a reference signal (the HRF) will be inspected, as in the current literature.

### 4.1 The linear regression model

Each fNIRS dataset (in vivo and synthetic, for O<sub>2</sub>Hb and HHb, superficial and deep layers) is pre-processed (baseline sample mean subtraction and smoothing spline interpolation) as described in Section 2.1. Then each dataset is analysed through the following linear model, one at a time.

The first 50 s and the last 40 s of the experiment (resting periods) are neglected, in order to focus on the 400 s central part of the experiment, in which activation can be found.

Instead of using all the 400 s for a single linear regression model, we divide the data time series of each channel in 10 sub-intervals (i.e. repetitions or trials) lasting 40 s (made of 10 s rest, 20 s task, and 10 s rest).

We then individually apply a linear regression model to each sub-interval. Each trial is the elementary sequence revealing activation. It represents a repetition of the same event, a realization of the same phenomenon (the activation sequence). It can therefore be interesting to first analyse each trial independently, writing a regression model for each of them.

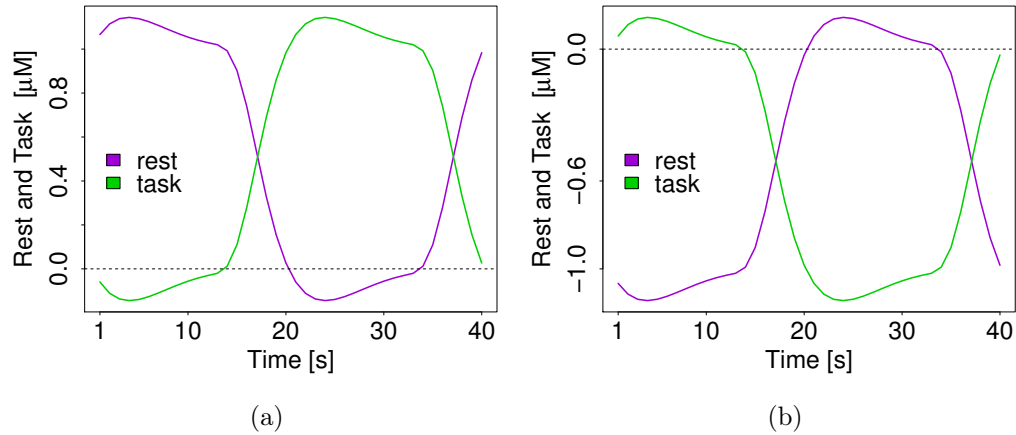


Figure 4.1: Regressors for  $O_2Hb$  (4.1a) and  $HHb$  (4.1b) concentrations.

If  $i$  indicates the sub-interval and  $k$  indicates the channel, we build for each channel  $k = 1 : 30$  the ten following linear regression models:

$$\mathbf{y}^{i,k} = X\boldsymbol{\beta}^k + \boldsymbol{\varepsilon}^{i,k}, \quad i = 1, 2, \dots, 10, \quad (4.1)$$

where  $\mathbf{y}^{i,k}$  is the vector of data,  $X$  is the design matrix,  $\boldsymbol{\beta}^k$  the vector of

coefficients,  $\epsilon^{i,k}$  a term of error. They are defined as follows:

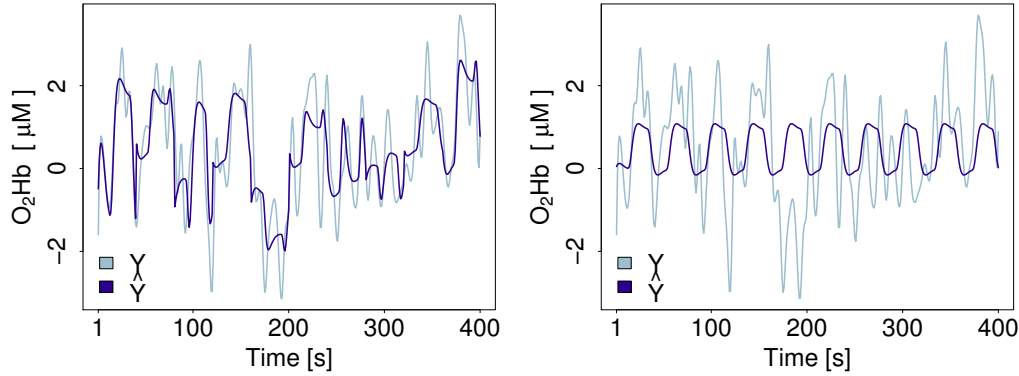
$$\mathbf{y}^{i,k} = \begin{pmatrix} y_1^{i,k} \\ y_2^{i,k} \\ \vdots \\ y_{40}^{i,k} \end{pmatrix}, \quad X = \begin{pmatrix} 1 & rest_1 & task_1 \\ 1 & rest_2 & task_2 \\ \vdots & \vdots & \vdots \\ 1 & rest_{40} & task_{40} \end{pmatrix}, \quad \boldsymbol{\beta}^k = \begin{pmatrix} \beta_0^k \\ \beta_{rest}^k \\ \beta_{task}^k \end{pmatrix}, \quad \boldsymbol{\epsilon}^{i,k} = \begin{pmatrix} \epsilon_1^{i,k} \\ \epsilon_2^{i,k} \\ \vdots \\ \epsilon_{40}^{i,k} \end{pmatrix}.$$

Under the hypothesis that O<sub>2</sub>Hb increases during the task periods, the regressors for O<sub>2</sub>Hb, *rest* and *task*, are obtained through a convolution between the HRF and a step-function (equal to 0 in the first and last 10 s and 1 elsewhere for *task*, the opposite for *rest*). They are shown in Fig. 4.1a.

On the contrary, given that HHb is expected to decrease during the task, the regressors for HHb are built as a convolution between the HRF and a step-function equal to 0 in the first and last 10 s, -1 elsewhere for *task*, the opposite for *rest* (see Fig. 4.1b).

For each channel  $k$  and sub-interval  $i$ , we calculate the Ordinary Least Squares estimators for  $\boldsymbol{\beta}^k$ , as:

$$\hat{\boldsymbol{\beta}}^{i,k} = (X^T X)^{-1} X^T \mathbf{y}^{i,k}.$$



(a) Ten regression models on ten trials.

(b) A unique regr. model on all 400 s.

Figure 4.2: Comparison between fitted data in the two approaches. Images refer to channel 25 of O<sub>2</sub>Hb (INV2). Real data are in grey, fitted data are in blue.

Following this procedure we obtain fitted values  $\hat{\mathbf{y}}^{i,k}$  more similar to  $\mathbf{y}^{i,k}$  than the ones found through a single linear regression model. An example is

reported in Fig. 4.2, where fitted values and real data for channel 25 of in vivo subject 0173 are plotted for ten regression models on sub-intervals (Fig. 4.2a) and for a unique regression model on all 400 s (Fig. 4.2b). Real data are in grey, fitted data are in blue. The figure refers to O<sub>2</sub>Hb of dataset INV2. In the first situation the Mean Square Error (MSE) is lower than in the second one (precisely, 0.67 vs 1.59  $\mu\text{M}^2$ ), in which the obtained coefficients are the same for all trials, preventing any variability.

For this reason the approach with regression models on trials well suits also experiments where the intensity of the HRF varies in time.

Moreover, through this approach, we have a sample of size 10 from the population of  $\beta_{rest}^k$ ,  $\beta_{task}^k$  and  $\beta_{task}^k - \beta_{rest}^k$  for each channel  $k$ . These quantities summarize appropriately the information about activation in each sub-interval: the following step will be analysing them in depth, understanding if and how they can be used to distinguish between activated and not-activated channels.

## 4.2 Analysis of the coefficients of the models

We report here some analysis on the quantities having a role in the regression models, such as residuals  $\epsilon$ , the coefficients' estimates  $\beta_{rest}^k$  and  $\beta_{task}^k$ , and data  $\mathbf{y}$ , in order to better understand the features of our samples.

Some of these analysis will be used for the final output of our research, others are just preliminary and can be omitted in analysing future datasets.

They are performed on INV1.

### Gaussianity of data and residuals

Introductory analysis on gaussianity of data is performed trough Shapiro-Wilk tests. For each trial and channel a test is implemented on O<sub>2</sub>Hb and HHb measures. P-values vary from subject to subject. Generally 46% of them is higher than 0.05, thus it is not possible to accept the hypothesis of gaussianity of O<sub>2</sub>Hb and HHb.

Gaussianity of residuals is tested in the same way. P-values from Shapiro-Wilk tests are higher than 0.05 in 62% of trials. Also in this situation we can't assume gaussianity of residuals.



These analysis are quite simple and rough (no correction on P-values is performed), but they show that gaussianity of data and residuals is a delicate point, and that it is preferable not to use inference tests based on these assumptions of normality.

## Gaussianity of coefficients estimates

The gaussianity of  $\hat{\beta}_{rest}^{i,k}$  and  $\hat{\beta}_{task}^{i,k}$  is investigated, as well as the gaussianity of the linear combination  $\hat{\beta}_{task}^{i,k} - \hat{\beta}_{rest}^{i,k}$ , through running, on each channel  $k$ , three Shapiro-Wilk tests (one on the ten-observations sample  $(\hat{\beta}_{rest}^{1,k}, \hat{\beta}_{rest}^{2,k}, \dots, \hat{\beta}_{rest}^{10,k})$ , one on  $(\hat{\beta}_{task}^{1,k}, \hat{\beta}_{task}^{2,k}, \dots, \hat{\beta}_{task}^{10,k})$ , one on their linear combination).

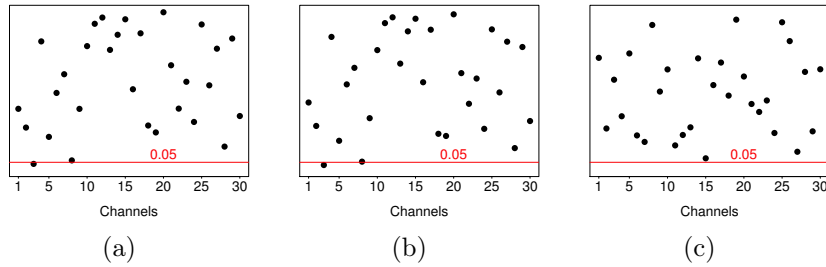


Figure 4.3: Gaussianity P-values for  $\hat{\beta}_{rest}^{i,k}$  (4.3a),  $\hat{\beta}_{task}^{i,k}$  (4.3b) and  $\hat{\beta}_{task}^{i,k} - \hat{\beta}_{rest}^{i,k}$  (4.3c) for the deeper layer of INV1, O<sub>2</sub>Hb.

P-values are almost always higher than 0.05 in every dataset, both simulated and in vivo, with O<sub>2</sub>Hb and HHb measures. An example is reported in Fig. 4.3. We can therefore assume that, for each fixed channel  $k$ ,  $\hat{\beta}_{rest}^{i,k}$  belongs to a normal distribution, as well as  $\hat{\beta}_{task}^{i,k}$  and  $\hat{\beta}_{task}^{i,k} - \hat{\beta}_{rest}^{i,k}$ .

In order to discriminate between activated/not-activated channels we focus on the contrast of the coefficients,  $\hat{\beta}_{task}^{i,k} - \hat{\beta}_{rest}^{i,k}$ , coherently with the current literature (see Friston et al., 2011).

## Tests between right and left hemispheres

Activation is expected in the left hemisphere, in some a priori unknown channels. A first idea can be to compare contrasts of the two hemispheres, to see if there are differences between them. Boxplots of each hemisphere

for all subjects are reported in Fig. 4.4 for a visual comparison. We can notice that boxplots from the left hemispheres are generally higher than the ones referred to the relative right hemisphere. This can happen because of

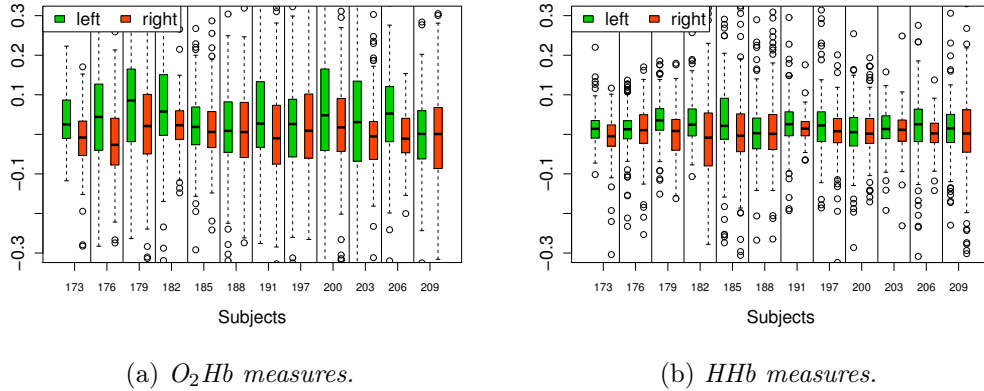


Figure 4.4: Boxplots of contrasts in right and left hemispheres, for each subject.

activated channels, that are supposed to have contrasts higher than zero. For most of subjects variance seems different in the two hemispheres: left hemispheres could have higher variability because of the presence of channels with very different degrees of activation.

If we look at boxplots related to HHb measures, we see that they are smaller: as we know, the amplitude of HHb signals is lower than  $O_2Hb$ . This affects also the coefficients' estimates.

In order to confirm these hypothesis, we implement for each subject a statistical test of comparison between the variance of the two groups, and a test of comparison between the means.

Statistics for tests on the variances of two hemispheres are calculated as the ratio between the sample variances of the two groups. If the null hypothesis of equal variances is true, the statistic follows a Fisher distribution, with (149, 149) degrees of freedom.

For tests on the means, we calculate the following statistic

$$T = \frac{\bar{X}_{left} - \bar{X}_{right}}{\sqrt{\frac{S_{left}^2 + S_{right}^2}{150}}},$$

Table 4.1: Tests comparing variances and means of contrasts in right and left hemispheres.

	O <sub>2</sub> Hb		HHb	
	Test on variances	Test on means	Test on variances	Test on means
173	0.36	10 <sup>-7</sup>	0.001	8 · 10 <sup>-5</sup>
176	6 · 10 <sup>-4</sup>	10 <sup>-6</sup>	2 · 10 <sup>-5</sup>	0.372
179	50.21	9 · 10 <sup>-5</sup>	0.01	5 · 10 <sup>-6</sup>
182	0	9 · 10 <sup>-4</sup>	0	2 · 10 <sup>-4</sup>
185	0.25	0.226	3 · 10 <sup>-4</sup>	0.043
188	5 · 10 <sup>-4</sup>	0.712	0.01	0.644
191	0.002	0.019	0	0.128
197	0	0.432	6 · 10 <sup>-12</sup>	0.210
200	0	0.095	0	0.057
203	0	0.029	0.002	0.193
206	5 · 10 <sup>-15</sup>	6 · 10 <sup>-7</sup>	0	0.026
209	0	0.181	0	0.067

where  $\bar{X}_{left}$  and  $\bar{X}_{right}$  are the contrasts sample means in the two hemispheres,  $S_{left}^2$  and  $S_{right}^2$  are the sample variances. If the null hypothesis of equal means is true, the statistic has a t-student distribution, with degrees of freedom dependent on variances in the two samples: if variances are equal, the degrees of freedom are 298; if variances are different, the degrees of freedom are approximated by:

$$\nu = \frac{149 \cdot \left( \frac{S_{left}^2 + S_{right}^2}{150} \right)^2}{\left( \frac{S_{left}^2}{150} \right)^2 + \left( \frac{S_{right}^2}{150} \right)^2}.$$

P-values are reported in Tab. 4.1.

We observe that results vary a lot. This happens because the clustering of the channels is rigid and made a priori. The hemisphere with activated channels (the left one) includes also not-activated areas, that reduce the difference between hemispheres. Thus when we ask if there is a difference

between the two groups of contrasts, the answer is often negative. We need a higher degree of precision in localizing activation: a comparison between hemispheres is not enough, a (binary or continuous) activation label is required for each channel.

## A test on each channel

We use the 10 found linear combinations  $\hat{\beta}_{task}^{i,k} - \hat{\beta}_{rest}^{i,k}$  and their gaussianity to implement an inference test for each channel  $k$ . We conduct a hypothesis test on the expected value of  $\hat{\beta}_{task}^{i,k} - \hat{\beta}_{rest}^{i,k}$ . In particular, for fixed channel  $k$ , the test will be:

$$\begin{cases} H_0 : \mu^k = 0 & \text{null hypothesis} \\ H_1 : \mu^k > 0 & \text{alternative hypothesis} \end{cases}$$

where  $\mu^k = E[\hat{\beta}_{task}^k - \hat{\beta}_{rest}^k]$  is the expected value of the linear combination of the coefficients. A one-tailed test is chosen due to the shape of the regressors and of the HRF.

Theoretically the decision of the test would be acceptance of the null hypothesis for the not-activated channels, and the rejection for the activated ones. In fact if a channel is activated we expect that the linear combination of the regressors is significant, and the coefficients related to it have expected value higher than 0.

Due to gaussianity of  $\hat{\beta}_{task}^k - \hat{\beta}_{rest}^k$  we can calculate for every test the following test statistic:

$$T = \frac{\bar{X}_n - 0}{\sqrt{S^2/10}}.$$

Under the null hypothesis it is distributed as a t-student with  $n - 1$  degrees of freedom. Here the sample size,  $n$ , is equal to 10,  $\bar{X}_n^k$  is the sample mean of  $\hat{\beta}_{task}^k - \hat{\beta}_{rest}^k$ , and  $S_k^2$  is the sample variance.

A P-value for each channel can be calculated as  $P(X > T_k)$ , where  $X$  is a random variable from a t-student distribution with  $n - 1$  degrees of freedom.

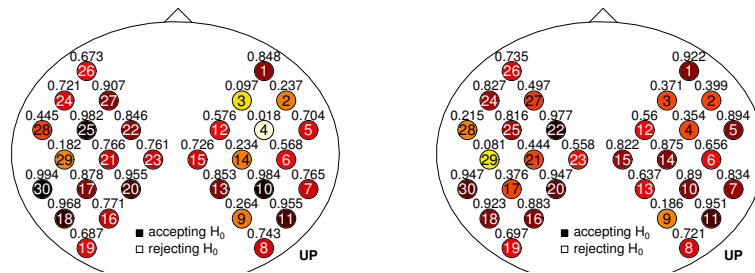
Now we can plot a map in which the colour of each channel is proportional to its P-value. Colours vary from white (activation) to black (no activation).

## 4.3 Activation maps

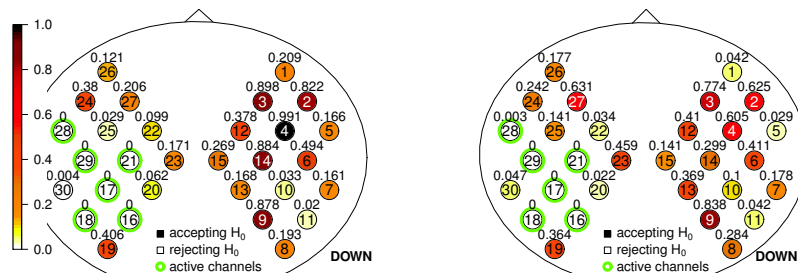
Tests on channels described in the previous section are applied on in vivo (INV2) and synthetic data, producing good results in both situations. We report here some of the obtained maps.

### Activation maps for synthetic data

Activation maps for synthetic data are reported in Fig. 4.5 (EXP1) and in Fig. 4.6 (EXP2). Maps concerning  $O_2Hb$  measures are on the left, maps for  $HHb$  are on the right. The top row of both figures is related to the superficial layer of the head, while the bottom row describes the deep layer.



(a)  $O_2Hb$ , superficial layer (EXP1). (b)  $HHb$ , superficial layer (EXP1).



(c)  $O_2Hb$ , deep layer (EXP1). (d)  $HHb$ , deep layer (EXP1).

Figure 4.5: Activation maps for synthetic data, EXP1. The numbers inside the circles are the channel numbers while the numbers outside the circles are P-values.

Channels simulated as active (in deep layer) are circled by green.

For dataset EXP1, obtained simulating ideal hemodynamic evolution without confounding oscillations, it is clear how the proposed method can discriminate the activated channels in the deeper region.

P-values related to activated channels are in fact close to 0 (equal to 0 rounding to the third decimal place), creating a sharp division in the map between white and coloured channels.

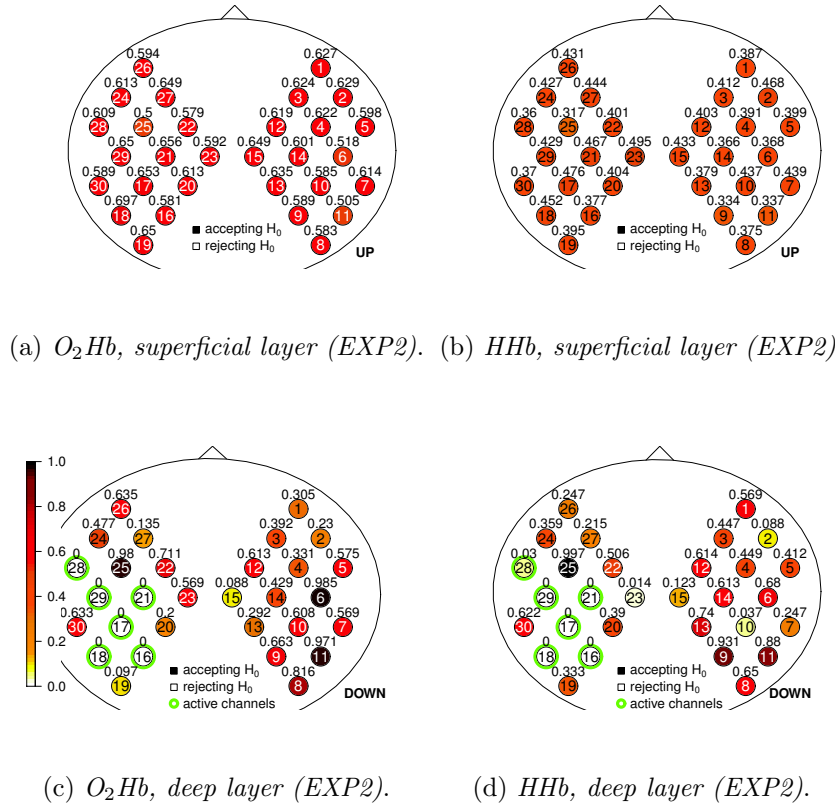


Figure 4.6: Activation map for synthetic data, EXP2. The numbers inside the circles are the channel numbers while the numbers outside the circles are the P-values.

If we choose a type I error of 0.05, applying a Bonferroni correction, we consider as activated channels with P-values lower than 0.0016 ( $0.0016 = 0.05/30$ ). We note that the map can discriminate the activated channels. More specifically, the lowest P-value (less than  $10^{-7}$ ) is the one referred to

channel 17, the most activated one (100% HRF), while channels with the lowest activation intensity (channels 16 and 28, 25% HRF) have the highest P-values among the activated ones (less than 0.0005). This confirms our choice of using P-values: they quantify the degree of activation of each channel with a high precision.

In the upper layer we don't find any activation, as expected, and P-values are all higher than 0.01.

Also in the activation map for the deeper layer of dataset EXP2 (Fig. 4.6) activated channels are instantly detectable.

In the superficial layer of EXP2 P-values are very high (higher than 0.5) and very uniform, confirming that the simulated O<sub>2</sub>Hb is noise.

We can notice in the HHb activation maps of both figures the same trends found for O<sub>2</sub>Hb. Revealing activation in this situation is more difficult, because activation amplitude is lower than in O<sub>2</sub>Hb measures. Nevertheless, this method performs a good channels classification on these measures too: the only channel with a slightly high P-value, compared to others, is 28 (25% HRF).

## Activation maps for in vivo data

Activation maps for in vivo data, INV2, are reported in Fig. 4.7, 4.8, 4.9 and 4.10.

In these maps P-values are slightly higher than in activation maps for synthetic data, but the procedure finds activated area in most of subjects.

In fact active channels in the left hemisphere can be clearly observed in maps related to O<sub>2</sub>Hb of subjects 0173, 0182, 0185, 0191, 0203 and 0206.

The other subjects show no activation in the hemisphere contralateral to the movement. This can be also due (in particular for subject 0188) to high noise that corrupts signals in some channels of the left hemisphere.

As for synthetic data, maps from HHb measures show the same features of O<sub>2</sub>Hb maps.

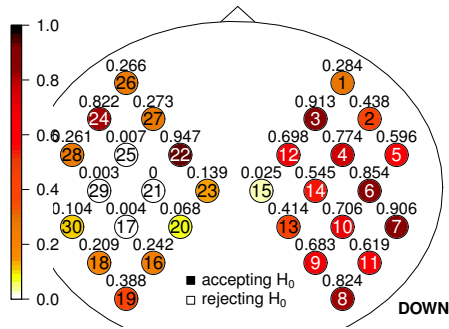
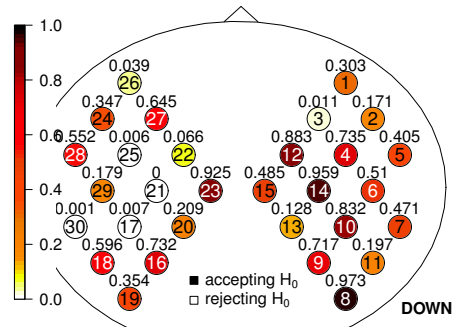
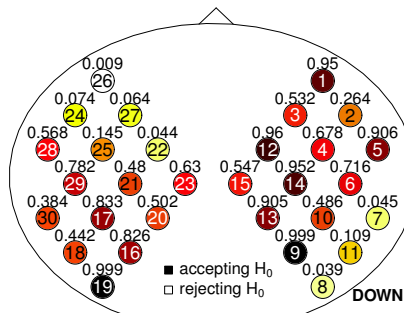
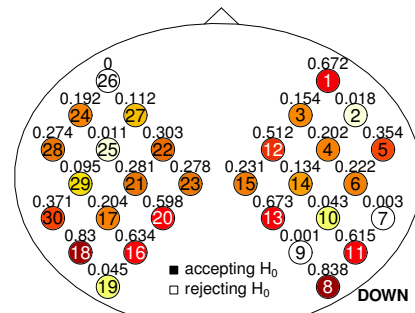
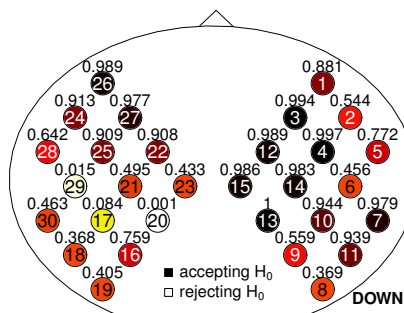
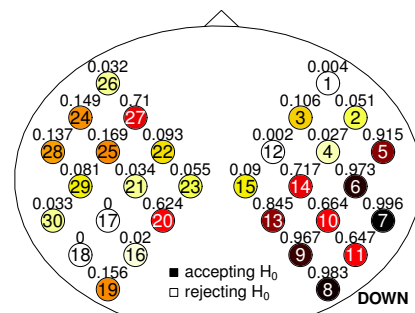
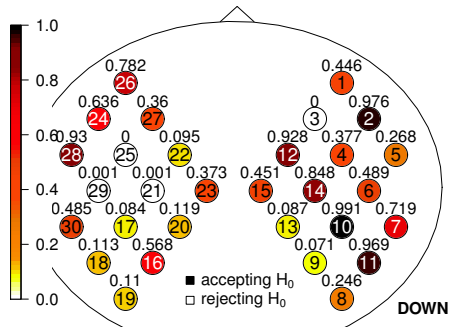
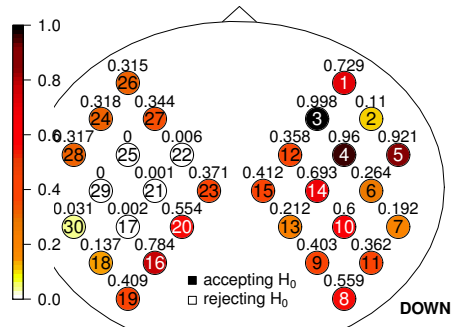
(a) Subject 0173,  $O_2Hb$ .(b) Subject 0173,  $HHb$ .(c) Subject 0176,  $O_2Hb$ .(d) Subject 0176,  $HHb$ .(e) Subject 0179,  $O_2Hb$ .(f) Subject 0179,  $HHb$ .

Figure 4.7: Activation maps for in vivo data (INV2). The numbers inside the circles are the channel numbers while the numbers outside the circles are the P-values.

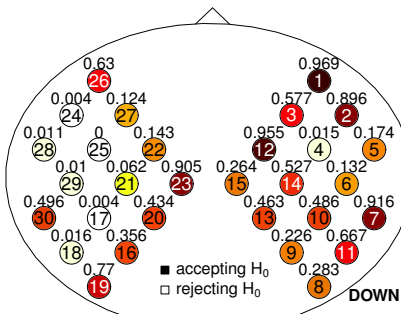




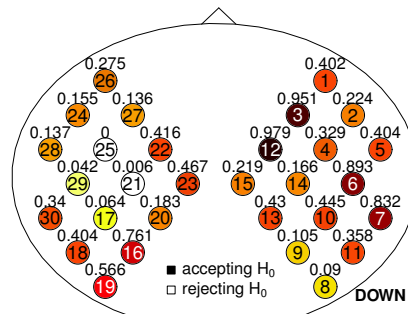
(a) Subject 0182,  $O_2Hb$ .



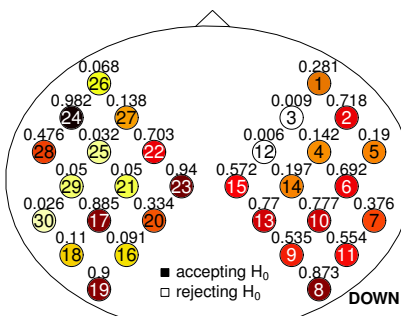
(b) Subject 0182,  $HHb$ .



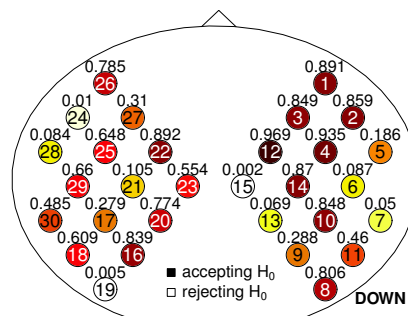
(c) Subject 0185,  $O_2Hb$ .



(d) Subject 0185,  $HHb$ .



(e) Subject 0188,  $O_2Hb$ .



(f) Subject 0188,  $HHb$ .

Figure 4.8: Activation maps for in vivo data (INV2). The numbers inside the circles are the channel numbers while the numbers outside the circles are the P-values.

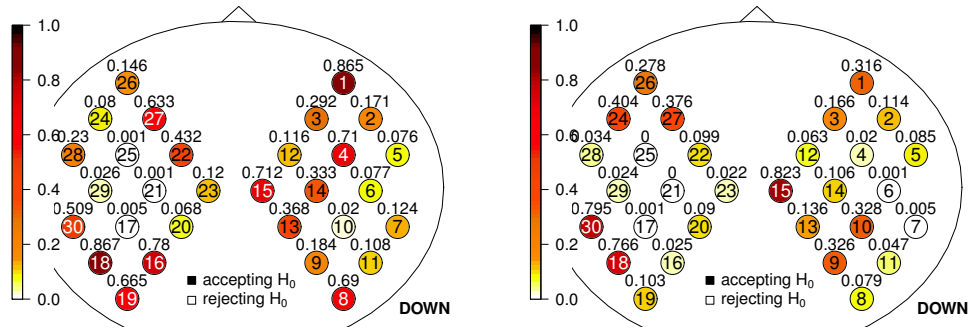
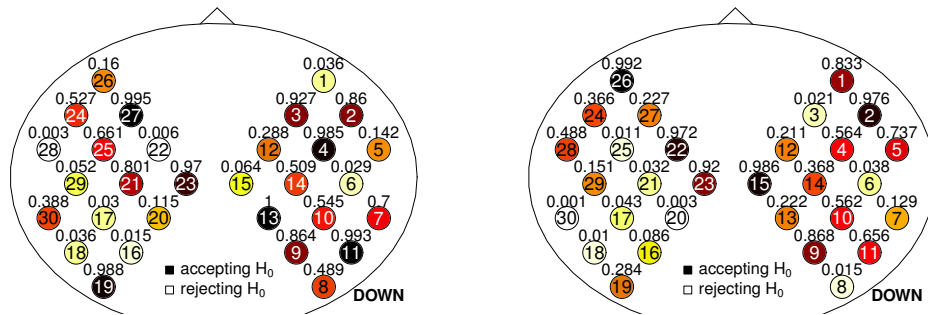
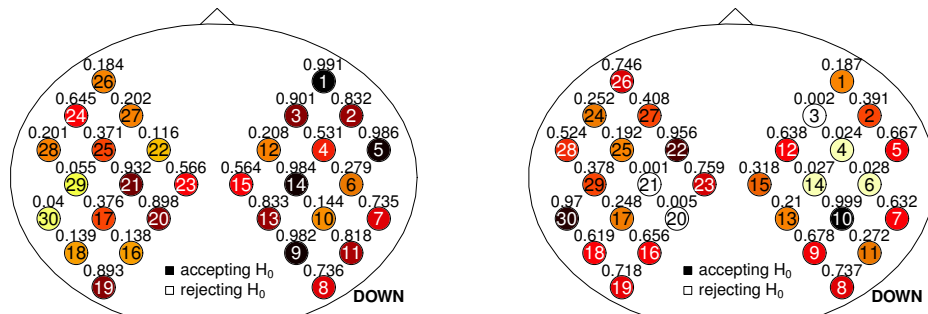
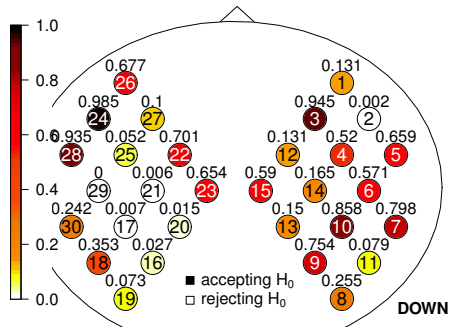
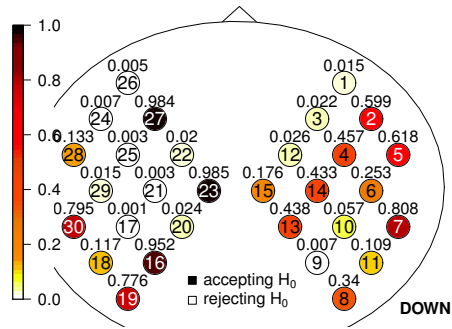
(a) Subject 0191,  $O_2Hb$ .(b) Subject 0191,  $HHb$ .(c) Subject 0197,  $O_2Hb$ .(d) Subject 0197,  $HHb$ .(e) Subject 0200,  $O_2Hb$ .(f) Subject 0200,  $HHb$ .

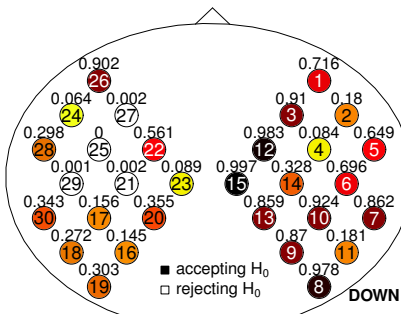
Figure 4.9: Activation maps for in vivo data (INV2). The numbers inside the circles are the channel numbers while the numbers outside the circles are the P-values.



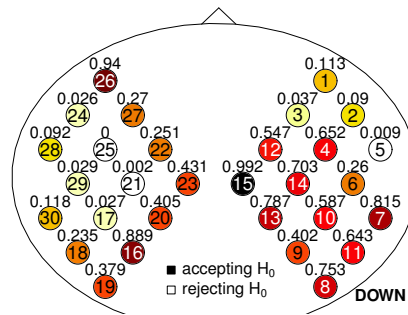
(a) Subject 0203,  $O_2Hb$ .



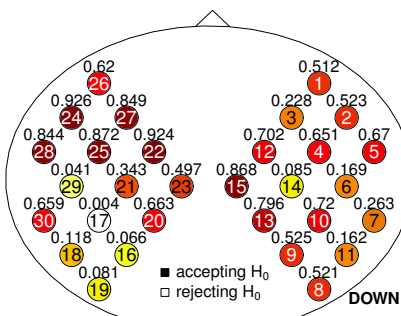
(b) Subject 0203,  $HHb$ .



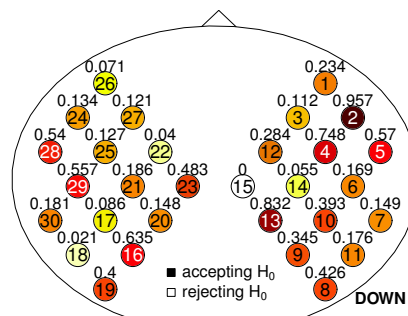
(c) Subject 0206,  $O_2Hb$ .



(d) Subject 0206,  $HHb$ .



(e) Subject 0209,  $O_2Hb$ .



(f) Subject 0209,  $HHb$ .

Figure 4.10: Activation maps for in vivo data (INV2). The numbers inside the circles are the channel numbers while the numbers outside the circles are the P-values.

## 4.4 K-means clustering algorithm

When an activation map shows activated areas the statistical analysis can be confirmed through k-means clustering algorithm. If  $k$  indicates the channel and  $i$  the trial, the following vector is considered for each channel:

$$\begin{pmatrix} \hat{\beta}_{task}^{1,k} - \hat{\beta}_{rest}^{1,k} \\ \vdots \\ \hat{\beta}_{task}^{i,k} - \hat{\beta}_{rest}^{i,k} \\ \vdots \\ \hat{\beta}_{task}^{10,k} - \hat{\beta}_{rest}^{10,k} \end{pmatrix}$$

A k-means algorithm is applied to the 30 vectors in  $\mathbb{R}^{10}$ . This clustering algorithm separates the 30 vectors in  $m$  groups, finding clusters that minimize the Euclidean distance within clusters and maximizes the one between clusters. We set  $m$  equal to 2, because we expect to observe two clusters: one with activated channels, one with not-activated ones. The algorithm consists of 3 steps:

1. Initialization, in which the initial centres are randomly fixed.
2. The Euclidean distances from centres are calculated for each vector, then vectors are assigned to the cluster with the nearest centre.
3. Updating of centres: the centre of each cluster is calculated as the mean between the vectors belonging to the cluster.

Steps 2. and 3. are repeated until convergence.

The k-means clustering algorithm works well if there are channels with “similar” vectors (thus with a similar evolution in time. This is expected to happen with activated channels). If there is no activation the algorithm is forced to separate channels in two groups, thus results are unpredictable and with no sense.

The choice of  $m = 2$  is confirmed also by the *average silhouette width*, a quality index allowing to select the number of clusters (Struyf et al., 1997). The index is calculated in the following way. If the number of clusters  $m$  is

fixed,  $i$  indicates one of the thirty classified vectors and  $A$  is the cluster to whom  $i$  belongs, the average dissimilarity of  $i$  to all other vectors of  $A$  is:

$$a(i) = \frac{1}{|A| - 1} \sum_{j \in A, j \neq i} d(i, j), \quad (4.2)$$

where  $d(i, j)$  is the Euclidean distance between  $i$  and  $j$ .

Similarly, for any cluster  $C$  different from  $A$ , the average dissimilarity of  $i$  to all objects of  $C$  can be calculated as:

$$d(i, C) = \frac{1}{|C|} \sum_{j \in C} d(i, j). \quad (4.3)$$

After computing  $d(i, C)$  for all clusters  $C \neq A$ , we take  $b(i) = \min_{C \neq A} d(i, C)$ . Then the *silhouette value*  $s(i)$  of vector  $i$  is defined as

$$s(i) = \frac{b(i) - a(i)}{\max\{a(i), b(i)\}}. \quad (4.4)$$

The silhouette value varies from -1 to 1, increasing if the algorithm well classifies the vector, decreasing if it is badly classified.

Now we can calculate the average silhouette width  $w$ , defined as the average of the  $s(i)$  over all vectors  $i$  in the dataset:

$$w = \frac{1}{30} \sum_{i=1}^{30} s(i). \quad (4.5)$$

K-means is performed several times, each time with a different number of clusters  $m$ . Then resulting average silhouette width  $w$  are compared and k-means with the highest  $w$  is chosen.

For synthetic data EXP1, if  $m = 2$ ,  $w$  is equal to 0.85 for O<sub>2</sub>Hb, equal to 0.76 for HHb. If  $2 < m < 7$  we obtain  $w < 0.36$  for both hemoglobins. Similar values are obtained for EXP2, where  $w = 0.86$  (O<sub>2</sub>Hb) and 0.8 (HHb) if  $m = 2$ ;  $w < 0.5$  for  $2 < m < 7$ .

Also in vivo data (INV2) show the highest index for  $m = 2$  (for example, O<sub>2</sub>Hb of subject 0173 has  $w = 0.40$  for  $m = 2$ ,  $w \simeq 0.20$  in the other cases). Thus  $m = 2$  is the best choice to perform activation detection.

The unique exception happens on subjects with highly noisy channels: in this situation the highest  $w$  can be obtained with  $m > 2$ , since the clustering

algorithm separates noisy channels, activated and not-activated ones. We will see an example of this situation in the next pages.

Silhouette indexes are calculated with the R package `cluster` (Maechler et al., 2013).

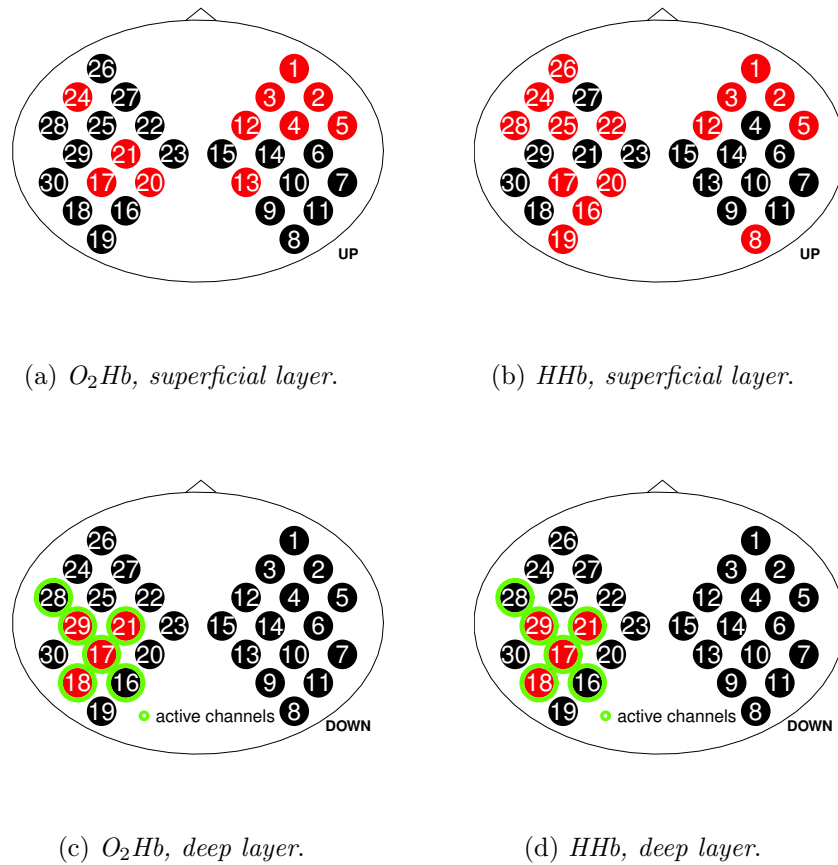


Figure 4.11: K-means activation for EXP1. Channels simulated as active are circled in green. The numbers inside the circles are the channel numbers while colors identify the two clusters.

K-means activation maps for synthetic data are reported in Fig. 4.11 and 4.12 for EXP1 and EXP2, respectively.

In these images channels from different clusters are represented in different colours. Channels simulated as active (in deep layer) are circled by green.

The k-means algorithm is able to identify most of the activated channels

for both  $O_2Hb$  and  $HHb$  in the deep layer. The channels that present a higher activation intensity (channels 17, 18, 21, 29) are precisely clustered, for both EXP1 and EXP2,  $O_2Hb$  and  $HHb$  measures. Conversely, channels 16 and 28, that present a low intensity of activation (25% HRF), are assigned to the cluster of not-activated ones. In fact k-means algorithm separates channels in two sharp groups: the output is a binary assignment of each channel, that is simply labelled as “active/not-active”. Thus it can happen that low activated channels are assigned to the cluster of not-activated ones.

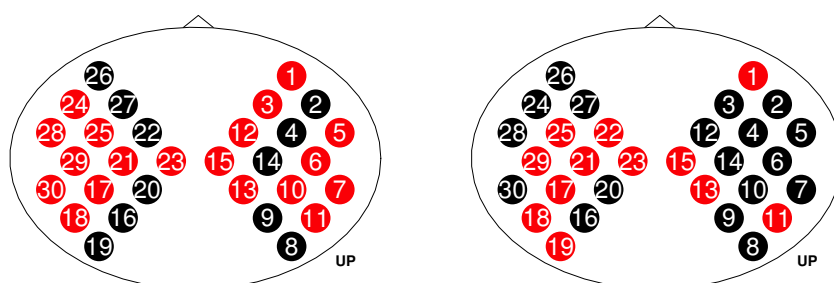
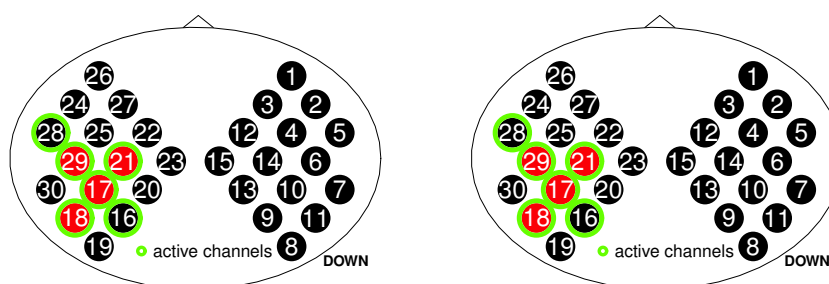
(a)  $O_2Hb$ , superficial layer.(b)  $HHb$ , superficial layer.(c)  $O_2Hb$ , deep layer.(d)  $HHb$ , deep layer.

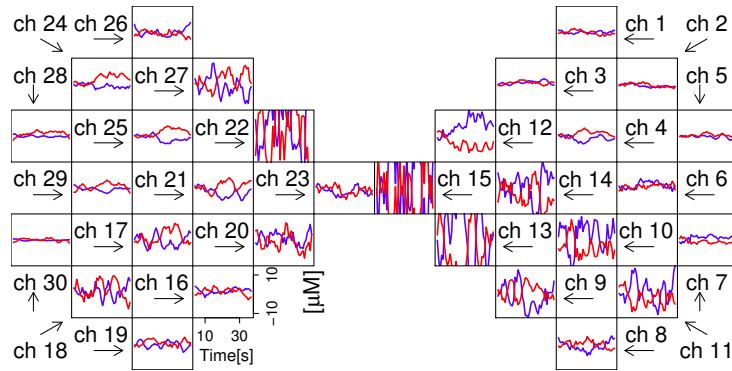
Figure 4.12: K-means activation for EXP2. Channels simulated as active are circled in green. The numbers inside the circles are the channel numbers while colors identify the two clusters.

If there is no activation, as happens in the upper layer, the algorithm is

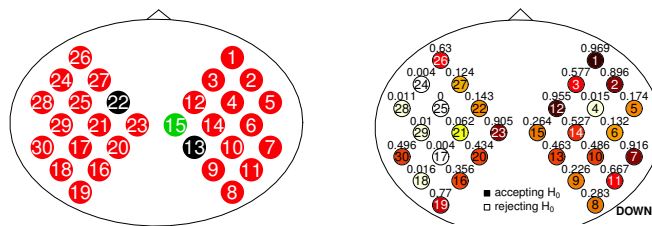
not suitable. In fact it is forced to separate channels in two groups, even if vectors shouldn't be divided in two clusters. Thus results are unpredictable.

Some problems can also arise if one (or more) channels are particularly noisy and product vectors much different from the others: in this situation the k-means algorithm can be inaccurate, separating noisy channels from the others.

This happens for some of in vivo subjects, for example 0176. As shown in Fig. 4.13a, this subject has several noisy channels (e.g. 10, 11, 13, 14, 15, 22). In this situation k-means algorithm with  $m = 2$  separates channel 15 from all the others. The average silhouette width  $w$  is high (0.88), but the reason of this classification is clearly not dependent on activation.



(a) *Folded data for subject 0185.*



(b) *K-means for 0185,  $m = 3$ .* (c) *Activ. map for 0185,  $O_2Hb$ .*

Figure 4.13: Folded data, k-means and activation map for subject 0185.

Excluding  $m = 2$ , the highest average silhouette width is obtained for  $m = 3$  ( $w = 0.79$ ). The clusterization with  $m = 3$  is reported in Fig. 4.13b. Here the algorithm separates channel 20 and some of the other channels with



the highest noise (channels 13 and 22). We can't find any relation between k-means clusterization and the activation map in Fig. 4.13c. This confirms that subjects with several noisy channels are difficult to treat with k-means. Noise corrupts not only some channels, but the whole clusterization, because channels are not treated independently one from the other as for activation maps of Section 4.3.

For this reason highly noisy channels should be excluded before an analysis with k-means.

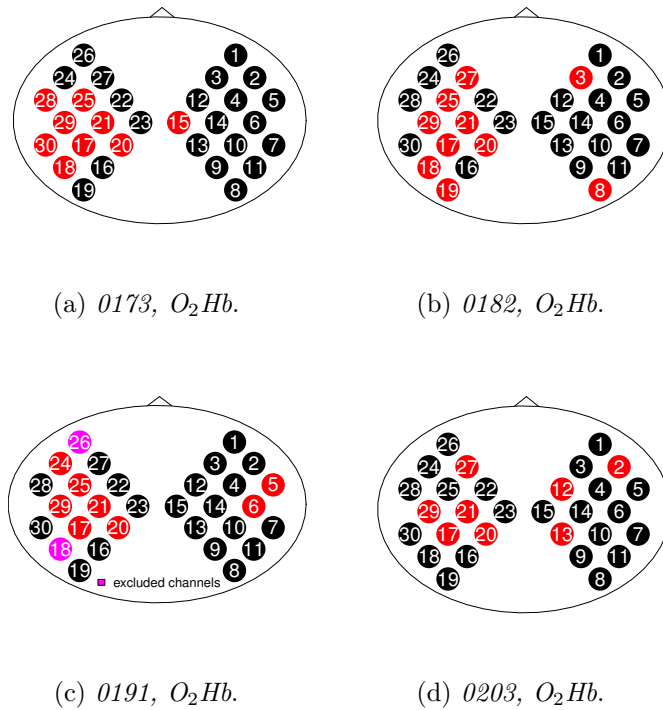


Figure 4.14: K-means activation for some of in vivo data. The numbers inside the circles are the channel numbers while colours identify the two clusters. Pink channels have been excluded.

Nevertheless k-means clustering algorithm produces good results on in vivo subject with low noise. Fig. 4.14 reports activation maps for  $O_2Hb$  (INV2) of subjects with activated areas. We notice that the algorithm correctly classifies most of channels.

K-means clustering algorithm follows a different procedure compared to the linear regression model. It aims to detect the same channels applying another kind of analysis, that doesn't use statistical tests and is based on different hypothesis. Thus it can be an important instrument of control: its right clustering is a further confirm of the accuracy of the previous analysis and of the calculated activation maps.

## 4.5 Group Analysis

If we want to compare the hemodynamic response between two different groups (typically, a set of healthy subjects and a set of patients), a group analysis is needed. The group analysis should summarize information from all the subjects of the group, producing a map that synthesizes the ones from single subjects.

In literature (see Ye et al., 2009; Tak, Ye, 2014) this is usually performed through a two-levels analysis, where parameters of interest at the group level are estimated from parameter and variance estimates from the single-session level (i.e. from the GLM on single subjects).

This procedure approximates a single-level mixed effect model that processes all group data together and estimates parameters of interest at the group level directly from the single sessions. If  $\mathbf{y}$  is the hemoglobin concentration ( $O_2Hb$  or  $HHb$ ) for a fixed channel and subject, the single-level mixed effect model would be:

$$\mathbf{y} = X\boldsymbol{\alpha} + X\boldsymbol{\eta} + \boldsymbol{\varepsilon} \quad (4.6)$$

where  $X$  is the known design matrix,  $\boldsymbol{\varepsilon}$  is a vector of errors,  $\boldsymbol{\alpha}$  denotes the group mean (equal for all the subjects in the group) and  $\boldsymbol{\eta}$  denotes a between-subject random effect parameter (depending on each subject). Group level statistics are obtained working with parameter  $\boldsymbol{\alpha}$ .

The approximation of this model through a two-levels analysis has the advantage of using yet calculated statistics from single sessions, making group analysis much simpler.

We suggest some ideas to perform a group analysis that suits the proposed activation detection procedure.

A first attempt consists in using all trials from a fixed channel, independently from the subject to whom they belong, for the same hypothesis test. We build a dataset of 30 channels, each channel including 120 (= 10 trials  $\times$  12 subjects) trials. We calculate 120 contrasts  $\hat{\beta}_{task}^{i,k} - \hat{\beta}_{rest}^{i,k}$ , with  $i = 1 : 120$ , for each channel  $k$ , performing an inference test on the mean on each of these samples of size 120<sup>1</sup>. Finally we use P-values from the hypothesis tests to draw a group map.

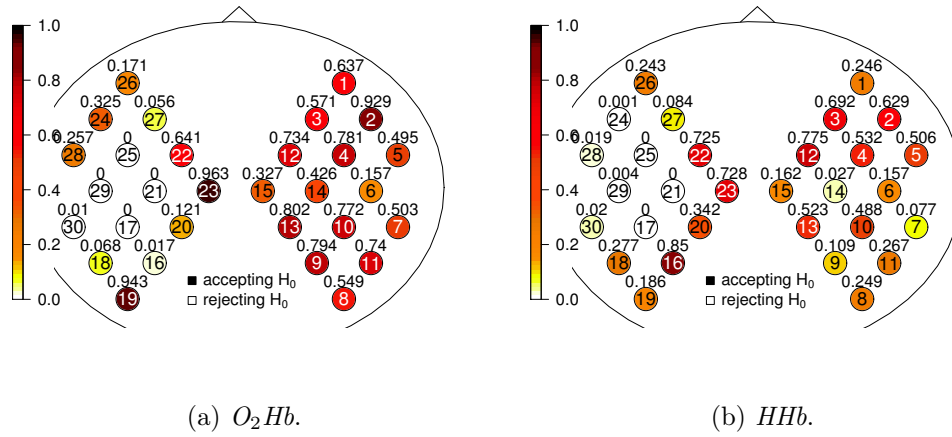


Figure 4.15: Group analysis maps calculated on 120 trials. For each fixed channel, trials are used as if they belonged to a unique subject.

The group map for INV2 resulting from this procedure is reported in Fig. 4.15, for  $O_2Hb$  and  $HHb$  measures. We can observe an activated area in the left hemisphere of both maps.

With this model we don't combine the information extracted from each subject (represented by P-values): we put signals together, and then we extract an information from mixed signals.

If we look for an approach that takes advantage from previously calculated P-values we can follow another procedure: we draw a group map in which the color of each channel is proportional to the mean of P-values calculated

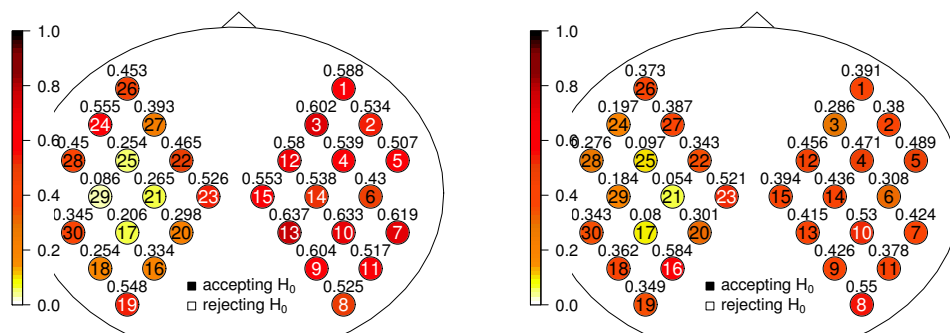
<sup>1</sup>A sample with more than ten contrasts - surely belonging to the same subject, and not from different subjects - could be useful to obtain a more precise test on the gaussianity of the sample. For this reason longer experiments could be considered.

in the analysis on single subjects.

The map built with the mean of P-values in subjects is reported in Fig. 4.16, for  $O_2Hb$  and HHb measures.

Looking at this figure we don't notice any activated channels. This happens because the mean suffers from extreme values: a high P-value (from an anomalous signal or a not-activated subject) makes the mean much higher in the channel.

In order to resolve this problem we can use the median of single-level P-values instead of the mean: in fact the median remains stabler varying extreme values.



(a) Group mean of P-values,  $O_2Hb$ .

(b) Group mean of P-values, HHb.

Figure 4.16: Group analysis maps obtained through mean of P-values.

Resulting map with median of P-values is reported in Fig. 4.17, for  $O_2Hb$  and HHb measures. As we supposed, the map is less influenced by “outlier subjects” and it shows an area with low P-values in the central region of the left hemisphere.

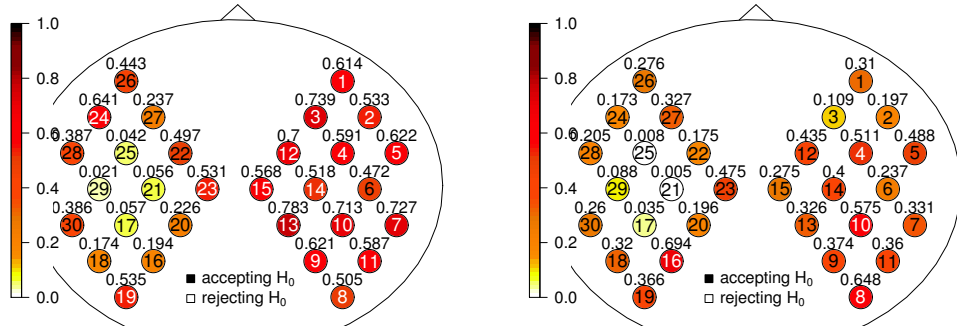
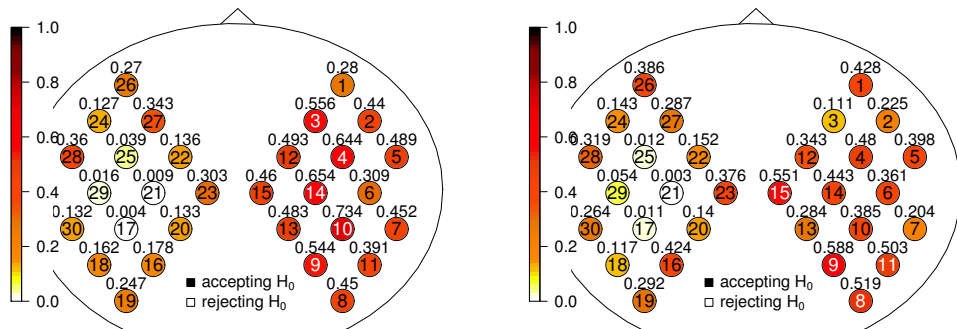
No correction is performed on P-values, thus results must be treated with attention. In fact twelve hypothesis tests (one for each subject) are performed simultaneously for a fixed channel, increasing the chances of obtaining false-positive results.

It is clear that group analysis are influenced by subjects whose single map doesn't show activated channels (because of noise or no real activation). It is

interesting to compare Fig. 4.17, reporting maps with median P-values for INV2, with Fig. 4.18, reporting the same maps for INV1.

Maps related to dataset INV1 show lower P-values than the ones from INV2. Maybe this difference depends on the lower noise that afflicts dataset INV1 respect of INV2.

A future study could improve these group-level analysis considering P-values corrections, and inspecting the influence of noise (for example, through an exclusion of noisy channels).

(a) Group median of  $P$ -values,  $O_2Hb$ .(b) Group median of  $P$ -values,  $HHb$ .Figure 4.17: Group analysis maps obtained through median of  $P$ -values.(a) Group median of  $P$ -values,  $O_2Hb$  for (b) Group median of  $P$ -values,  $HHb$  for  $INV1$ .  
 $INV1$ .Figure 4.18: Group analysis maps obtained through median of  $P$ -values for  $INV1$ .

# Chapter 5

## Bayesian analysis

We propose here a bayesian approach to fNIRS activation detection problem. We introduce this alternative point of view, compared to the frequentist approach described so far, in order to confirm and enrich results of the previous chapter, on the one hand, and on the other hand to extend our knowledge on this subject inspecting features that have been ignored till now.

In fact, two analysis are proposed. At first data are inspected as time series, following an approach new to us and analysing the correlation structure of data, that haven't been studied till now. Then a bayesian linear model is illustrated: it is similar to linear models of Chapter 4 and it can be used as a further confirmation and development of results already obtained.

In this chapter methods are applied to the 10 trials (40 s each) of O<sub>2</sub>Hb of subject 0173, from dataset INV2. Some subjects from the same dataset are used to estimate hyperparameters of priors in the bayesian linear model.

Not to weigh the exposition down, we will often focus on the eight central channels of the brain (four from the left hemisphere, all activated for subject 0173, four from the right one, all not-activated), proposing a comparison between channels in the two regions.

### 5.1 Bayesian analysis of time series

A first approach to the problem consists in studying correlation between hemoglobin concentration in different channels. If we found different time

series in active channels, we would be able to reach our goal of activation detection.

If  $y_t^k$  is O<sub>2</sub>Hb measure in channel  $k$  at time  $t$ , with  $k = 1 : 30$ ,  $t = 1 : 400$ , we can build the following linear regression model:

$$y_t^k = \beta_0^k + \beta_1^k y_{t-1}^k + \varepsilon_t^k, \quad \text{with} \quad \varepsilon_t^k | \sigma^2 \stackrel{iid}{\sim} \mathcal{N}(0, \sigma^2) \quad \begin{cases} \forall & t = 1:400 \\ \forall & k = 1:30 \end{cases} \quad (5.1)$$

We can then obtain the likelihood for  $y_t^k$ , considering that

$$y_t^k | y_{t-1}^k, \beta^k, \sigma^2 \stackrel{iid}{\sim} \mathcal{N}(\beta_0^k + \beta_1^k y_{t-1}^k, \sigma^2).$$

We choose for  $\beta^k$  and  $\sigma^2$  the following prior distributions:

$$\beta^1, \dots, \beta^k, \dots, \beta^{30} \stackrel{iid}{\sim} \mathcal{N}(\mathbf{0}, 100 \cdot I_2), \quad \text{with } I_2 \text{ identity matrix,}$$

$$\sigma^2 \sim U(0, 2000).$$

We choose two non-informative priors, assigning to  $\beta^k$  and  $\sigma^2$  a high variance.

We use this kind of model and not, for example, a bayesian hierarchical model<sup>1</sup> (that will be used, in a different context, in the next section), because our interest is oriented in evaluating the posterior densities of  $\beta_1^k$ , comparing them for different  $k$ . With a hierarchical model we would inspect variables that describe the common features of all the channels (e.g. a variable representing the expected value of  $\beta_1^k$  in all channels), studying the shared characteristics instead of the ones that allow a separation between channels.

We want to inspect  $\beta_1^k$  because it specifies the relation between data at a certain time and at the previous instant: we are interested in verifying if activated channels show a different dependence in time.

For the sake of simplicity  $\sigma^2$  is equal for all channels: we verified that results don't change assuming different  $\sigma^2$  for each channel.

We run a Markov Chain Monte Carlo (MCMC) simulation with the software Jags (see Plummer, 2003) to obtain the posterior densities of the parameters. We run 53.000 iterations, with a burn-in of 3000 and a thinning of 10.

---

<sup>1</sup>Hoff (2009)



Then we verify the convergence of the chain through Geweke's statistic, Kolmogorov-Smirnov's test, Heidelberger and Welch's convergence diagnostic and visual inspection of traceplots and autocorrelation plots (for details on these methods, see Section 5.3). We obtain very good results of convergence for all parameters (for an example, see traceplots and autocorrelation plots in Fig. 5.1 and 5.2).

The proposed model doesn't help in activation detection, though. In fact if we compare the posterior densities of  $\beta^k$  we can't find significant differences between  $\beta^k$  from activated and not-activated channels.

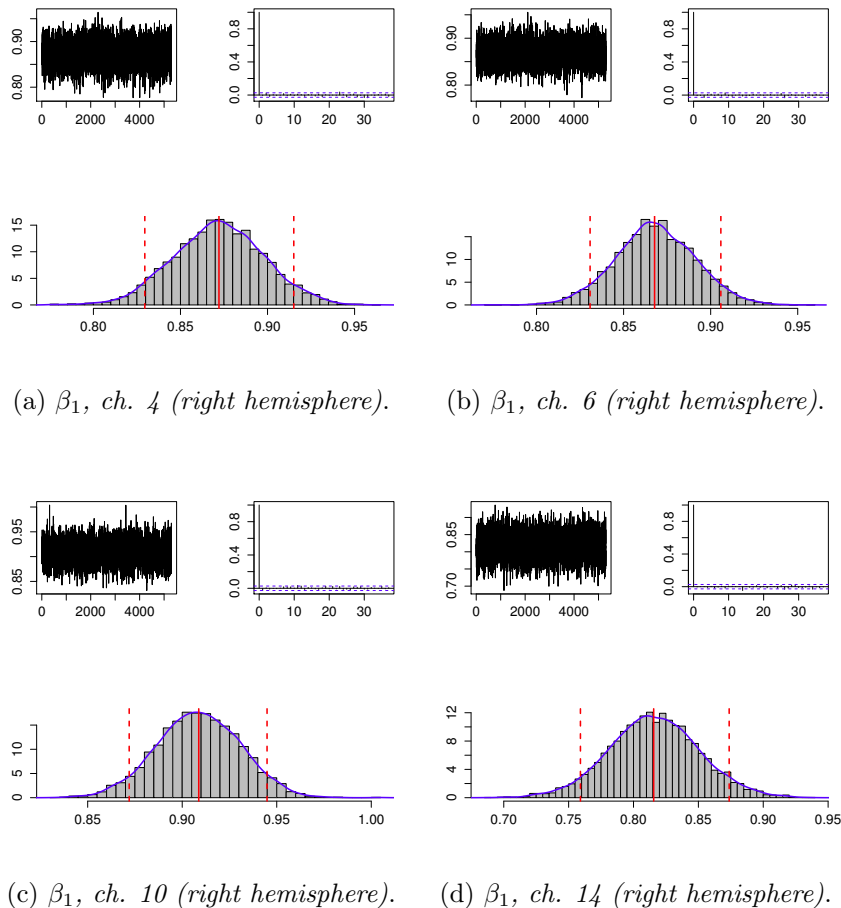


Figure 5.1: Traceplot, Autocorrelation function and posterior densities for  $\beta_1$  of not-activated channels (channels 4, 6, 10, 14).

In order to prove this, we report the posterior densities of  $\beta_1^k$  from the four central channels of right hemisphere (Fig. 5.1), that can be compared with the central channels from left hemisphere (Fig. 5.2). The mean of the distribution is similar in all channels (around 0.85-0.9) and also the variance doesn't seem to change.

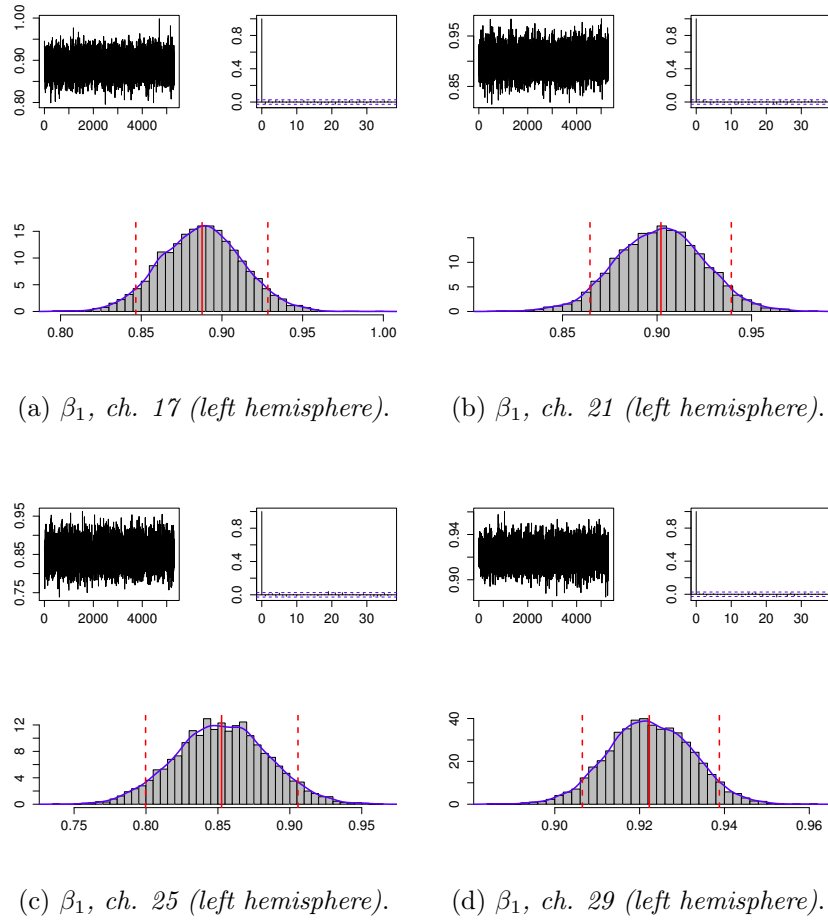


Figure 5.2: Traceplot, Autocorrelation function and posterior densities for  $\beta_1$  of activated channels (channels 17, 21, 25, 29).

For a quicker comparison of  $\beta_1^k$  from all channels we can observe Fig. 5.3. It shows the Highest Posterior Density (HPD) regions for  $\beta_1^k$  in all channels. Quantiles of order 0.05, 0.5 and 0.95 are marked with points, channels in which we want to find activation are in red. Segments in red are not different

from the others: we would like to find that they can be easily distinguished, for example because they are shorter than the blue ones, or because they lie around different  $y$ -axis values. A confirm of the similarity between segments length can be obtained looking at Fig. 5.4, in which lengths of HPD regions are shown.

From a simple visual inspection of these images we understand that it is difficult to separate active channels studying only the correlation structure. This is due to the high correlation of  $y_t^k$ , that doesn't depend on specific channels. Not-activated channels show a high temporal correlation, similar to the ones in activated channels. This happens because data indicate the concentration of a substance during time in a fixed region: we found that the relation between data in consecutive instants is very strong, independently on the activation of each fixed channel. Thus a model that inspects only data correlation can't find the desired classification.

For this reason we move to a different procedure, using a regressor that mimic the Hemodynamic Response Function (HRF), as in frequentist approach of Chapter 4.

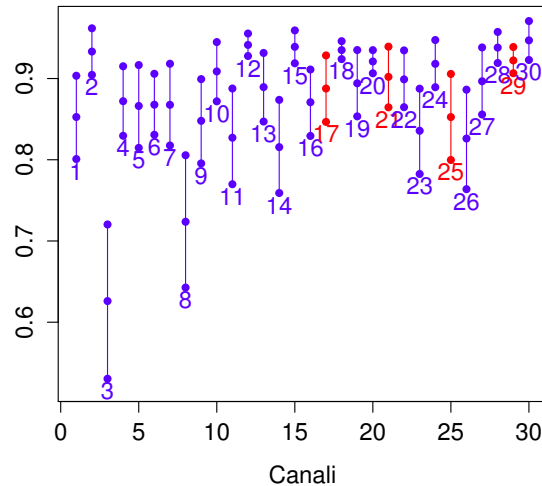


Figure 5.3: HPD intervals for  $\beta_1$  in each channel. Quantiles of order 0.05, 0.5 and 0.95 are marked with points. Channels in which we want to find activation are in red.

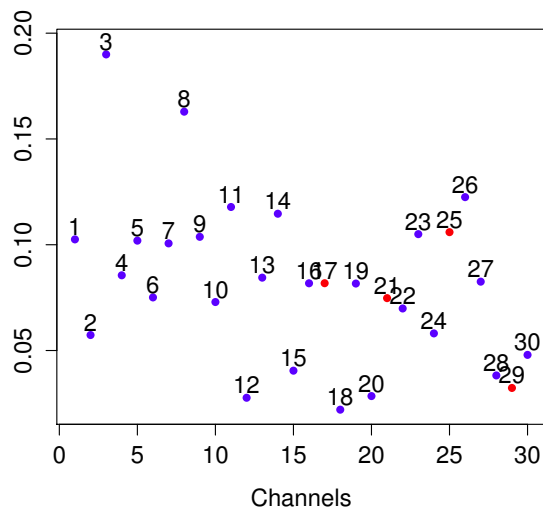


Figure 5.4: Length of HPD intervals for  $\beta_1$  in each channel. Channels in which we want to find activation are in red.

## 5.2 A hierarchical linear regression model

Considering data as time series we don't reach our objective of activation detection: we need a model that evaluates the shape of data, its specific evolution in time. We implement this model taking advantage from the previous knowledge and from the frequentist analysis seen in Chapter 4. As in that situation (and in the GLM of the current literature), we use a regressor that mimics the ideal hemodynamic response.

With this model we would like to confirm the results already obtained in Chapter 4, and to enrich them through a bayesian analysis on the posterior distributions. We won't observe only a numeric value for the classification (e.g. the P-values of the activation maps or the labels of the k-means clustering algorithm), but a whole distribution.

We divide signals in 10 trials of 40 s, applying a linear regression model to each of them.

For each fixed channel,  $\mathbf{y}^j$  is the O<sub>2</sub>Hb concentration in sub-interval  $j$ , with  $j = 1 : 10$ ,  $\mathbf{R}$  is the regressor *rest*, reported in Fig. 5.5, and  $X$  is the

design matrix:

$$\mathbf{y}^j = \begin{bmatrix} y_1^j \\ y_2^j \\ \vdots \\ y_{40}^j \end{bmatrix}, \quad \mathbf{R} = \begin{bmatrix} r_1 \\ r_2 \\ \vdots \\ r_{40} \end{bmatrix}, \quad X = \begin{bmatrix} 1 & r_1 \\ 1 & r_2 \\ \vdots & \vdots \\ 1 & r_{40} \end{bmatrix}. \quad (5.2)$$

As in the frequentist model of Chapter 4, the regressor  $\mathbf{R}$  is obtained through a convolution between the HRF and a step-function equal to 1 in the first and last 10 s and 0 elsewhere, in order to reproduce the alternation of task and rest periods. We use only one regressor, *rest*, to simplify the procedure and the computations. In fact, following the current literature, the proposed

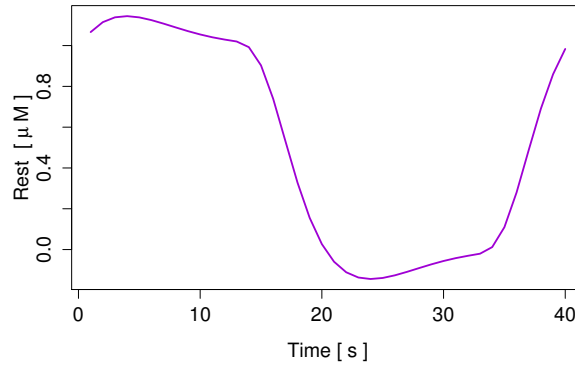


Figure 5.5: The regressor, *rest*.

frequentist analysis implements a model with two regressors, studying their linear combination. However the same statistical results can be obtained using a single regressor, therefore we here opt for the simplest model.

For each fixed channel, we set:

$$\mathbf{y}^j = X\boldsymbol{\beta}^j + \boldsymbol{\varepsilon}^j, \quad \text{with } \boldsymbol{\varepsilon}^j | \Sigma \stackrel{iid}{\sim} \mathcal{N}_{40}(\mathbf{0}, \Sigma), \quad \text{for } j = 1 : 10. \quad (5.3)$$

We choose the following hierarchical model:

$$\begin{aligned} \mathbf{y}^j | X, \boldsymbol{\beta}^j, \Sigma &\stackrel{iid}{\sim} \mathcal{N}_{40}(X\boldsymbol{\beta}^j, \Sigma) \quad \text{for } j = 1 : 10, \\ \boldsymbol{\beta}^j | \boldsymbol{\mu}, \lambda &\stackrel{iid}{\sim} \mathcal{N}_2(\boldsymbol{\mu}, \lambda \cdot I_2) \quad \text{for } j = 1 : 10, \end{aligned}$$

$$\begin{aligned}\mu_0, &\sim \mathcal{N}(a, b), \\ \mu_1 &\sim \mathcal{N}(a', b'), \\ \lambda &\sim \text{invGamma}(c, d).\end{aligned}$$

In this model, for each fixed channel, the random variable  $\boldsymbol{\mu}$  synthesizes the information derived from  $\boldsymbol{\beta}$ . In particular we are interested in  $\mu_1$ : we will try to understand if this random variable has a specific distribution for active channels. We will calculate the posterior densities for  $\mu_1$  in each channel and then we will compare them.

We fix hyperparameters  $a, b, a'$  and  $b'$  using other subjects from in vivo dataset.

We still have to define the matrix  $\Sigma$ . Since  $\Sigma$  is a  $40 \times 40$  matrix, we have to choose a known structure, not to estimate too many parameters<sup>2</sup>. We choose a matrix of an ARMA(1,1) process, defined as:

$$\Sigma = \sigma^2 \cdot \begin{bmatrix} 1 & \gamma & \gamma\phi & \gamma\phi^2 & \gamma\phi^3 & \dots \\ \gamma & 1 & \gamma & \gamma\phi & \gamma\phi^2 & \dots \\ \gamma\phi & \gamma & 1 & \gamma & \gamma\phi & \dots \\ \vdots & \vdots & \vdots & \vdots & \vdots & \ddots \end{bmatrix}. \quad (5.4)$$

If parameters  $\sigma^2$ ,  $\phi$  and  $\psi$  are specified, the matrix is completely defined. In order to obtain a positive definite matrix we choose the following prior distributions:

$$\begin{aligned}\sigma &\sim U(0, 10), \\ \vartheta &\sim U(-1, 1), \\ \phi &\sim U(0, 1),\end{aligned}$$

with  $\sigma^2 = \sigma \cdot \sigma$  and  $\gamma$  equal to the following deterministic transformation:

$$\gamma = \frac{(\phi - \vartheta)(1 - \phi\vartheta)}{(1 - \phi^2) + (\phi - \vartheta)^2}.$$

Using Jags, we run an MCMC simulation with 185000 iterations, a thinning of 35 and a burn-in of 5000.

---

<sup>2</sup>An alternative approach could be using a common correlation matrix for all channels, as usually happens in Statistical Parametric Mapping (see Friston et al., 1994).

## 5.3 Convergence analysis

All the simulated Markov Chains are convergent. Their convergence was tested with the following instruments.

### Geweke's statistic

For each parameter, Geweke's convergence diagnostic considers two parts of the Markov chain (usually, the first 10% and the last 50%) comparing their means with a test on the difference of the means, in order to see if the two parts belong to the same distribution<sup>3</sup>.

The final output is a statistic from a Z distribution, that has to be compared with the 0.025 and 0.975 quantiles of a standard normal distribution (they are equal to  $\pm 1.96$ ): if Z-score is included in the interval  $(-1.96, 1.96)$ , the Markov Chain is convergent. With our data, this condition is verified for all parameters of each channel.

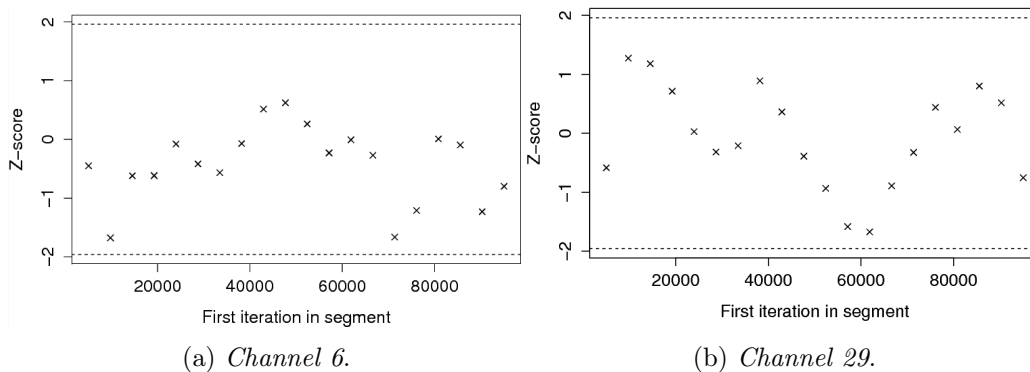


Figure 5.6: Geweke plot for  $\mu_1$  in two channels.

Fig. 5.6 shows how Geweke's Z-statistic varies if the first iterations are discarded. To do this, the first half of the Markov chain is divided in  $l$  segments (we choose  $l = 19$ ), then Geweke's Z-statistic is repeatedly calculated. The first Z-statistic is calculated with all iterations in the chain, the second one after discarding the first segment, the third after discarding the first two

<sup>3</sup>An alternative method to verify if samples have the same distribution could be comparing two parts of the chain through a Kolmogorov-Smirnov's test.

segments, and so on. The last Z-statistic is calculated using only the samples in the second half of the chain.

### **Heidelberg-Welch's diagnostic**

Heidelberg-Welch's diagnostic performs a convergence test (based on Cramer-Von Mises statistic) to accept or reject the null hypothesis that the sample values come from a stationary distribution. This method is composed of two steps:

1. The test is applied to the whole chain, accepting or rejecting the null hypothesis that the chain comes from a stationary distribution. If the null hypothesis is rejected, the first 10% of the chain is discarded and then the test is repeated. If the result of the test is another rejection, the next 10% of the chain is discarded, and so on until the null hypothesis is accepted or the 50% of the chain has been discarded. If the last test result is a rejection the chain is not convergent and a longer MCMC is needed. If the stationarity test is passed, the number of iterations to keep and the number to discard are reported.
2. If the test is not failed, a 95% confidence interval for the mean is calculated, using the portion of the chain which passed the stationarity test. Then half the width of this interval is compared to the estimate of the mean: if the ratio between the two quantities is low enough, the test is passed and the chain estimates the mean of the parameter with sufficient accuracy. Otherwise a longer MCMC is required.

We always obtain passed tests, and the number of iterations to discard is often 0.

### **Traceplots, autocorrelation and effective sample size**

Another way to verify the convergence of the chain consists in controlling that the chain visits the whole parametric space. In fact if the chain needs several iterations to move in the space, it will have a slow convergence.



To control this we can observe traceplots. Traceplots show the values assumed by parameters at each iteration. As an example we report traceplots related to the parameter  $\mu_1$  for channel 4 (not-activated) and 25 (activated) in Fig. 5.7.

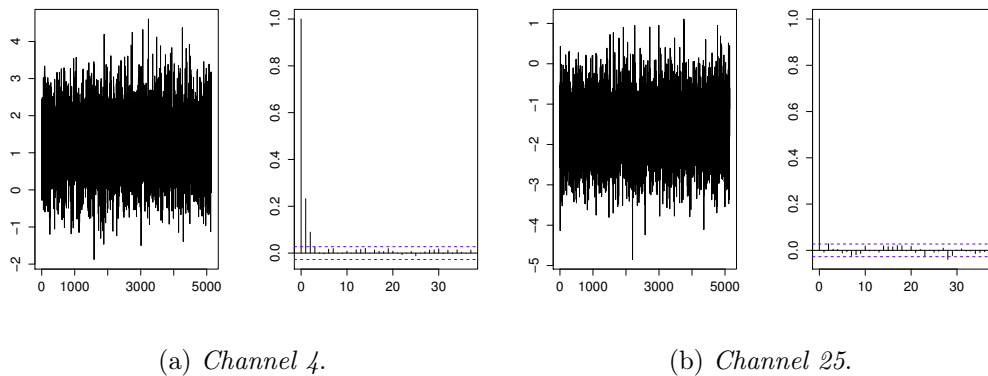


Figure 5.7: Traceplot and autocorrelation plot for  $\mu_1$  in two channels.

In the same figure we can see two examples of autocorrelation plots: they show the autocorrelation in the sample during time. Plots reveal a low autocorrelation, confirming the pertinence of the used thinning.

The stationarity of the chain can be inspected also by cumulative quantile plots. They show the evolution of the sample quantiles as a function of the number of iterations. An example of this kind of graph is reported in Fig. 5.8, for the parameter  $\mu_1$  of two channels.

We finally report the effective sample size for parameters of one channel (channel 14, not-activated):

```
> effectiveSize(output)
lambda      mu0      mu1      phi      sigma      theta
3919.104  4032.037  4676.081  3173.212  2801.692  5143.000
```

The effective sample size gives an estimate of the equivalent number of independent iterations that the chain represents. If the chain was composed by an independent sample, its effective sample size would be the size of the sample (in our model, the size of the sample is equal to  $5143 = \frac{\text{num.it} - \text{burn-in}}{\text{thinning}}$ ). Lower

the effective sample size is, higher the efficiency lost because of correlation. Our chains show high effective sample sizes, confirming a good thinning.

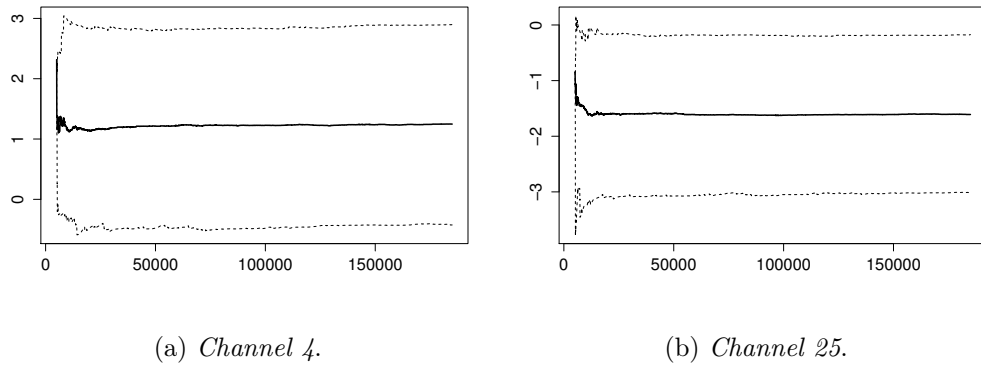


Figure 5.8: Evolution in time of the sample quantiles of  $\mu_1$  for two channels.

Methods here proposed were applied to all parameters of each channel, always obtaining good results. Since we can't report all results for all channels, we chose some of values from the four central channels of both hemispheres.

Convergence analysis were made trough R package coda (for more details on these algorithms see Plummer et al., 2006).

## 5.4 A look to the posterior densities

With the bayesian approach we don't obtain only a numeric estimate of  $\mu_1$ , but we get an estimation of its whole distribution: the posterior density. This distribution is originated by an update of our a priori beliefs (represented by the prior distribution) trough data.

We analyse the posterior densities for  $\mu_1$  in the central channels of the two hemispheres, in order to understand if it is possible to separate activated channels trough them.

Since the hierarchical model inspects the relation between the  $O_2Hb$  concentration and *rest*, we would expect to find a negative dependence between data and the regressor in activated channels, and no correlation between them in the not-activated ones.

This results in an expected value of  $\beta_1$  – that is represented by  $\mu_1$  – lower than 0 in activated channels, near to 0 in the not-activated ones. In this way we would have a demonstration of the dependence of activated signals from the HRF, that is a proof of the cerebral activation.

The posterior distributions for  $\mu_1$  in the two hemispheres are reported in Fig. 5.9 and 5.10. Red lines indicate the 0.05, 0.5 and 0.95 quantiles.

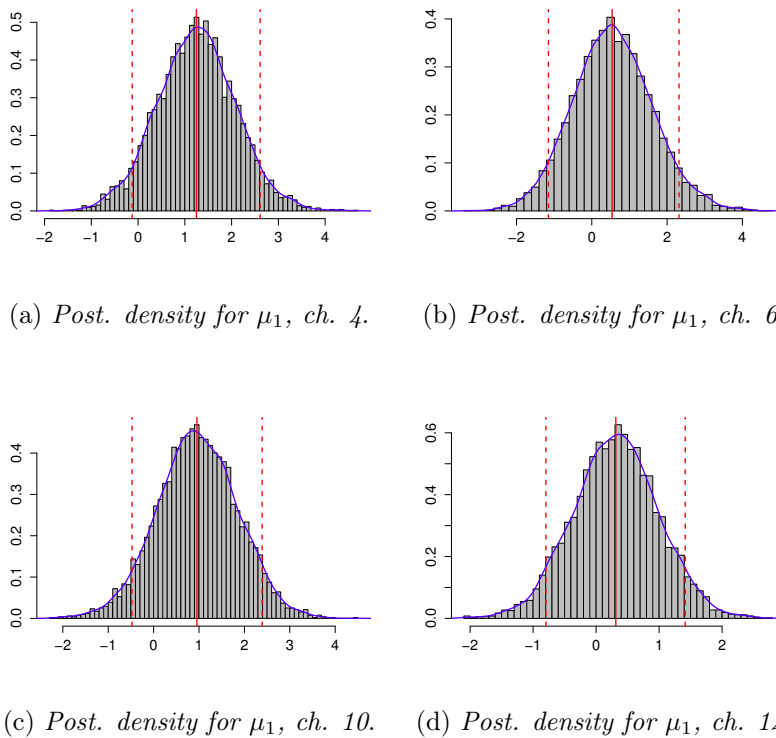
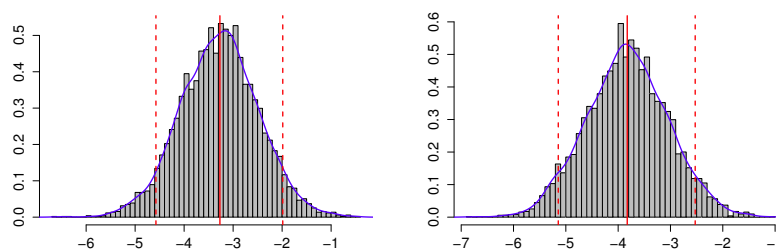


Figure 5.9: Posterior densities for  $\mu_1$  in not-activated channels. Red lines indicate the 0.05, 0.5 and 0.95 quantiles.

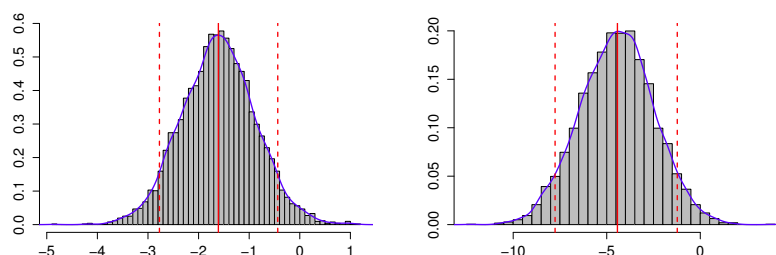
Looking at these figures we can notice that posterior distributions for activated channels are quite different from the ones for not-activated channels. In fact the variance of the distributions and their bell-shapes seem very similar on to the other, but their means are very different: if we focus on the HPD intervals (the dotted red lines) we immediately see that the ones related to the left hemisphere don't include the zero, while the others do.

Our hypothesis on the dependence between  $O_2Hb$  measures and the

regressor *rest* is confirmed: the correlation is negative in activated channels, and near to 0 in not-activated ones. This confirms the proposed frequentist model, in which the hypothesis tests evaluate the equality to 0 of the mean of the coefficients<sup>4</sup>, without having a distribution.



(a) Posterior density for  $\mu_1$ , ch. 17. (b) Posterior density for  $\mu_1$ , ch. 21.



(c) Posterior density for  $\mu_1$ , ch. 25. (d) Posterior density for  $\mu_1$ , ch. 29.

Figure 5.10: Posterior densities for  $\mu_1$  in activated channels. Red lines indicate the 0.05, 0.5 and 0.95 quantiles.

Trough this model, a simple criterion for channels' clusterization (with the binary label activated/not-activated) can be deduced by the visual inspection of the posterior density: if the HPD interval includes the zero the channel is activated, otherwise it isn't.

The goal is reached: channels can be classified trough the proposed hierarchical model.

<sup>4</sup>In Chapter 4 the alternative hypothesis inspects a positive correlation because the observed quantity is a contrast between coefficients.

# Chapter 6

## Conclusions

The present work describes and faces the problem of fNIRS data analysis. In particular, our main objective consists in proposing a new procedure for statistical analysis of activated channels in fNIRS data, exploiting the convenient aspects of some models in the current literature and reducing their weaknesses.

In order to detect noisy channels we performed an outlier detection using the Area Under the Curve (AUC).

We tried to detect noisy channels using the mean and the variance of AUCs on sub-intervals. The proposed procedure showed a good ability in highlighting anomalous channels and a coherence with results deriving from the visual inspection made by experts.

Future analysis could enhance the accuracy of the selection, finding a threshold value (for the mean or for a linear combination between mean and variance). In this way it would be possible to perform an automatic and real-time outlier detection.

The most critical matter about fNIRS data is its strong temporal dependence structure. The vector of data is the concentration of the hemoglobin in a fixed point, during time: surely each measure depends on the previous one.

This dependence, that complicates analysis, contains the information that has to be investigated in order to find activation. In fact activated channels can be recognised by the shape of the hemoglobin signal during time,

by its specific evolution, caused by the neural activation. Thus the strong dependence of measures, that can be a critical point to treat, is at the same time a source of knowledge.

The current literature suggests many procedures for activation detection. One of the most commonly accepted and used method is the General Linear Model (GLM), a linear regression model that uses, as regressors, functions imitating the evolution of the ideal hemodynamic response (e.g. convolutions between scales function and the hemodynamic response function). The GLM is based on hypothesis that were not verified on our datasets.

We introduced a method that minimizes the hypotheses to be fulfilled.

Data have been split in sub-intervals, each one representing a realization of the same event (the elementary activation sequence), and a linear regression model was applied on each of them. Thus, rather than a unique linear combination for each channel, that can be difficult to analyse without making some hypothesis, we obtained a normal population of linear combinations for each channel, which can be easily investigated through an inference test.

The unique hypothesis required to use this model is the gaussianity of the activation-related quantities, and this hypothesis was always confirmed by statistical tests.

The output of this method is a head map where the colour of each channel depends on its activation degree.

This procedure has been applied on in vivo and simulated data, and it has shown very good results in both situations.

In this work we suggest also some ideas to perform a group analysis coherent with the proposed linear regression model. In particular we show a method that mixes signals from different subjects (for each fixed channel), considering them as if they belong to a unique person, and a method that uses the median of P-values that were calculated during the single subject analysis.

Results are good in both situation, even if the latter method was highly influenced by subjects without activated channels.

Further studies should be conducted in this area, analysing the advantages

and drawbacks of both methods in deep.

A k-means clustering algorithm is also proposed as an useful additional tool for activated channels detection.

This clustering algorithm doesn't require any statistical hypothesis: it divides channels in k groups. The number of groups has been chosen maximizing suitable indexes.

Because of the different proceedings compared to the previous algorithm, k-means can be used as a reinforcing control instrument after the proposed method execution.

K-means algorithm performs a correct clusterization on a (simulated or in vivo) subject if its activation map has shown activated channels. Since the classification is not continuous but binary, low activated channels can be misclassified.

If a subject has no activation the algorithm is forced to separate channels in two groups, thus results were unpredictable. For this reason, k-means algorithm should be used after the proposed linear regression model, and its use should be evaluated in each situation.

Some problems can also arise if one (or more) channels are particularly noisy: in this situation the clustering algorithm can separate noisy channels from the others.

Therefore highly noisy channels should be excluded before an analysis with k-means clustering algorithm.

Finally, a bayesian approach has been introduced.

We proposed a hierarchical linear regression model that recalls the frequentist linear model previously analysed: data have been divided in sub-intervals and for each of them a linear model has been set.

For each fixed channel, the analysis focuses on  $\mu_1$ , the random variable that represents the mean of the *task*-related coefficient. An MCMC simulation was run for each channel and the posterior density for the variable of interest  $\mu_1$  was obtained.

We tested the convergence of the simulated Markov Chains trough several instruments and results are very good.

Moreover, we find that it is possible to perform a precise classification (activated/not-activated channels) using the proposed bayesian model, trough an inspection of the posterior densities of  $\mu_1$ . In fact activated channels can be recognised looking at the highest posterior density interval for  $\mu_1$ : if it doesn't include the zero, the channels is activated.

Further studies in this area could apply the bayesian model to simulated or noisier subjects, in order to confirm the validity of the model in critical situations.



# Appendix: R codes

We report the most important R codes used for fNIRS analysis.

In particular, we write the codes for the pre-processing algorithm, the creation of the linear models, the gaussianity tests on coefficients, the tests on contrasts with maps' drawings, and a hint on AUC analysis.

The used packages are specified in the code.

In the following lines:

- `y` is a matrix of size  $490 \times 30$ , with O<sub>2</sub>Hb or HHb measures from an in vivo or synthetic subject. Each column includes hemoglobin concentration in one channel during time.
- `rest` is a vector of length 40, containing the regressor *rest*
- `task` is a vector of length 40, containing the regressor *task*
- `coord` is a matrix of size  $30 \times 2$ , containing channels' coordinates in the page space (it is used for the creation of activation maps).

```
### Baseline mean subtraction and smoothing spline algorithm
period <- 39
start <- seq(51, 411, 40)
start2 <- seq(1, 400, 40)
t <- seq(1, 400)
withoutBase <- matrix(0, 400, 30) # matrix that will contain data
after the baseline subtraction
spl <- matrix(0, 400, 30) # matrix that will contain data after smoothing
spline algorithm
```

```
for(j in 1:30){ # switching each channel
  for(i in 1:10){ # switching each trials
    withoutBase[start2[i):(start2[i]+period),j] <-
    y[start[i):(start[i]+period),j] - mean(y[start[i):(start[i]+9),j])
  }
  spl[, j]<-smooth.spline(t, withoutBase[, j], spar=.001)$y
}

### Linear regression models on sub-intervals
yHat <- matrix(0, 400, 30) # matrix that will contain the fitted
values
betaHat <- matrix(0, 30, 30) # matrix that will contain the coefficients
estimates
period <- 39
start2 <- seq(1, 400, 40)
dist <- seq(1, 30, 3) # [1 4 7 10 13 16 19 22 25 28]
for(i in seq(1, 30)){ # switching each channel
  for(j in 1:10){ # switching each trial
    model <- lm(spl[start2[j] : (start2[j]+period), i]~ rest + task)
    betaHat[i, dist[j] : (dist[j]+2)] <- coefficients(model)
    yHat[start2[j] : (start2[j]+period), i] <- fitted(model)
  }
} # N.B. betaHat: each row is a channel
diff <- betaHat[, dist+2] - betaHat[, dist+1]

### Shapiro tests on coefficients estimates
shapBeta0 <- rep(0,30); shapBeta1 <- rep(0,30) # initialized to 0
shapBeta2 <- rep(0,30); shapContrasts <- rep(0,30)
for(i in 1:30){ # four Shapiro tests on each channel
  shapBeta0[i] <- shapiro.test(betaHat[i, dist])$p.value
  shapBeta1[i] <- shapiro.test(betaHat[i, dist+1])$p.value
  shapBeta2[i] <- shapiro.test(betaHat[i,dist+2])$p.value
  shapContrasts[i] <- shapiro.test(diff[i,])$p.value
}
```

```
### Hypothesis Test: for each channel, a one-sided test
###  $E[\beta_2 - \beta_1] = 0$  vs  $E[\beta_2 - \beta_1] > 0$ 
pva <- rep(0, 30) # vector that will contain P-values
for(i in 1:30){ # one test for each channel
  pva[i] <- t.test(diff[i, ], alternative = 'greater', conf.level
= 0.95)$p.value
}

### Drawing the activation maps
ind <- pva*100
colori <- c('yellow1', 'darkorange', 'darkorange1', 'darkorange2',
  'orangered', 'orangered1', 'orangered2', 'red', 'red1', 'red2',
  'red3', 'darkred', 'red4')
scala <- colorRampPalette(c('white', colori, 'black'), bias = 1,
  space = "rgb")
v <- scala(100)
par(mfrow = c(1,1), mar = c(4, 4.5, 4, 2) + 0.1)
plot(coord[,1], coord[,2], yaxt = 'n', xaxt = 'n', col = c(v[ind+1]),
  xlab = "", ylab = "", pch = CIRCLE<-16, cex = 4, xlim = c(1.5,59),
  ylim = c(1.1, 17.6), pty = 's', bty = 'n')
points(coord[, 1], coord[, 2], pch = 1, cex = 4)
textColor <- (pva < 0.5)
text(coord[, 1], coord[, 2], labels = seq(1, 30), col = textColor)
text(coord[, 1] + 4, coord[, 2], round(pva, 3), cex = 0.5)
lines( c(24, 26.5), c(17.4, 18.25)) # drawing the nose
lines( c(26.5, 29), c(18.25, 17.4), lwd=1)# drawing the nose
require(plotrix) # loading the package plotrix
require(car) # loading the package car
legend(26, 4, c(expression(paste("accepting ",paste(H[0]),sep="")),
  expression(paste("rejecting ",paste(H[0]),sep="))), xjust=1, bty='n',
  cex = 0.8, text.width = 4, y.intersp = 1.3, box.col = 0, pt.lwd = 1,
  pch = c(22,22), col = c(1,1), pt.bg = c(1, 0), pt.cex = 1.5)
ellipse(center = c(26, 8.2), shape = cbind(c(38, 0), c(0, 3.4)),
```

```
radius = 5, col = 1, center.pch = 0, lwd = 0.5)
library(fields) # loading the package fields
palette(v) # drawing the color scale
image.plot(legend.only = T, col = v, horizontal = F, add = T,
  zlim = c(0, 1), reset.graphics = T,
  smallplot = c(0.05, 0.09, 0.2, 0.85))
palette("default")

### AUC
require(pracma) # loading the package pracma
auc <- matrix(0, 10, 30) # matrix 10 × 30 that will contain the
AUCs. Each column is a channel.
sottoins <- matrix(0, 40, 1) # auxiliary variable
start2 <- seq(1, 400, 40)
for(j in 1:30){ # switching channels
  for(i in 1:10){ # switching trials
    sottoins <- spl[start2[i] : (start2[i] + periodo), j]
    auc[i, j] <- trapz(abs(sottoins))
  }
}
med <- colMeans(auc) # a vector with AUC means
varianze <-diag(var(auc)) # a vector with AUC variances
# A simple plot for visual inspection:
plot(med, varianze, pch = 16, ylim = c(min(varianze), 3))
text(med, (varianze)+0.1, seq(1,30))
```

# Ringraziamenti

Desidero ringraziare Lucia Zucchelli, Rebecca Re, Lorenzo Spinelli, Davide Contini e Alessandro Torricelli del Dipartimento di Fisica del Politecnico, che con me hanno condiviso l'appassionante percorso che ha portato a questo lavoro. La loro professionalità e collaborazione sono state determinanti per la realizzazione di un progetto che richiedeva il contributo e l'integrazione di competenze fisiche e statistiche. Ringrazio in particolare Lucia per la disponibilità e l'aiuto offerto.

Un profondo ringraziamento alla Prof.ssa Anna Maria Paganoni e alla Dott.ssa Francesca Ieva, per avermi seguita e sostenuta in questo stimolante progetto con grande disponibilità e competenza. Le ringrazio per avermi insegnato tanta statistica, e per averlo fatto con passione ed entusiasmo contagiosi. È bello trovare persone così preparate e appassionate alla scienza e al proprio lavoro, sempre presenti, costruttive e piene di energia e stimoli. Incontrarle è stato un dono prezioso, e io le ringrazierò all'infinito (per fortuna, tra statistici ci si intende, basteranno una trentina di grazie).



# Bibliography

- Barker J. W., Aarabi A., Huppert T. J. (2013) Autoregressive model based algorithm for correcting motion and serially correlated errors in fNIRS. *Biomedical Optics Express*, vol. 4: 1366–1379.
- Benaron D. A., Hintz S. R., Villringer A., Boas D., Kleinschmidt A., Frahm J., Hirth C., Obrig H., Van Houten J. C., Kermit E. L., Cheong W.-F., Stevenson D. K. (2000) Noninvasive functional imaging of human brain using light. *Journal of Cerebral Blood Flow and Metabolism*, vol. 20, 3: 469–477.
- Boas D. A., Dale A. M., Franceschini M. A. (2004) Diffuse optical imaging of brain activation: approaches to optimizing image sensitivity, resolution, and accuracy. *NeuroImage*, vol. 23 Suppl 1: S275–S288.
- Bonomini V., Zucchelli L., Re R., Ieva F., Spinelli L., Contini D., Paganoni A. M., Torricelli A. Linear regression models and K-means clustering for statistical analysis of fNIRS data. *Submitted*.
- Contini D., Spinelli L., Caffini M., Cubeddu R., Torricelli A. (2009) A multichannel time-domain brain oximeter for clinical studies. Proceedings of SPIE-OSA European Conference on Biomedical Optics.
- Contini D., Torricelli A., Pifferi A., Spinelli L., Paglia F., Cubeddu R. (2006) Multi-channel time-resolved system for functional near infrared spectroscopy. *Optics express*, vol. 14, 12: 5418–5432.
- Cooper R. J., Selb J., Gagnon L., Phillip D., Schyetz H. W., Iversen H. K., Ashina M., Boas D. A. (2012) A systematic comparison of motion artifact

- correction techniques for functional near-infrared spectroscopy. *Frontiers in neuroscience*, vol. 6, 147: 1–10.
- Cui X., Bray S., Reiss A. L. (2010) Functional Near Infrared Spectroscopy (NIRS) signal improvement based on negative correlation between oxygenated and deoxygenated hemoglobin dynamics. *NeuroImage*, vol. 49, 4.
- Erdoğan S. B., Yücel M. A., Akin A. (2014) Analysis of task-evoked systemic interference in fNIRS measurements: insights from fMRI. *NeuroImage*, vol. 87: 490–504.
- Fekete T., Rubin D., Carlson J. M., Mujica-Parodi L. R. (2011) The NIRS Analysis Package: noise reduction and statistical inference. *PLoS One*, 24322.
- Franceschini M. A., Boas D. A. (2004) Noninvasive measurement of neuronal activity with near-infrared optical imaging. *NeuroImage*, vol. 21, 1: 372–386.
- Franceschini M. A., Joseph D. K., Huppert T. J., Diamond S. G. (2006) Diffuse optical imaging of the whole head. *Journal of Biomedical Optics*, vol. 11, 5: 1–22.
- Friston K. J., Ashburner J. T., Kiebel S. J., Nichols T. E., Penny W. D. (2011) *Statistical Parametric Mapping: The Analysis of Functional Brain Images*, Academic Press.
- Friston K. J., Holmes A. P., Worsley K. J., Poline J.-B., Frith C. D., Frackowiak R. S. J. (1994) Statistical Parametric Maps in Functional Imaging: A General Linear Approach. *Human Brain Mapping*, vol. 2, 4: 189–210.
- Gagnon L., Cooper R. J., Yücel M. A. (2012) Short separation channel location impacts the performance of short channel regression in NIRS. *NeuroImage*, vol. 59, 3: 2518–2528.
- Gagnon L., Perdue K., Greve D. N., Goldenholz D., Boas D. A. (2011) Improved recovery of the hemodynamic response in diffuse optical imaging using short optode separations and state-space modeling. *NeuroImage*, vol. 56, 3: 1362–1371.



- Genest M., Masse J.-C., Plante, J.-F. (2012) `depth`: Depth functions tools for multivariate analysis. R package version 2.0-0.
- Germon T. J., Evans P. D., Barnett N. J., Wall P., Manara A. R., Nelson R. J. (1999) Cerebral near infrared spectroscopy: emitter-detector separation must be increased. *British Journal of Anaesthesia*, vol. 82, 6: 831–837.
- Germon T. J., Evans P. E., Barnett N. J., Lewis T. T., Wall P., Nelson Richard J. (1997) Changes in tissue oxyhaemoglobin concentration measured using multichannel near infrared spectroscopy during internal carotid angiography. *Journal of neurology, neurosurgery, and psychiatry*, vol. 63: 660–664.
- Harville D. A. (1977) Maximum likelihood approaches to variance component estimation and to related problems. *Journal of the American Statistical Association*, vol. 72, 358: 320–338.
- Hoff P. (2009) *A First Course in Bayesian Statistical Methods*. Springer.
- Huppert T. J., Hoge R. D., Diamond S. G., Franceschini M. A., Boas D. A. (2006) A temporal comparison of BOLD, ASL, and NIRS hemodynamic responses to motor stimuli in adult humans. *NeuroImage*, vol. 29, 2: 368–382.
- Izzetoglu M., Devaraj A., Bunce S., Onaral B. (2005) Motion artifact cancellation in NIR spectroscopy using Wiener filtering. *IEEE Transactions on Biomedical Engineering*, vol. 52, 5: 934–938.
- Izzetoglu M., Chitrapu P., Bunce S., Onaral B. (2010) Motion artifact cancellation in NIR spectroscopy using discrete Kalman filtering. *Biomedical Engineering Online*, vol. 9, 1: 16.
- Kim M. N., Durduran T., Frangos S., Edlow B. L. (2010) Noninvasive Measurement of Cerebral Blood Flow and Blood Oxygenation Using Near-Infrared and Diffuse Correlation Spectroscopies in Critically Brain-Injured Adults. *Neurocritical Care*, vol. 12: 173–180.

- Koh P. H., Glaser D. E., Flandin G., Butterworth B., Maki A., Delpy D., Elwell C. E. (2007) Functional Optical Signal Analysis (fOSA): A Software Tool for NIRS Data Processing Incorporating Statistical Parametric Mapping (SPM). *Journal of Biomedical Optics*, vol. 12, 6: 064010.
- Lina J.-M., Matteau-Pelletier C., Dehaes M., Desjardins M., Lesage F. (2010) *Wavelet-based estimation of the hemodynamic responses in diffuse optical imaging*. *Medical Image Analysis*, vol. 14, 4: 606–616.
- Maechler M., Rousseeuw P., Struyf A., Hubert M., Hornik K. (2013) `cluster`: Cluster Analysis Basics and Extensions.
- Murata Y., Sakatani K., Katayama Y., Fukaya C. (2002) Increase in focal concentration of deoxyhaemoglobin during neuronal activity in cerebral ischaemic patients. *Journal of Neurology, Neurosurgery and Psychiatry*, vol. 73, 2: 182–184.
- Plummer M., Best N., Cowles K., Vines K. (2006) CODA: Convergence Diagnosis and Output Analysis for MCMC. *R News*, vol. 6, 1: 7–11.
- Plummer M. (2003) JAGS: A Program for Analysis of Bayesian Graphical Models Using Gibbs Sampling Proceedings of Distributed Statistical Computing.
- Robertson F. C., Douglas T. S., Meintjes E. M. (2010) Motion Artifact Removal for Functional Near Infrared Spectroscopy: a Comparison of Methods. *IEEE Transactions on Biomedical Engineering*, vol. 57, 6: 1377–1387.
- Saager R. B., Berger A. J. (2005) Direct characterization and removal of interfering absorption trends in two-layer turbid media. *Journal of the Optical Society of America. A: Optics, Image Science, and Vision*, vol. 22, 9: 1874–1882.
- Sato H., Tanaka N., Uchida M., Hirabayashi Y., Kanai M., Ashida T., Konishi I., Maki A. (2006) Wavelet analysis for detecting body-movement artifacts in optical topography signals. *NeuroImage*, vol. 33, 2: 580–587.

- Scarpa F., Brigadoi S., Cutini S., Scatturin P., Zorzi M., Dell'Acqua R., Sparacino G. (2013) A reference-channel based methodology to improve estimation of event-related hemodynamic response from fNIRS measurements. *NeuroImage*, vol. 72: 106–119.
- Scholkmann F., Spichtig S., Muehlemann T., Wolf M. (2010) How to detect and reduce movement artifacts in near-infrared imaging using moving standard deviation and spline interpolation. *Physiological Measurement*, 31: 649–662.
- Scholkmann F., Wolf M. (2012) Measuring brain activity using functional near infrared spectroscopy: a short review. *Spectroscopy Europe*, vol 24, 4.
- Shumway R. H., Stoffer D. S. (2010) Time Series Analysis and its applications, Springer.
- Struyf A., Hubert M., Rousseeuw P. (1997) Clustering in an Objected-Oriented Environment. *Journal of Statistical Software*, vol. 1, 4.
- Tak S., Jang K. E., Jung J., Jang J., Ye J. C. (2008) General linear model and inference for near infrared spectroscopy using global confidence region analysis. *Biomedical Imaging: From Nano to Macro*, pag. 476–479.
- Tak S., Ye J. C. (2014) Statistical analysis of fNIRS data: a comprehensive review. *NeuroImage*.
- Tak S., Yoon S. J., Jang J., Yoo K., Jeong Y., Ye J. C. (2011) Quantitative analysis of hemodynamic and metabolic changes in subcortical vascular dementia using simultaneous near-infrared spectroscopy and fMRI measurements. *NeuroImage*, vol. 55, 1: 176–184.
- Takemura A., Kuriki S. (2002) On the equivalence of the tube and Euler characteristic methods for the distribution of the maximum of Gaussian fields over piecewise smooth domains. *Annals of Applied Probability*, vol. 12, 2: 768–796.
- Tanosaki M., Sato C., Shimada M., Iguchi Y., Hoshi Y. (2003) Effect of stimulus frequency on human cerebral hemodynamic responses to electric

- median nerve stimulation: a near-infrared spectroscopic study. *Neuroscience Letters*, vol. 352: 1–4.
- Umeyama S., Yamada T. (2014) Monte Carlo study of global interference cancellation by multidistance measurement of near-infrared spectroscopy. *Journal of Biomedical Optics*, vol. 14, 6.
- White B. R., Snyder A. Z., Cohen A. L., Petersen S. E. (2009) Resting-state functional connectivity in the human brain revealed with diffuse optical tomography. *NeuroImage*, vol. 47, 1: 148–156.
- White H. (1980) A Heteroskedasticity-Consistent Covariance Matrix Estimator and a Direct Test for Heteroskedasticity. *Econometrica*, vol. 48, 4: 817–838.
- Worsley K. J., Friston K. J. (1995) Analysis of fMRI Time-Series Revisited—again. *NeuroImage*, pag. 173–181.
- Ye J. C., Moulin P., Bresler Y. (2006) Asymptotic global confidence regions for 3-D parametric shape estimation in inverse problems. *IEEE Transactions on Image Processing*, vol. 15, 10: 2904–2919.
- Ye J. C., Tak S., Jang K. E., Jung J., Jang J. (2009) NIRS-SPM: statistical parametric mapping for near-infrared spectroscopy. *NeuroImage*, vol. 44, 2: 428–447.
- Zeff B. W., White B. R., Dehghani H., Schlaggar B. L., Culver J. P. (2007) Retinotopic mapping of adult human visual cortex with high-density diffuse optical tomography. *Proceedings of the National Academy of Sciences of the United States of America*, vol. 104, 29: 12169–12174.
- Zhang Q., Brown E. N., Strangman G. E. (2007) Adaptive filtering for global interference cancellation and real-time recovery of evoked brain activity: a Monte Carlo simulation study. *Journal of Biomedical Optics*, vol. 12, 4.
- Zucchelli L., Contini D., Re R., Torricelli A., Spinelli L. (2013) Method for the discrimination of superficial and deep absorption variations by time domain fNIRS. *Biomedical Optics Express*, vol. 4, 12: 2893–2910.

Zucchelli L. (2013) Development and applications of a medical device based on time domain functional Near Infrared Spectroscopy for brain imaging. Ph.D. Thesis, Politecnico of Milan.